POLITECNICO
MILANO 1863

SCUOLA DI INGEGNERIA INDUSTRIALE
E DELL'INFORMAZIONE

Directly encoding morphological features of microstructure anatomy into the diffusion MRI signal

Tesi di Laurea Magistrale in
Ingegneria Biomedica

MSc Thesis in
Biomedical Engineering

Author: **Vittoria Cappozzo**

Polimi Student ID:	222920
DTU Student ID:	s233228
Polimi advisor:	Prof. Enrico Gianluca Caiani
DTU advisors:	Prof. Tim Bjorn Dyrby
	Assoc. Prof. Marco Pizzolato, Emma Thomson, PhD
Academic Year:	2024-25

Abstract

Diffusion Magnetic Resonance Imaging (dMRI) is a non-invasive modality that probes the microstructural properties of biological tissues, providing valuable insights into cellular architecture and tissue integrity. This thesis investigates the application of advanced diffusion encoding schemes for the detection of early microstructural changes associated with Alzheimer's Disease (AD), with a particular focus on axonal pathology.

An ex vivo protocol was implemented, combining Triple Diffusion Encoding (TDE) and Single Diffusion Encoding (SDE) at high b-values, and results were compared with those obtained using Diffusion Tensor Imaging (DTI) fitted on Pulsed Gradient Spin Echo (PGSE) data.

The TDE–SDE approach enables estimation of intra-axonal diffusivity, axonal signal fraction, and microscopic anisotropy with fewer modeling assumptions. It uses high b-values to suppress extracellular signals and applies the spherical mean technique to eliminate confounding effects from orientation dispersion and multiple fiber orientations—common sources of error in DTI metrics.

Experiments were conducted on TgF344-AD rats, a transgenic model of the disease, at two progression stages (4 and 17 months). The extracted microstructural parameters were statistically analyzed to assess their sensitivity to pathological changes. Results show that the TDE–SDE protocol outperforms DTI in detecting intra-axonal alterations, revealing significant differences in axonal diffusivity as early as 4 months. These findings support the use of advanced diffusion encoding techniques as non-invasive, sensitive, and potentially specific biomarkers for the early diagnosis of Alzheimer's disease in preclinical models.

Keywords: Diffusion Magnetic Resonance Imaging (dMRI), Triple Diffusion Encoding (TDE), Single Diffusion Encoding (SDE), Pulsed Gradient Spin Echo (PGSE), Diffusion Tensor Imaging (DTI), Diffusivity, Microscopic Anisotropy, Spherical Mean, Alzheimer's Disease, TgF344-AD.

Abstract in lingua italiana

La Risonanza Magnetica di Diffusione (dMRI) è una tecnica non invasiva che esplora le proprietà microstrutturali dei tessuti biologici, fornendo informazioni sull'architettura cellulare e sull'integrità tissutale. Questa tesi analizza l'impiego di schemi avanzati di codifica della diffusione per l'individuazione precoce di alterazioni microstrutturali associate alla Malattia di Alzheimer (AD), con particolare attenzione alla patologia assonale. È stato utilizzato un protocollo ex vivo combinando Codifica Tripla di Diffusione (TDE) e Codifica Singola di Diffusione (SDE) a elevati valori di b, confrontando i risultati con quelli ottenuti tramite Diffusion Tensor Imaging (DTI) basato su sequenze Pulsed Gradient Spin Echo (PGSE).

L'approccio TDE–SDE consente di stimare la diffusività intra-assonale, la frazione di segnale assonale e l'anisotropia microscopica con un numero ridotto di assunzioni modellistiche. Utilizza alti valori di b per sopprimere il segnale extracellulare e applica la tecnica della media sferica per eliminare gli effetti confondenti dovuti alla dispersione dell'orientamento e alla presenza di più orientazioni delle fibre, che spesso compromettono l'accuratezza delle metriche della DTI.

Gli esperimenti sono stati condotti su ratti TgF344-AD, un modello transgenico della malattia, in due fasi di progressione (4 e 17 mesi). I parametri microstrutturali estratti sono stati analizzati statisticamente per valutarne la sensibilità ai cambiamenti patologici. I risultati mostrano che il protocollo TDE–SDE supera il DTI nel rilevare alterazioni intra-assonali, evidenziando differenze significative nella diffusività assonale già a 4 mesi. Questi dati supportano l'uso di tecniche avanzate di codifica della diffusione come biomarcatori non invasivi, sensibili e potenzialmente specifici per la diagnosi precoce dell'Alzheimer in modelli preclinici.

Parole chiave: Risonanza Magnetica di Diffusione (dMRI), Codifica Tripla di Diffusione (TDE), Codifica Singola di Diffusione (SDE), Pulsed Gradient Spin Echo (PGSE), Diffusion Tensor Imaging (DTI), Diffusività, Anisotropia Microscopica, Media Sferica, Malattia di Alzheimer, TgF344-AD.

Contents

1 | Introduction

Diffusion Magnetic Resonance Imaging (dMRI) is a non-invasive imaging technique that exploits the thermal motion of water molecules (Brownian motion) —specifically, water self-diffusion—to generate contrast and map microstructural features within biological tissues. By sensitizing the MRI signal to the random motion of water, dMRI enables the probing of cellular architecture, offering unique insights into tissue organization and integrity. As water molecules diffuse throughout the tissue, they interact with the local environment, encountering hindrances and restrictions imposed by cellular and subcellular structures. Through this interaction, features of the underlying microstructure are effectively encoded into the displacement patterns of the diffusing molecules. Given an appropriately designed diffusion-weighted experiment, these microstructural characteristics can be inferred from the observed signal. For instance, the apparent diffusivity decreases in regions of high tissue density and becomes directionally dependent (anisotropic) in the presence of aligned structures, such as axon fibers. Through this mechanism, dMRI enables a non-invasive, indirect assessment of tissue microstructure [47, 72].

This sensitivity to microscopic tissue properties has made dMRI an invaluable tool in neuroscience, neuroanatomy, and clinical neurology. It also finds broader applications beyond the brain, including musculoskeletal, whole-body, and organ-specific imaging under both normal and pathological conditions. One of its key applications, fiber tractography, uses diffusion information to reconstruct the orientation and connectivity of white matter tracts in the brain, aiding in the study of structural brain networks [47].

While in vivo dMRI enables real-time, non-invasive tissue characterization, ex vivo imaging offers several experimental advantages, including longer scanning times and the absence of motion. Moreover, preclinical scanners used for ex vivo studies can reach higher magnetic field strengths due to their smaller bore diameter, along with stronger and faster switching gradients. The small bore size also allows the radiofrequency (RF) coil to be positioned very close to the sample, significantly increasing the signal-to-noise ratio (SNR). These characteristics enable the implementation of advanced diffusion encoding schemes such as higher b-values and shorter diffusion times—which are often unfeasible in vivo.
On the other hand, ex vivo imaging has to account for tissue fixation, which might slightly alter the tissue microstructure and hence bias the analysis. Among the consequences of tissue fixation, it was shown that intra-/extracellular space volume fraction shifts, cell membrane permeability, relaxation rates, and diffusion coefficients change. It is important to consider these effects when designing the scanning protocol [64].

In biomedical research, animal models serve as a crucial tool for investigating the sensitivity of dMRI to tissue alterations associated with pathological conditions and therapeutic interventions, all within a controlled experimental environment. Importantly, many animal species share susceptibility to diseases observed in humans, while also offering the advantage of being studied across their entire lifespan and even across generations.
Ex vivo animal imaging is particularly valuable for linking in vivo MRI findings with histological validation, and for testing innovative diffusion sequences that may yield new imaging biomarkers [30, 64].

In this thesis, an ex vivo animal model was used to detect possible biomarkers of Alzheimer's disease (AD) in rat brains. The parameters of interest included diffusivities, axonal signal fraction, and microscopic fractional anisotropy. To achieve this, various models and acquisition sequences were utilized, with model selection guided by the goal of minimizing assumptions and enhancing the generalizability of the results. The diffusion encoding schemes ranged from simple linear methods, such as the conventional pulsed gradient spin echo (PGSE), to more complex setups, such as tensor encoding implemented with a triple diffusion encoding (TDE) scheme. Eventually, parameter estimation was performed using non-linear least squares (NLLS) fitting, and the new acquisition protocol was tested statistically.

The findings demonstrate that tensor-valued diffusion encoding improves sensitivity to microstructural features compared to traditional diffusion tensor imaging (DTI) modeling applied to pulsed gradient spin echo (PGSE) data. This improvement enables more accurate characterization of both white matter (WM) and gray matter (GM) integrity. Disease-related alterations in axonal diffusivity were identified in the Alzheimer's rat brain, supporting the potential of advanced diffusion encoding as a non-invasive imaging biomarker in preclinical neurodegeneration research.

2 | Motivation: Alzheimer's Disease

Alzheimer's disease is a progressive neurodegenerative disease and the leading cause of dementia worldwide. It is rapidly emerging as one of the most costly, fatal, and impactful health challenges of this century [63]. Currently, around 32 million people have AD dementia, 69 million live with Mild Cognitive Impairment (MCI), and over 315 million are in a preclinical stage of the disease. Together, these groups make up about 22% of the global population aged 50 and above. This number is expected to triple by 2050[50].

AD progresses through three major stages: preclinical phase, involving the silent buildup of amyloid-beta (Aβ) plaques, Mild Cognitive Impairment with early functional changes, and Alzheimer's dementia, marked by significant cognitive decline and brain atrophy. The disease affects multiple brain systems, particularly the medial temporal lobe and associative neocortical structures, resulting in impairments in memory, executive function, attention, and spatial navigation. Pathological features include extracellular amyloid plaques, intracellular tau tangles, neuronal loss, gliosis, and neuroinflammation. Additional findings include cortical thinning, hippocampal shrinkage, enlarged ventricles, reduced glucose metabolism, and oxidative stress [50].

Alzheimer's disease can be classified into two main types. The first is familial early-onset AD (FAD), a rare form that is caused by inherited mutations in specific genes, such as the amyloid precursor protein (APP), presenilin-1 (PSEN1), presenilin-2 (PSEN2), and microtubule associated protein tau (MAPT) genes. These genetic changes can also increase the risk for the later-onset form of the disease. The second and more common type is sporadic late-onset AD (LOAD), which usually develops in older adults and results from a combination of genetic, environmental, and lifestyle factors. Among the genetic risk factors, the strongest is a variant of the apolipoprotein E gene, known as APOE ϵ4, along with variants in the TREM2 gene, which plays a role in the brain's immune response [50].

Current diagnostic methods for Alzheimer's disease, such as PET imaging and cerebrospinal fluid (CSF) analysis of beta-amyloid and tau, are valuable for confirming pathology but are often invasive, expensive, and not ideal for early-stage detection, as they lack sensitivity. However, early diagnosis is essential to maximize the effectiveness of both symptomatic and potentially disease-modifying therapies. This emphasizes the need for non-invasive biomarkers capable of detecting early pathological changes, before clinical symptoms fully manifest. To address this, the TgF344-AD

rat model[11] is employed, which replicates the full pathological spectrum of AD, including age-dependent amyloidosis, tauopathy, gliosis, neuronal loss, and cognitive impairments. The study aims to investigate early axonal and neuronal changes in both gray and white matter of TgF344-AD rats at 4 and 17 months using advanced diffusion MRI techniques. In particular, the study will focus on identifying axonal swellings, an early hallmark of neurodegeneration. Key imaging biomarkers to be examined include axial and radial diffusivity, microscopic anisotropy, and axonal signal fraction. This project complements histological findings from the Ph.D. study conducted by Julie S. Hansen, with the goal of advancing diffusion MRI as a sensitive, non-invasive tool for detecting early AD-related microstructural alterations [25].

3 | Theoretical background

In this chapter, the foundational theory of the project is described.

3.1. A diffusion weighted pulse sequence

In this section, the theory underlying diffusion MRI is presented following the material of the special course "Eksperimentelt design af avancerede diffusion-MRI-kodninger til neuroimaging-applikationer" produced by Ass. Prof. Marco Pizzolato, and the simplest diffusion sequence is introduced.

A diffusion-weighted pulse sequence is obtained by adding a pair of diffusion-sensitizing gradients to a T_2-weighted spin-echo sequence. When the two gradients applied along one direction have the same magnitude, the encoding scheme is called Stejskal-Tanner diffusion encoding [69], and the sequence is known as Pulsed Gradient Spin Echo. To capture the anisotropic diffusion properties of tissues, these gradients are typically applied sequentially along multiple directions within the same scan session, resulting in multiple diffusion-weighted images with different gradient orientations.

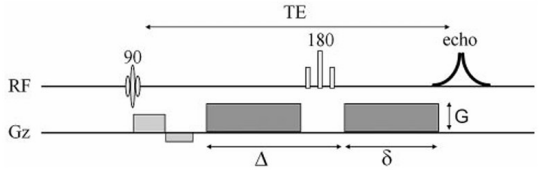

Figure 3.1: Example of PGSE sequence. Diffusion gradients are applied along the z direction. Diffusion sequence parameters are highlighted: δ is the duration of a single pulse, Δ instead refers to the interval between the onset of the two diffusion gradients, and G is the gradient amplitude (referred to as g in the notation used throughout the thesis to denote scalar amplitude). Reproduced by [47].

In general, the effect of the gradients $\mathbf{g}$ is to change the value of the applied magnetic field depending on the position $\mathbf{r}$ of the particles:

$$B(\mathbf{r}) = B_0 + \mathbf{g} \cdot \mathbf{r}. \tag{3.1}$$

This phenomenon is reflected in the phase of the spin:

$$\phi(t) = \gamma \int_0^t \omega_g(\theta)\, d\theta = \gamma \int_0^t (B_0 + \mathbf{g}(\theta) \cdot \mathbf{r}(\theta)\,) d\theta. \tag{3.2}$$

The 180° pulse between the two gradients flips the phase accumulated by the spins during the first diffusion gradient. Since the second diffusion gradient has the same amplitude and direction, any spin that has not moved during that interval experiences an equal and opposite phase shift, resulting in complete rephasing of its signal. However, in the case of diffusion, water molecules move randomly and can experience a different phase accumulation under the second gradient. As a result, these spins are not fully rephased, leading to signal loss.

The diffusion-weighted contrast can be fit into the following model, describing the attenuation signal measured at the echo time (TE) τ:

$$E(\tau) = \frac{S(\tau)}{S_0} = \left\langle e^{i\phi(\tau)} \right\rangle = \left\langle e^{i\gamma \int_0^\tau \mathbf{g}(t)\cdot\mathbf{r}(t)dt} \right\rangle, \tag{3.3}$$

where:

- $S(\tau)$[1]is the signal at echo time τ when diffusion gradients are applied;
- S_0 is the signal obtained from a pure spin echo, without the application of any diffusion gradient;
- $\phi(\tau)$ represents the phase as a function of τ,
- $\mathbf{g}(t)$ and $\mathbf{r}(t)$ are vectors representing respectively gradients and position as a function of time[2];
- $\langle\rangle$ denotes the average over an ensemble of particles, because usually diffusion deals with a large group of particles.

Equation 3.3 holds for any type of diffusion sequence. Let the specifications now be defined for a PGSE sequence. Considering constant gradient amplitude and the durations as shown in Fig. 3.1, the phase becomes:

$$\begin{aligned} \phi &= \gamma \left(\int_{t_0}^{t_0+\delta} \mathbf{g}\cdot\mathbf{r}(t)\,dt - \int_{t_0+\Delta}^{t_0+\Delta+\delta} \mathbf{g}\cdot\mathbf{r}(t)\,dt \right) \\ &= \gamma\mathbf{g} \left(\int_{t_0}^{t_0+\delta} \mathbf{r}(t)\,dt - \int_{t_0+\Delta}^{t_0+\Delta+\delta} \mathbf{r}(t)\,dt \right). \end{aligned} \tag{3.4}$$

Moreover, the integrals in Eq. 3.4 can be expressed as functions of the center of mass of the trajectory of the spins during the first and second pulse [46]:

[1]Throughout this thesis, S denotes the diffusion-weighted signal, E the signal attenuation, i.e., the normalized signal $S(\tau)/S_0$, and $\bar{S}$ and $\bar{E}$ denote the relative spherical mean.

[2]Vectors are represented as bold lowercase letters.

$$\mathbf{r}_1^{cm} = \frac{1}{\delta}\int_{t_0}^{t_0+\delta} \mathbf{r}(t)\,dt \tag{3.5}$$

$$\mathbf{r}_2^{cm} = \frac{1}{\delta}\int_{t_0+\Delta}^{t_0+\Delta+\delta} \mathbf{r}(t)\,dt. \tag{3.6}$$

These two relationships represent the average position of the spins over time. The phase can be then further expressed as

$$\begin{aligned}\phi &= \gamma\delta\mathbf{g}\cdot(\mathbf{r}_1^{cm} - \mathbf{r}_2^{cm}) \\ &= -\gamma\delta\mathbf{g}\cdot\mathbf{r}^{cm} \\ &= -\mathbf{q}\cdot\mathbf{r}^{cm},\end{aligned} \tag{3.7}$$

where $\mathbf{q}$ is called q-vector and represents a spatial frequency, measured in $[1/m]$.

$$\mathbf{q} = \gamma\delta\mathbf{g} \tag{3.8}$$

The q-vector carries important information, because it describes the shape of the gradient, since the product $\delta\mathbf{g}$ represents the area of the gradient. Importantly, the vector $\mathbf{r^{cm}}$ depends on δ and Δ, as evident from Eq, 3.5 and Eq. 3.6.

With this information, Eq. 3.3 can be rewritten for a PGSE sequence as

$$E(\tau) = \frac{S(\tau)}{S_0} = \left\langle e^{i\phi(\tau)}\right\rangle = \left\langle e^{-i\mathbf{q}\cdot\mathbf{r^{cm}}}\right\rangle, \tag{3.9}$$

A simplified expression for the attenuation signal of a PGSE sequence can be derived using the cumulant expansion. Recalling that the cumulant expansion is the power series expansion of the natural logarithm of the characteristic function $\mathbb{E}[e^{itX}]$ of a random variable X , one can rewrite Equation 3.3, treating the position $\mathbf{r}$ as a stochastic process. The general characteristic function can be expanded as

$$H(t) = \log\mathbb{E}[e^{itX}] = \sum_{n=1}^{\infty}\frac{\kappa_n(it)^n}{n!} = i\kappa_1 t - \frac{\kappa_2 t^2}{2} + \cdots \tag{3.10}$$

where κ_n are the cumulants of the stochastic variable X, defined as

$$\kappa_n = \frac{d^n}{dt^n}\log\mathbb{E}\left[e^{tX}\right]\Big|_{t=0} \tag{3.11}$$

After simplifications, the expression of the first cumulants are the following:

$$\kappa_1 = \mathbb{E}[X] = \mu_1 \tag{3.12}$$

$$\kappa_2 = \mathbb{E}\left[(X - \mathbb{E}[X])^2\right] = \mathbb{E}[X^2] - (\mathbb{E}[X])^2 = \mu_2 - \mu_1^2 \tag{3.13}$$

$$\kappa_3 = \mathbb{E}\left[(X - \mathbb{E}[X])^3\right] = \mu_3 - 3\mu_1\mu_2 + 2\mu_1^3 \tag{3.14}$$

$$\kappa_4 = \mathbb{E}\left[(X - \mathbb{E}[X])^4\right] - 3\left(\mathbb{E}\left[(X - \mathbb{E}[X])^2\right]\right)^2 = \mu_4 - 4\mu_3\mu_1 - 3\mu_2^2 + 12\mu_2\mu_1^2 - 6\mu_1^4 \tag{3.15}$$

Analogously, taking the logarithm of the attenuation in Eq. 3.3, its cumulant expansion is:

$$\log E(\tau) = i\gamma\kappa_1 - \frac{\gamma^2}{2}\kappa_2 + \cdots \tag{3.16}$$

where κ_n are the cumulants of the stochastic variable

$$X = \int_0^\tau \mathbf{g}(t) \cdot \mathbf{r}(t) dt. \tag{3.17}$$

Since the spin position is the only random variable, the cumulants can be solved as following:

$$\kappa_1 = \mathbb{E}[X] \tag{3.18}$$

$$= \left\langle \int_0^\tau \mathbf{g}(t) \cdot \mathbf{r}(t) dt \right\rangle \qquad \mathbf{g}(t) \text{ is not random} \tag{3.19}$$

$$= \int_0^\tau \mathbf{g}(t) \cdot \langle \mathbf{r}(t) \rangle dt \qquad \text{linearity of expectation} \tag{3.20}$$

$$\kappa_2 = \left\langle \left(\int_0^\tau \boldsymbol{g}(t) \cdot \boldsymbol{r}(t) dt \right)^2 \right\rangle - \kappa_1^2 \tag{3.21}$$

$$= \left\langle \left(\int_0^\tau \boldsymbol{g}(t) \cdot \boldsymbol{r}(t) dt \right) \left(\int_0^\tau \boldsymbol{g}(t) \cdot \boldsymbol{r}(t) dt \right) \right\rangle - \kappa_1^2 \tag{3.22}$$

$$= \left\langle \int_0^\tau \int_0^\tau [\boldsymbol{g}(t_1) \cdot \boldsymbol{r}(t_1)][\boldsymbol{g}(t_2) \cdot \boldsymbol{r}(t_2)] dt_1 dt_2 \right\rangle - \kappa_1^2 \qquad \text{Fubini's theorem} \tag{3.23}$$

$$= \int_0^\tau \int_0^\tau \langle [\boldsymbol{g}(t_1) \cdot \boldsymbol{r}(t_1)][\boldsymbol{g}(t_2) \cdot \boldsymbol{r}(t_2)] \rangle dt_1 dt_2 - \kappa_1^2 \qquad \text{linearity of expectation} \tag{3.24}$$

Now recalling that $\mathbf{g}(t)$ and $\mathbf{r}(t)$ are tridimensional vectors:

$$\mathbf{g}(t) = [g_x(t), g_y(t), g_z(t)]^T, \quad \mathbf{r}(t) = [r_x(t), r_y(t), r_z(t)]^T$$

Their dot product is:

$$\mathbf{g}(t_1) \cdot \mathbf{r}(t_1) = \sum_{j=x,y,z} g_j(t_1) r_j(t_1) \tag{3.25}$$

$$\mathbf{g}(t_2) \cdot \mathbf{r}(t_2) = \sum_{k=x,y,z} g_k(t_2) r_k(t_2) \tag{3.26}$$

Therefore, the two products in Eq. 3.24 become:

$$\begin{aligned}
&\langle [\mathbf{g}(t_1) \cdot \mathbf{r}(t_1))][\mathbf{g}(t_2) \cdot \mathbf{r}(t_2)] \rangle = \\
&= \left\langle \left[\sum_{j=x,y,z} g_j(t_1) r_j(t_1) \right] \left[\sum_{k=x,y,z} g_k(t_2) r_k(t_2) \right] \right\rangle && (3.27) \\
&= \left\langle \sum_{j=x,y,z} \sum_{k=x,y,z} g_j(t_1) g_k(t_2) r_j(t_1) r_k(t_2) \right\rangle && (3.28) \\
&= \sum_{j=x,y,z} \sum_{k=x,y,z} g_j(t_1) g_k(t_2) \langle r_j(t_1) r_k(t_2) \rangle \qquad \text{linearity of expectation} && (3.29) \\
&= G : R, && (3.30)
\end{aligned}$$

where $G : R$ is the tensor inner product or Frobenius inner product between the following matrices:

$$\begin{aligned}
G &= \begin{bmatrix} g_x(t_1)g_x(t_2) & g_x(t_1)g_y(t_2) & g_x(t_1)g_z(t_2) \\ g_y(t_1)g_x(t_2) & g_y(t_1)g_y(t_2) & g_y(t_1)g_z(t_2) \\ g_z(t_1)g_x(t_2) & g_z(t_1)g_y(t_2) & g_z(t_1)g_z(t_2) \end{bmatrix} \\
&= g(t_1) \otimes g(t_2) = g(t_1)g(t_2)^T = g_1 g_2^T
\end{aligned} \tag{3.31}$$

$$\begin{aligned}
R &= \begin{bmatrix} \langle r_x(t_1)r_x(t_2) \rangle & \langle r_x(t_1)r_y(t_2) \rangle & \langle r_x(t_1)r_z(t_2) \rangle \\ \langle r_y(t_1)r_x(t_2) \rangle & \langle r_y(t_1)r_y(t_2) \rangle & \langle r_y(t_1)r_z(t_2) \rangle \\ \langle r_z(t_1)r_x(t_2) \rangle & \langle r_z(t_1)r_y(t_2) \rangle & \langle r_z(t_1)r_z(t_2) \rangle \end{bmatrix} \\
&= \langle r(t_1) \otimes r(t_2) \rangle = \langle r(t_1)r(t_2)^T \rangle = \langle r_1 r_2^T \rangle
\end{aligned} \tag{3.32}$$

The symbol $\otimes$ denotes the outer product. Each element of this last matrix represents the correlation function, $C(\cdot)$:

$$R_{jk} = \langle r_j(t_1) r_k(t_2) \rangle = C_{jk}(t_1, t_2) = C_{jk}(|t_1 - t_2|) = C_{jk}(|t|). \tag{3.33}$$

Note that, for a stationary process with zero mean, it only depends on the difference between the times t_1 and t_2. R is therefore a covariance matrix.

The cumulant expansion in Eq. 3.16 can be rewritten using the matrices 3.31 and 3.32 as follows, truncated to the second term and assuming diffusion a zero-mean process ($\langle \mathbf{r}(t) \rangle = 0$):

$$\log E(\tau) \approx i\gamma \underbrace{\int_0^\tau \mathbf{g}(t) \cdot \langle \mathbf{r}(t) \rangle \, dt}_{\kappa_1} - \frac{\gamma^2}{2} \Bigg[\underbrace{\int_0^\tau \int_0^\tau \mathbf{g}(t_1) \otimes \mathbf{g}(t_2) : \langle \mathbf{r}(t_1) \otimes \mathbf{r}(t_2) \rangle \, dt_1 dt_2}_{\mu_2} \tag{3.34}$$

$$- \underbrace{\left(\int_0^\tau \mathbf{g}(t) \cdot \langle \mathbf{r}(t) \rangle \, dt \right)^2}_{\kappa_1^2} \Bigg]$$

$$\approx -\frac{\gamma^2}{2} \int_0^\tau \int_0^\tau \mathbf{g}(t_1) \otimes \mathbf{g}(t_2) : \langle \mathbf{r}(t_1) \otimes \mathbf{r}(t_2) \rangle \, dt_1 dt_2. \tag{3.35}$$

An extra assumption can be added: the positions can be described by an uncorrelated random walk, hence they are Gaussian. With this hypothesis, there is no correlation between positions at different time instants:

$$\langle \mathbf{r}(t_1) \otimes \mathbf{r}(t_2) \rangle \neq 0 \iff t_1 = t_2. \tag{3.36}$$

This means that the attenuation only depends on the displacement correlation:

$$\langle \mathbf{r}(t) \otimes \mathbf{r}(t) \rangle. \tag{3.37}$$

Considering that the correlation is different from zero only when $t_1 = t_2$, then

$$\langle \mathbf{r}(t_1) \otimes \mathbf{r}(t_2) \rangle = \langle \mathbf{r}(t_1) \otimes \mathbf{r}(t_2) \rangle \delta(t_1 - t_2) = 2 \min(t_1, t_2) D, \tag{3.38}$$

where the last passage is obtained by inverting the expression of the time-dependent diffusion tensor:

$$\mathbf{D}(t) = \frac{1}{2t} \langle \mathbf{r}(t) \otimes \mathbf{r}(t) \rangle \qquad (\mathrm{m}^2/\mathrm{s}) \tag{3.39}$$

and considering it constant throughout the gradient waveform.

Substituting in eq. 3.35, one obtains:

$$\log E(\tau) = -\frac{\gamma^2}{2} \int_0^\tau \int_0^\tau \mathbf{g}(t_1) \otimes \mathbf{g}(t_2) : \langle \mathbf{r}(t_1) \otimes \mathbf{r}(t_2) \rangle \, dt_1 dt_2 \tag{3.40}$$

$$= -\gamma^2 \int_0^\tau \int_0^\tau \mathbf{g}(t_1) \otimes \mathbf{g}(t_2) : \min(t_1, t_2) \, \mathbf{D} \, dt_1 dt_2. \tag{3.41}$$

Hence,

$$logE(\tau) = -B : D \tag{3.42}$$

where B and D are the B tensor and the Diffusion tensor respectively, which are symmetric.

$$B = \begin{bmatrix} b_{xx} & b_{xy} & b_{xz} \\ b_{yx} & b_{yy} & b_{yz} \\ b_{zx} & b_{zy} & b_{zz} \end{bmatrix} \tag{3.43}$$

$$D = \begin{bmatrix} d_{xx} & d_{xy} & d_{xz} \\ d_{yx} & d_{yy} & d_{yz} \\ d_{zx} & d_{zy} & d_{zz} \end{bmatrix} \tag{3.44}$$

Each element of the B tensor can be expressed as:

$$b_{jk} = \gamma^2 \int_0^\tau \int_0^\tau g_j(t_1) g_k(t_2) \min(t_1, t_2) \, dt_1 dt_2, \tag{3.45}$$

that for a PGSE sequence results in:

$$b = \gamma^2 g^2 \delta^2 (\Delta - \delta/3) = q^2 (\Delta - \delta/3), \tag{3.46}$$

where the factor $\tau = \Delta - \delta/3$ is called diffusion time. The parameter b, known as the *b-value*, quantifies the degree of diffusion weighting applied during the MRI sequence and controls the sensitivity of the MRI signal to diffusion: larger values correspond to stronger diffusion weighting. In more advanced diffusion encoding schemes beyond PGSE, this concept generalizes to the *B tensor*, which captures the full diffusion weighting pattern in all spatial directions.

Note that in general, the diffusion process is considered symmetric. Symmetry means that for each spin having a positive phase contribution, there will be another one with the opposite phase contribution. In case of symmetric diffusion, the magnitude signal is real valued (the imaginary part goes in the phase). The other approximation often used is the Gaussianity. Gaussian diffusion means that water molecules spread out following a Gaussian probability distribution. This assumption holds exactly in free water, where diffusion obeys Einstein's equation [33]. However, in more complex environments with barriers and restrictions—such as biological tissues—this model

serves as an approximation.

3.2. Diffusion signal Analysis

There are two main approaches for analyzing the diffusion MRI signal: signal representations and tissue models. Signal representations are phenomenological and model-independent—they aim to describe the signal itself without making strong assumptions about the underlying tissue, but they lack specificity. A well-known example is the cumulant expansion, described in Sec. 3.1, or the spherical mean (see Sec. 3.2.2). In contrast, tissue models try to infer microstructural properties by fitting an analytical expression to the data, to improve specificity [29]. Any modeling approach relies on a set of assumptions. However, as the number and complexity of these assumptions increase, the generalizability of the model decreases. Consequently, this project aims to choose a model that minimizes the number of hypotheses, increasing robustness and applicability of the findings. To support this approach, an overview of different models and signal representations is given, to highlight differences and justify the final choice.

3.2.1. DTI - Diffusion tensor imaging

Diffusion Tensor Imaging is a method for probing tissue microstructure by measuring the diffusion of water molecules. The key parameter derived from this technique is the diffusion coefficient (or diffusivity), which quantifies how easily water molecules spread through tissue in response to a concentration gradient, typically expressed in units of mm/s. The diffusion tensor models this diffusion behavior, assuming a Gaussian distribution of water molecule displacement [53].

Mathematically, DTI describes the macroscopic diffusion process using a second-order approximation of the cumulant expansion, resulting in a second-order diffusion tensor, as shown in Eq. 3.35 [35]. Therefore, it is classified as a signal representation of the dMRI signal [51]. The diffusion tensor is a 3×3 symmetric matrix (because of the hypothesis of symmetric diffusion), so it has only 6 independent parameters. Therefore, at least 6 diffusion-encoded directions are needed to estimate the tensor, in addition to at least one non-diffusion weighted, also called b_0 [3], image.

The shape of the diffusion tensor changes depending on the type of diffusion. If diffusion is isotropic, then the diffusion tensor is isotropic, because there is no preferred direction. In case of anisotropy, the tensor may be represented with an ellipsoid.

The diffusion tensor captures the overall diffusion properties within a voxel, and it is influenced by both the underlying tissue microstructure and macroscopic tissue organization. The metrics derived from the tensor are described below.

[3]Note that the non-diffusion weighted images will be referred to as b_0 images for the rest of the report.

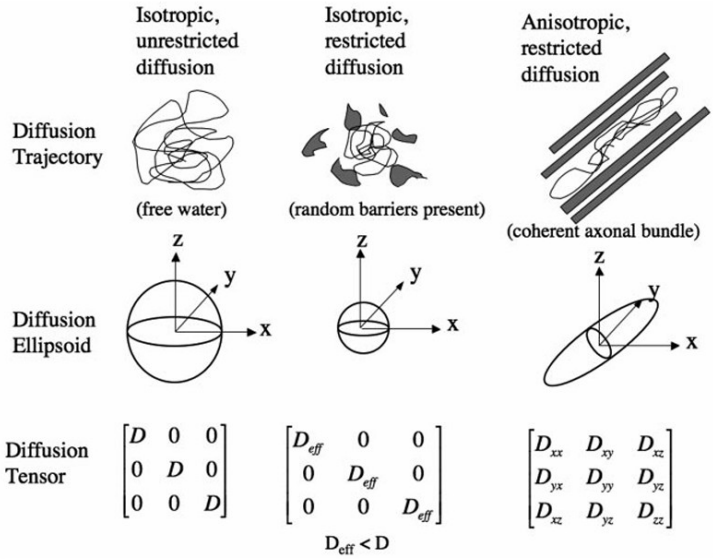

Figure 3.2: Example of diffusion tensor and corresponding shape. Image reproduced from [47].

Eigenvalues and eigenvectors

The eigenvectors are the principal axes of the diffusion tensor and can be found by diagonalizing the tensor.

$$A = \begin{bmatrix} \lambda_1 & 0 & 0 \\ 0 & \lambda_2 & 0 \\ 0 & 0 & \lambda_3 \end{bmatrix} = PDP^{-1} \tag{3.47}$$

where P is the matrix of eigenvectors and $\lambda_1, \lambda_2, \lambda_3$ are the eigenvalues in descending order of magnitude. The largest eigenvector, known as the primary eigenvector, represents the direction of greatest water diffusion, while its corresponding eigenvalue, λ_1, indicates the magnitude of diffusion along that direction. Because this direction aligns with the orientation of the fiber tracts in regions of coherently aligned fibers, λ_1 is often referred to as *axial diffusivity* (AxD, also called *parallel diffusivity*). The second and third eigenvectors are orthogonal to the primary eigenvector and lie within the plane perpendicular to the fiber orientation. Their associated eigenvalues, λ_2 and λ_3, reflect the extent of diffusion in this transverse plane. The average of λ_2 and λ_3 is therefore termed *radial diffusivity* (RD, or *perpendicular diffusivity*), representing diffusion perpendicular to the axonal bundles[47].

Mean Diffusivity

It is the mean of the 3 eigenvalues, it can be interpreted as the directionally averaged diffusivity of water within a voxel [47]. It can be calculated as:

$$\bar{\lambda} = \frac{\lambda_1 + \lambda_2 + \lambda_3}{3} = \frac{trace(D)}{3} \tag{3.48}$$

Fractional anisotropy

Fractional anisotropy (FA) is a measure of the degree of directionality (anisotropy) of the intravoxel diffusivity. It can also be expressed in terms of the difference of each eigenvalue from the mean diffusivity.

$$FA = \sqrt{\frac{1}{2}\frac{(\lambda_1 - \lambda_2)^2 + (\lambda_2 - \lambda_3)^2 + (\lambda_3 - \lambda_1)^2}{\lambda_1^2 + \lambda_2^2 + \lambda_3^2}} \tag{3.49}$$

$$= \frac{\sqrt{\frac{3}{2}}\sqrt{(\lambda_1 - \bar{\lambda})^2 + (\lambda_2 - \bar{\lambda})^2 + (\lambda_3 - \bar{\lambda})^2}}{\sqrt{\lambda_1^2 + \lambda_2^2 + \lambda_3^2}} \tag{3.50}$$

FA ranges from 0 - isotropic diffusion, no directional preference, spherical tensor - to 1 - highly anisotropic diffusion, strong directional preference, ellipsoidal tensor. When the primary eigenvalue is significantly larger than the second and third eigenvalues, the fractional anisotropy will be high, indicating a strong directional preference for diffusion. This corresponds to brighter areas in grayscale FA maps, while darker areas correspond to regions with less directional diffusion [47].

The FA map can also be color-coded to visualize the orientation of the primary eigenvector. In this colorized map, green represents axonal fibers oriented from left to right, red represents fibers oriented from anterior to posterior, and blue represents fibers oriented from inferior to superior. When fibers are oriented between these three cardinal directions, their colors are mixed additively to reflect the combined orientation of the fiber populations [47].

Although DTI remains one of the most widely used methods for analyzing diffusion data due to its speed, it has some drawbacks that can compromise the derived parameters. A major limitation lies in the inability of the tensor model to represent diffusion in regions with complex fiber architecture, such as areas containing crossing or bending fibers or orientation dispersion. In such regions, the tensor model attempts to fit a single ellipsoid to multiple distinct fiber orientations, resulting in a simplified and averaged depiction of the underlying, more complex diffusion patterns—biased by the relative strength and orientation of each fiber population within the voxel. As a result, commonly used scalar metrics—particularly fractional anisotropy —can be misleading, as FA may decrease not due to reduced white matter integrity, but simply due to the presence of multiple competing fiber directions. At the same time, axial and radial diffusivity are also influenced by multiple fiber orientations, and this must be considered when interpreting the results. Moreover, DTI is based on the assumption of Gaussian diffusion, which is not always valid. It also tends to perform poorly in regions affected by partial volume effects, where voxels contain a mixture of different tissue types. Finally, it does not distinguish between multiple tissue compartments, such as intra- and extracellular spaces, providing an average measure of diffusion [35, 76].

3.2.2. Spherical Mean Technique (SMT) based multi-compartment microscopic diffusion model

This model is developed by Kaden et al. in [35]. It accounts for multiple compartments (intra- and extra-neurite) and disentangles the microscopic diffusion features from the neurite orientation.

At the voxel level, the observed signal is modeled as the superposition of contributions from numerous microdomains, which may have complex orientation distributions. Specifically, the diffusion signal of a voxel of this possibly anisotropic media can be written as a spherical convolution between the neurite orientation distribution function (ODF) and the microscopic diffusion signal from an individual neurite [35]. Mathematically, this is expressed as:

$$E(b, n) = \int_{S^2} p(\omega) h(b, n|\omega) d\omega \tag{3.51}$$

where:

- $\omega \in S^2$ (with $S^2 = \{\omega \in \mathbb{R}^3 \mid \|\omega\| = 1\}$) is the rotation axis or orientation of the microscopic tissue geometry[4]. The tissue is assumed to be rotationally invariant about ω.
- $p(\omega)$ is the neurite orientation distribution function, describing how neurites are oriented in space. It quantifies the relative frequency of specific axon orientations within a fiber population.
- n $\in S^2$ is the normalized gradient direction.
- b ≥ 0 is the diffusion weighting.
- $h(b, n|\omega)$ is the impulse response that represents the microscopic diffusion signal along a single neurite whose main diffusion is aligned with ω and that is measured along n.
- The integral represents the spherical convolution, which combines the microscopic diffusion properties with the macroscopic fiber dispersion.
- $E(b, n)$ represents the attenuation, i.e., the diffusion signal.

Spherical mean technique

The Spherical Mean Technique (SMT) is used to analyze microscopic tissue features unconfounded by the neurite orientation distribution. In fact, by averaging the diffusion MRI signal over all gradient directions, while keeping other acquisition parameters fixed, the signal is no longer affected by the macroscopic fiber orientation, allowing for direct estimation of intrinsic microstructural properties such as diffusivities and fractional anisotropy.

[4] In presenting this model, the vector notation follows that used by the original authors. Both n and ω are unit vectors on S^2, and their orientations are typically expressed in spherical coordinates.

Mathematically, the **spherical mean** of the diffusion signal $E(b, n)$ at a given b-value is defined as [36]:

$$\bar{E}(b) = \frac{1}{4\pi} \int_{S^2} E(b, n) d\Omega \tag{3.52}$$

where:

- $E(b, n)$ is the signal measured along a direction n on the sphere.
- $d\Omega$ is the differential solid angle element on the unit sphere S^2, representing all possible diffusion gradient directions.
- $\bar{E}(b)$ is the final signal after removing the effects of fiber orientation.

The proof that the spherical mean signal is independent of the orientation distribution function follows [36]. Substituting Eq. 3.51 into Eq. 3.52 yields the double integral:

$$\bar{E}(b) = \frac{1}{4\pi} \int_{S^2} \left(\int_{S^2} p(\omega) h(b, n|\omega) \, d\omega \right) dn. \tag{3.53}$$

Note that $p(n)$ is omitted because of uniform gradient sampling. Defining the spherical mean of the response function as:

$$\bar{h}(b, \omega) = \frac{1}{4\pi} \int_{S^2} h(b, n|\omega) dn, \tag{3.54}$$

and applying Fubini's theorem to interchange the order of integration results in

$$\bar{E}(b) = \int_{S^2} p(\omega) \left(\frac{1}{4\pi} \int_{S^2} h(b, n|\omega) \, dn \right) d\omega \tag{3.55}$$

$$= \int_{S^2} p(\omega) \, \bar{h}(b, \omega) \, d\omega. \tag{3.56}$$

Since the spherical mean of the impulse response does not depend on fiber orientation ω, and $p(\omega)$ is normalized [36], it follows that

$$\bar{h}(b, \omega) = \bar{h}(b), \tag{3.57}$$

$$\int_{S^2} p(\omega) \, d\omega = 1, \tag{3.58}$$

from which the equality

$$\bar{E}(b) = \bar{h}(b) \tag{3.59}$$

is obtained. Therefore, this is the proof that using SMT, the signal is not influenced by the orientation distribution of the fibers but only by microscopic diffusion properties [36].

Microscopic Diffusion Model

Kaden et al.[35] applies the SMT on a multicompartimental model. This model divides brain tissue into an intra-neurite domain and an extra-neurite compartment. The first consists of dendrites and axons - possibly surrounded by myelin sheath - modeled as cylinders of infinitesimal thickness, called *sticks*. The second compartment is made of neurons, glial cells (oligodendrocytes, neurolemmocytes and astrocytes) and extracellular space. The microscopic diffusion signal for a brain tissue with orientation $\omega \in S^2$ is the weighted sum of intra- and extra-neurite signals:

$$h(b, n|\omega) = f_{int} h^{\text{int}}(b, n|\omega) + (1 - f_{int}) h^{\text{ext}}(b, n|\omega), \tag{3.60}$$

where $f_{\text{int}} \in [0, 1]$ denotes the signal fraction of the intra-neurite compartment, and $f_{\text{ext}} = 1 - f_{\text{int}}$ corresponds to the extra-neurite compartment. The terms $h^{\text{int}}(b, n|\omega)$ and $h^{\text{ext}}(b, n|\omega)$ represent the diffusion signals arising from the intra- and extra-neurite water pools, respectively.

The signal fraction f_{int} can be further expressed as a function of the respective compartmental volume fractions and their transverse relaxation times:

$$\begin{aligned} h(b, n|\omega) = & \left(\frac{v_{\text{int}} e^{-\frac{TE}{T_{2\text{int}}}}}{v_{\text{int}} e^{-\frac{TE}{T_{2\text{int}}}} + v_{\text{ext}} e^{-\frac{TE}{T_{2\text{ext}}}}} \right) h^{\text{int}}(b, n|\omega) \\ & + \left(1 - \frac{v_{\text{int}} e^{-\frac{TE}{T_{2\text{int}}}}}{v_{\text{int}} e^{-\frac{TE}{T_{2\text{int}}}} + v_{\text{ext}} e^{-\frac{TE}{T_{2\text{ext}}}}} \right) h^{\text{ext}}(b, n|\omega) \end{aligned} \tag{3.61}$$

where v_{int} and v_{ext} denote the volume fractions of the intra- and extra-neurite compartments, and $T_{2\text{int}}$ and $T_{2\text{ext}}$ are their corresponding T_2 relaxation times.

This model holds with the following hypotheses:

- no myelin compartment is included because of rapid T_2 relaxation of water between myelin layers, not detectable at long echo times;
- intra- and extra-neurite pools have similar T_2 relaxation;
- intra- and extra-neurite pools are non exchanging compartments;
- transverse microscopic diffusivity is set to 0 for low b-values in intra-neurite pool (only parallel diffusivity in axons), as the attenuation is not detectable

for such a small diameter;

- the transverse microscopic diffusion in the extra-neurite compartment is represented as a function of the intra-neurite volume fraction and intrinsic diffusivity using a first-order approximation of the tortuosity effect (see Eq. 3.64).

It's important to note that this method does not distinguish between the parallel microscopic diffusivities within axons and dendrites and those in the surrounding extra-neurite space, which may differ. Instead, it provides a voxel-averaged estimate that reflects contributions from both compartments.

The intra-neurite diffusion signal is modeled as:

$$h_{\text{int}}(b, n|\omega) = e^{-b\langle n,\omega\rangle^2\lambda} \tag{3.62}$$

where $0 \leq \lambda \leq \lambda_{\text{free}}$ is the intrinsic diffusion coefficient parallel to the neurites, and λ_{free} is the free-water diffusivity. The dot product[5] $\langle n, \omega\rangle^2$ represents the projection of the gradient direction n onto the fiber direction omega.

The extra-neurite tissue compartment could have directionally anisotropic geometry at the micrometer scale. Therefore, it is reasonable to model this signal component using a rotationally symmetric microscopic tensor, characterized by the product of longitudinal and transverse diffusivities.

$$h_{\text{ext}}(b, n|\omega) = e^{-b\langle n,\omega\rangle^2\lambda} e^{-b(1-\langle n,\omega\rangle^2)\lambda_{\perp}^{ext}} \tag{3.63}$$

where $\lambda_{\perp}^{ext}$ is the (extra) transverse diffusivity. The transverse diffusion coefficient $\lambda_{\perp}^{ext}$ is modeled as a function of the intra-neurite volume fraction v_{int} and intrinsic diffusivity λ.

Specifically, the transverse diffusivity is approximated using the first-order tortuosity model, which was derived based on a system of randomly positioned, parallel cylinders with varying diameters and impermeable boundaries. This approximation applies in the long-time diffusion limit and derives from the effective medium theory.

$$\lambda_{\perp}^{ext} = (1 - v_{\text{int}})\lambda \tag{3.64}$$

Spherical Mean diffusion signal model

Given the microscopic diffusion model, one can calculate the spherical mean of the attenuation signal:

$$\bar{E}(b) = f_{\text{int}}\bar{E}(b)^{\text{int}} + (1 - f_{\text{int}})\bar{E}(b)^{\text{ext}} \tag{3.65}$$

where:

[5]Note that only in this model, $\langle\cdot,\cdot\rangle$ denotes a dot product, following the notation in [35]. Elsewhere in this report, $\langle\cdot\rangle$ indicates an average.

- v_{int} is the intra-neurite signal fraction;
- $\bar{E}(b)^{\text{int}}$ is the intra-neurite spherical mean:

$$\bar{E}(b)^{\text{int}} = \frac{\sqrt{\pi}\,\text{erf}\left(\sqrt{b\lambda}\right)}{2\sqrt{b\lambda}}; \tag{3.66}$$

- $\bar{E}(b)^{\text{ext}}$ is the extra-neurite spherical mean :

$$\bar{E}(b)^{\text{ext}} = \exp(-b\lambda_{\perp}^{\text{ext}}) \cdot \frac{\sqrt{\pi}\,\text{erf}\left(\sqrt{b(\lambda - \lambda_{\perp}^{\text{ext}})}\right)}{2\sqrt{b(\lambda - \lambda_{\perp}^{\text{ext}})}}; \tag{3.67}$$

- erf() is the error function (already in closed form).

From Equation 3.65, the parameters f_{int} and λ can be found by implementing a nonlinear Least Squares optimization. Since there are two unknown parameters, only two shells are needed [35].

The model developed by [35, 36] is simple and intuitive, but it has several assumptions that constrain it to specific conditions. One of the strongest hypotheses is the tortuosity assumption (Eq. 3.64).

3.3. From Kaden et al. model to approaches with less assumptions in the high b-values regime

To address the limitations of DTI and the Kaden et al. model [35], a possible direction forward is offered by Pizzolato et al. [58], who propose working at high b-values to eliminate the extra-axonal compartment and limit the hypotheses. Once one has estimated the parameters of the axonal compartment, it is possible to go back to the bicompartimental model and obtain the parameters for the extra-axonal compartment with nonlinear optimization. In their work, [58] used a PGSE sequence, which is the quintessential implementation of a Single Diffusion Encoding (SDE) sequence. Using the same high b-value regime, a more complex encoding can be implemented, to improve tissue characterization beyond what is possible with the classic PGSE-based SDE. In fact, even if SDE is widely used in diffusion MRI, it possesses a series of limitations. While SDE is generally sensitive to parallel diffusivity, this sensitivity decreases significantly at high b-values when spherical mean techniques are applied. As a result, detecting parallel diffusivity with SDE becomes challenging unless advanced modeling strategies, such as zonal modeling, are used [58]. In contrast, Multiple Diffusion Encoding (MDE) methods—specifically Triple Diffusion Encoding—maintain sensitivity to parallel diffusivity at high b-values, even when spherical mean approaches are employed. Moreover, signal multi-compartmental modeling with SDE is often ill-posed, even when the number of compartments is small, leading to low accuracy and precision in parameter estimates. For example,

bicompartmental models like NODDI [79] exhibit biased parameter fits because the objective function to minimize contains two local minima [29]. MDE techniques such as TDE help resolve degeneracies in multi-compartment models and validate model constraints without relying solely on strong assumptions [26].
These limitations motivate the use of TDE acquisition schemes, which apply diffusion-sensitizing gradients along multiple axes within the same acquisition. This approach ensures that only spins experiencing correlated displacements across multiple directions contribute to the signal, thereby introducing inter-dimensional correlations—something not achievable with SDE.

In these more complex and general encoding schemes, the b-values assume a more general form that derives from the $\mathbf{q}(t)$ vector:

$$\mathbf{q}(t) = \gamma \int_0^t \mathbf{g}(t')\, dt', \tag{3.68}$$

$$B = \int_0^\tau \mathbf{q}(t)\mathbf{q}(t)^{\mathrm{T}}\, dt, \tag{3.69}$$

where B is called the measurement tensor and τ is the echo time. Eq. 3.69 shows that the trajectory of $\mathbf{q}(t)$ determines the shape of the B-tensor [78].

More complicated implementations are also possible, for instance, the one proposed by Sjolund et al. [68]. Their framework aims at finding the gradient waveforms that minimize TE, to maximize the SNR, given as input the tensor encoding wanted (e.g, spherical, prolate, cigar, etc.), the maximum gradient strength, sample points, and timing of the sequence. As a result, the gradient waveform obtained will not have the classic 'diffusion-gradient-shape', such as that of the PGSE, but it will have an oscillating shape. This minimal TE is beneficial because it minimizes the attenuation, increasing the SNR; however, the definition of diffusion time is more difficult to grasp in this new setting.

3.3.1. Triple Diffusion Encoding scheme

In this section, the triple diffusion encoding proposed by Ramanna et al. [61] is described and extended. The work aims at estimating the diffusion tensors of intra- and extra-axonal spaces, together with axonal signal fraction, with only mild assumptions and without a complex fitting procedure.

Their method is based on 4 hypotheses. First, water exchange between the intra- and extra-axonal compartments is assumed to be negligible over the timescale of diffusion MRI measurements, which typically spans tens of milliseconds. Second, the contribution of the dMRI signal from water within the myelin sheath is considered insignificant, due to its short T_2. Third, axons are idealized as thin, straight cylinders to simplify the modeling, with zero diameter. Fourth, the applied diffusion weighting is assumed to be sufficiently strong (higher than 4000 s/mm^2 in vivo) to largely suppress the dMRI signal from extra-axonal water, remaining only with intra-axonal signal. They perform two acquisitions, one at high b-values to estimate intra-axonal

diffusion, and one at lower b-value to estimate the total diffusion tensor and then derive the extra-axonal diffusion tensor.

The differences introduced by this project are the absence of the simplification on a zero axon diameter ($D_\perp$ is different from 0) and the focus on intra-axonal diffusivities, neglecting the low b-values acquisitions to estimate the extra-axonal one. Compared to previous models, this approach is more robust because it does not make any assumptions about the parameters to estimate.

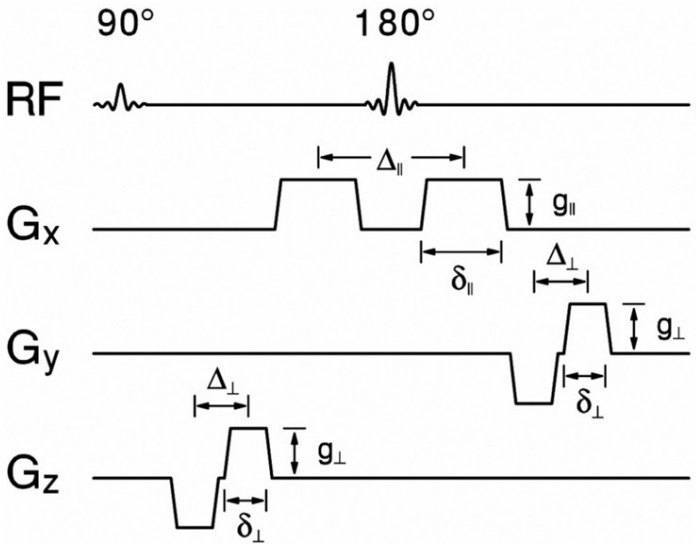

Figure 3.3: Example of triple diffusion encoding sequence. The axial diffusion gradients are oriented along the x-axis, whereas the radial gradients are applied along the y- and z-axes. Reproduced from [61].

Fig. 3.3 shows the pulse sequence diagram, which is the same used in this Master Thesis. After the 90° pulse, a set of radial gradients is applied, followed by the axial ones, divided by the 180° pulse, and by the axial pair. By sending these 3 gradient pairs, only the population of spins that have diffused along any of these 3 directions will contribute to the signal. The axial direction is associated with the largest b-value, called $b_{//}$. The radial directions have a smaller and equal b-value, $b_\perp$, yielding an axisymmetric B-tensor. The B-tensor is prolate and described by the following matrix:

$$B = \begin{bmatrix} b_{//} & 0 & 0 \\ 0 & b_\perp & 0 \\ 0 & 0 & b_\perp \end{bmatrix} \tag{3.70}$$

In this case

$$b_i = \gamma^2 g_i^2 \delta_i^2 (\Delta - \frac{1}{3}\delta_i), \tag{3.71}$$

where i can be parallel or perpendicular.

With this B-tensor, and no simplifications on zero axon diameter as in [31], the

spherically averaged signal [6] can be expressed as [18]:

$$\bar{S}(b_{\parallel}, b_{\perp}) = C\frac{\sqrt{\pi}}{2}e^{-b_{\parallel}D_{\perp}-b_{\perp}D_{\parallel}-b_{\perp}D_{\perp}}\frac{erf\left\{\sqrt{(b_{\parallel}-b_{\perp})(D_{\parallel}-D_{\perp})}\right\}}{\sqrt{(b_{\parallel}-b_{\perp})(D_{\parallel}-D_{\perp})}}. \tag{3.72}$$

The constant C represents the axonal signal fraction (ASF). Note that the notation D, rather than λ, as used in Section 3.2.2, was adopted for diffusivity to follow the style of the original model authors and to emphasize that these are distinct parameters.
In the following, it is reported a series of simplifications proposed by Associate Professor Marco Pizzolato aimed at identifying the minimal set of acquisitions required to estimate both axial and radial diffusivities from Eq. 3.72, as well as the constant C. In fact, at high b-value the equation can be approximated as

$$\bar{S}(b_{\parallel}, b_{\perp}) \approx C\frac{1}{\sqrt{b_{\parallel}-b_{\perp}}}e^{-b_{\parallel}D_{\perp}-b_{\perp}(D_{\parallel}+D_{\perp})}\sqrt{\frac{\pi}{4(D_{\parallel}-D_{\perp})}}, \tag{3.73}$$

whenever $(b_{\parallel}-b_{\perp})(D_{\parallel}-D_{\perp})$ is sufficiently high, because the error function will tend to 1 [31].

According to Eq. 3.73, if a TDE encoding is acquired together with a SDE, their ratio becomes

$$\frac{\bar{S}(b_{\parallel}, b_{\perp})}{\bar{S}(b_{\parallel}, 0)} \approx \frac{\sqrt{b_{\parallel}}}{\sqrt{b_{\parallel}-b_{\perp}}}e^{-b_{\perp}(D_{\parallel}+D_{\perp})}. \tag{3.74}$$

In this Eq. 3.74, the unknown variable is $(D_{\parallel}+D_{\perp})$. This approach differs from the one of [61], as the axonal diffusivity cannot be estimated directly, but only the sum of parallel and perpendicular diffusivity can, because of the absence of the assumption on zero axon diameter. Such sum will be named J.

$$J = D_{\parallel} + D_{\perp} \tag{3.75}$$

The perpendicular diffusivity $D_{\perp}$ can be estimated using two single diffusion encodings at high b-values as shown in [58]. Each of them will give the following signals:

$$\bar{S}(b^1_{\parallel}, 0) \approx \frac{1}{\sqrt{b^1_{\parallel}}}e^{-b^1_{\parallel}D_{\perp}}\sqrt{\frac{\pi}{4(D_{\parallel}-D_{\perp})}} \tag{3.76}$$

and

$$\bar{S}(b^2_{\parallel}, 0) \approx \frac{1}{\sqrt{b^2_{\parallel}}}e^{-b^2_{\parallel}D_{\perp}}\sqrt{\frac{\pi}{4(D_{\parallel}-D_{\perp})}}. \tag{3.77}$$

Hence, their ratio this time becomes:

[6] More on spherical mean signal in Sec. 3.4.

$$\frac{\bar{S}(b_{\parallel}^2, 0)}{\bar{S}(b_{\parallel}^1, 0)} = \sqrt{\frac{b_{\parallel}^1}{b_{\parallel}^2}} e^{D_{\perp}(b_{\parallel}^1 - b_{\parallel}^2)} \tag{3.78}$$

where the only unknown is $D_{\perp}$ and can be easily obtained. Then, $D_{\parallel}$ is calculated as:

$$D_{\parallel} = J - D_{\perp}. \tag{3.79}$$

It follows that in order to estimate the diffusivities a minimum of three acquisitions is needed. Moreover, once the parallel and perpendicular diffusivities are found, the axonal signal fraction C can be derived. For example, if either of the SDE signals is expressed as a spherical mean, one obtains:

$$\bar{S}(b_{\parallel}, 0) = C \frac{\sqrt{\pi}}{2} e^{-b_{\parallel} D_{\perp}} \frac{erf\left\{\sqrt{(b_{\parallel}(D_{\parallel} - D_{\perp})}\right\}}{\sqrt{b_{\parallel}(D_{\parallel} - D_{\perp})}}. \tag{3.80}$$

Upon inversion of Eq. 3.80, the axonal signal fraction C can be easily derived.

3.4. T_2 fitting and spherical variance technique

One important parameter in dMRI is the tissue relaxation time, T_2. Maps that register the value for each voxel are produced, and any alteration of this parameter can suggest a pathological state. It is therefore important that these maps are as accurate and as specific as possible. Using a strong diffusion-weighted signal, the signal contribution only comes from the more diffusion-restricted components, such as the axons. However, diffusion is also restricted in cell nuclei and vacuoles. The signal is therefore obtained by the combination of axons, cell nuclei and vacuoles. In the following paragraphs, two methods for deriving T_2 are described. The first, developed by McKinnon and Jensen [42], accounts for all tissue components. The second, proposed by Pizzolato et al. [57], aims to estimate only the axonal T_2, excluding contributions from other isotropic compartments.

3.4.1. Spherical mean T_2

This technique is developed by McKinnon and Jensen in [42]. T_2 can be estimated from the spherical mean of two diffusion-weighted signals acquired at the same high b-value, but different TEs (that must be long enough to neglect the contribution of myelin):

$$T_{2m} = \frac{\mathrm{TE}_2 - \mathrm{TE}_1}{\log\left(\frac{\bar{S}(\mathrm{TE}_1, b)}{\bar{S}(\mathrm{TE}_2, b)}\right)}. \tag{3.81}$$

The T_2 obtained from Eq. 3.81 accounts for both anisotropic (axons) and isotropic

(cells) diffusion-restricted components. Moreover, T_2 estimates based on the spherical mean can be more affected by partial volume contamination with isotropic signal contributions from the gray matter [57]. As a result, this method does not achieve a precise estimate of axonal T_2.

3.4.2. Spherical variance T_2

This technique, proposed by [57], provides an estimate of axonal T_2 based on the spherical variance of the signal, removing the bias from isotropic components. The spherical variance is the variance of the diffusion signal sampled along multiple directions on a diffusion shell with fixed b-value. Since isotropic components contribute equally across all directions, they affect only the signal's mean and do not influence the spherical variance.

The directional signal measured in a voxel at high b-value can be modelled as the sum of isotropic and anisotropic (axonal) contributions:

$$S(\mathrm{TE}, b, \vec{n}) \approx f_{\mathrm{iso}} S_{\mathrm{iso}}(b, \vec{n}) e^{-\mathrm{TE}/T_{2\mathrm{iso}}} + f_a S_a(b, \vec{n}) e^{-\mathrm{TE}/T_{2a}} \tag{3.82}$$

where a stands for axonal and iso for isotropic, f_a, f_{iso} are their relative signal fractions (volume fractions modulated by proton density and longitudinal relaxation), and S_{iso} and S_a are the diffusion attenuations. The terms T_{2a} and $T_{2\mathrm{iso}}$ denote the transverse relaxation times for the axonal and isotropic compartments, respectively, accounting for the signal decay as a function of echo time (TE).
The signal's spherical variance can be expressed as:

$$\begin{aligned} \mathrm{var}\{S(\mathrm{TE}, b)\} &= \frac{1}{N} \sum_{i=1}^{N} \left(S(\mathrm{TE}, b, \vec{n}_i) - \frac{1}{N} \sum_{k=1}^{N} S(\mathrm{TE}, b, \vec{n}_k) \right)^2 \\ &= \frac{f_a^2}{N} e^{-2\mathrm{TE}/T_{2a}} \sum_{i=1}^{N} \left(S_a(b, \vec{n}_i) - \frac{1}{N} \sum_{k=1}^{N} S_a(b, \vec{n}_k) \right)^2, \end{aligned} \tag{3.83}$$

where the isotropic contribution cancels out, as the directional isotropic signal is equal to its mean.

Using the spherical variance (Eq. 3.83) rather than the spherical mean, the axonal T_2 can be estimated as follows:

$$T_{2\nu} = T_{2a} = \frac{2(\mathrm{TE}_2 - \mathrm{TE}_1)}{\log\left(\frac{\mathrm{var}\{S(\mathrm{TE}_1, b)\}}{\mathrm{var}\{S(\mathrm{TE}_2, b)\}}\right)}. \tag{3.84}$$

In this case, the T_2 can be estimated without any influence of vacuoles and cells.

However, the variance is an estimator that is more sensitive to noise. Modeling the noise as zero-mean Gaussian distributed noise with variance σ^2 implies that the measured signal variance is the sum of the true signal variance and the noise variance, that is,

$$\mathrm{var}\{S(\mathrm{TE}, b)\} + \sigma^2.$$

Since the noise variance is not perfectly known, it is crucial to apply denoising procedures before using Eq. 3.84. However, if the noise is not fully removed, a practical alternative is to model the signal over a single shell using spherical harmonics and suppress noise, for example through Laplace-Beltrami regularization. This type of regularization penalizes higher-order coefficients, which are typically associated with high-frequency noise, more strongly than lower-order ones.

The signal can be expanded in spherical harmonics as:

$$S(\mathrm{TE}, b, \vec{n}) = \sum_{l=0,\mathrm{even}}^{L} \sum_{m=-l}^{l} c_{lm}(\mathrm{TE}, b) Y_l^m(\vec{n}) \tag{3.85}$$

where $Y_l^m(\vec{n})$ are the real spherical harmonics of order l and degree m (due to the antipodal symmetry of the diffusion signal, only even values of l are considered) $c_{lm}(\mathrm{TE}, b)$ are the corresponding coefficients [80].

Using this expansion, the spherical variance used in Eq. 3.83 can be computed as:

$$\mathrm{var}\{S(\mathrm{TE}, b)\} = \frac{1}{4\pi} \sum_{\substack{l=2 \\ \mathrm{even}}}^{L} \sum_{m=-l}^{l} c_{lm}(\mathrm{TE}, b)^2 \tag{3.86}$$

$$= \frac{1}{4\pi} \left(\sum_{m=-2}^{2} c_{2m}(\mathrm{TE}, b)^2 + \sum_{m=-4}^{4} c_{4m}(\mathrm{TE}, b)^2 + \sum_{m=-6}^{6} c_{6m}(\mathrm{TE}, b)^2 + \cdots \right). \tag{3.87}$$

The findings of [57] show that the spherical variance estimator is more reliable compared to the spherical mean technique. A comparison between the spherical mean and variance-based T_2 values can, in principle, reveal whether isotropic and anisotropic microstructures coexist within a voxel and contribute non-negligibly to the signal.

3.5. Axonal Pathology of Alzheimer's disease

This section focuses on the axonal pathology present in Alzheimer's disease.

Alzheimer's disease is the primary cause of dementia. The neuropathological hall-

marks of AD include i) the accumulation of amyloid-β plaques, ii) the formation of neurofibrillary tangles (NFTs) composed of hyperphosphorylated tau protein, iii) progressive synaptic and neuronal loss, and iv) chronic activation of microglia [11]. The pathology typically begins in the medial temporal lobe but gradually spreads to involve nearly all brain regions, resulting in widespread brain atrophy [22].

3.5.1. Amyloid-β and tau protein

The AD brain is characterized microscopically by the combined presence of two classes of abnormal structures, extracellular amyloid plaques and intraneuronal neurofibrillary tangles, both of which comprise highly insoluble, densely packed filaments. The soluble building blocks of these structures are amyloid-β peptides for plaques and tau for tangles. Amyloid-β peptides are proteolytic fragments of the transmembrane amyloid precursor protein [7]. APP is synthesized in the endoplasmic reticulum (ER) and subsequently transported to the Golgi complex, where it undergoes maturation. Once mature, APP is delivered to the plasma membrane, where it is sequentially cleaved by the successive action of the β-secretase and γ-secretase to generate Aβ. Usually, this protein is cleared quickly but, in pathological state, the balance is altered and Aβ accumulates in the extracellular space [52]. This can be due to a genetic mutation, aging, impaired Fast Axonal Transport (FAT), etc. Under normal conditions, APP plays roles in neurotransmission, vesicle transport, and maintaining cellular energy levels. Tau, instead, is a microtubule-associated protein predominantly located in axons, where it stabilizes the cytoskeleton and regulates axonal transport [6].

In the context of AD, Aβ aggregates disrupt membrane integrity and signaling, while hyperphosphorylated tau detaches from microtubules, leading to cytoskeletal instability, impaired FAT, and ultimately axonal degeneration [6].

Studies have shown that tau and Aβ work together in the pathogenesis [7, 14], independently of their accumulation into plaques and tangles, to drive healthy neurons into the diseased state, and that hallmark toxic properties of Aβ require tau. For example, soluble extracellular Aβ species have been identified as the cause of acute neuron death, delayed degeneration, and synaptic dysfunction when soluble cytoplasmic tau is present. This supports the idea that Aβ acts upstream of tau in the pathogenesis of AD, initiating tau's conversion from a physiological to a pathological form. At the same time, it was also found that toxic forms of tau can, in turn, amplify the toxicity of Aβ in a feedback loop. Both Aβ and tau oligomers are capable of self-propagation and spreading through the brain via prion-like mechanisms [22]. Therefore, effective therapeutic strategies should aim to detect and neutralize these toxic soluble species early—before the formation of plaques and tangles and prior to the onset of cognitive decline.

3.5.2. The myelin model

Among the two previously described molecules, research efforts have predominantly focused on amyloid plaques, culminating in the FDA's recent approval of an anti-

amyloid-beta protofibrils antibody, intended to slow the progression of Alzheimer's disease [14]. However, as highlighted in [14], this emphasis has often overshadowed the essential physiological roles of Aβ and tau proteins within axons. Moreover, Bartzokis [6] proposes to read Aβ and tau deposits as by-products of the homeostatic myelin repair process. In the myelin model of AD, the development, maintenance, and eventual breakdown of myelin sheaths are central to the understanding of how the disease progresses. In this section, an overview of axonal pathology in the myelin model and its connection to Aβ and tau is given, as described by Bartzokis [6] and Dan and Zhang [14], highlighting how axons undergo damage during the early stages of AD and exert a pivotal influence on disease progression.

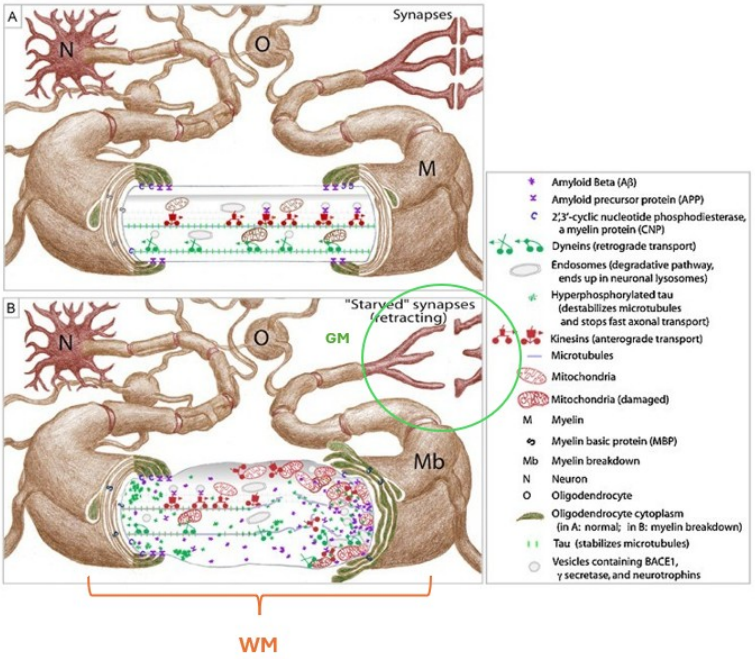

Figure 3.4: Myelin model. Top—healthy axon with intact fast axonal transport (FAT). Bottom—axon exhibiting myelin damage, swollen morphology, impaired FAT in WM, and synaptic starvation in GM. Adapted from [6].

Axons are fundamental components of the nervous system, not only for conducting electrical impulses but also for transporting synaptic materials and energy over long distances. Beyond transmitting signals from the soma to the synapse, axons are believed to have intrinsic computational properties that allow them to fine-tune and regulate neural signaling with remarkable precision. To maintain continuous electrical activity, axons require uninterrupted delivery of energy and molecular cargo. This depends on efficient axonal transport systems and the structural integrity of key components such as the axon initial segment, nodes of Ranvier, and the myelin sheath, as well as their interactions with glial cells like oligodendrocytes and microglia. In particular, myelin allows for high-speed signal conduction and supports the metabolic needs of long-range axons. Given their complex architecture and metabolic demands, axons are especially vulnerable to disruption.

Axonal degeneration is a hallmark of many neurodegenerative diseases. Growing evidence suggests that axonal injury occurs at early stages in Alzheimer's disease

and plays a central role in its progression. In fact, regional WM integrity correlates more closely with cognitive performance, particularly in episodic memory, semantic processing, and executive function, than cortical thickness[14].

Fast Axonal Transport (FAT) and Axonal Swelling

A crucial mechanism that links myelin damage to neuronal dysfunction is the disruption of FAT. FAT is responsible for delivering proteins, organelles, and signaling molecules between the cell body and synapses. This process depends on intact microtubules—hollow, cylindrical components of the cytoskeleton that provide structural support and serve as tracks for intracellular transport. Microtubules are stabilized by proteins such as tau, which bind along their surface to maintain their stability [12].

Damage to oligodendrocytes and myelin can impair FAT. One response to myelin injury involves a localized slowdown or blockage of axonal transport, possibly as part of an intrinsic repair mechanism aimed at restoring the damaged myelin segment. Notably, reductions in axonal transport rates have been observed in transgenic models of Alzheimer's disease even before the appearance of amyloid plaques [6].

Impaired FAT leads to the accumulation of transported cargo—including proteins and organelles—within the axon, producing characteristic axonal swellings at sites of myelin disruption. Initially, these swellings may represent a transient and reversible state reflecting ongoing attempts at remyelination. However, if the repair process is prolonged or unsuccessful, persistent transport blockages deprive distal axons and synapses of essential metabolic support. Interestingly, even in regions where myelin appears macroscopically intact, subtle and ongoing repair attempts may still reduce FAT, potentially leading to an underestimation of the role that myelin vulnerability and repair play in central nervous system disorders.

Studies have shown that myelin damage may contribute to tau hyperphosphorylation, particularly during the remyelination process [54, 62]. Furthermore, higher levels of myelin have been associated with greater resistance to tau pathology in Alzheimer's disease [62]. Once tau becomes hyperphosphorylated, it detaches from microtubules, destabilizing the cytoskeleton and further exacerbating the slowing of FAT. As a result, transport cargos such as amyloid precursor protein (APP) accumulate in regions where toxic tau is present, leading to axonal swelling. This APP accumulation may increase local Aβ production.

The disruption affects not only anterograde transport (from the soma to the synapse) but also retrograde transport, which is responsible for carrying neurotrophic signals back to the cell body. The failure of retrograde transport prevents neurons from receiving critical survival signals and functional feedback from their target regions, further compromising neuronal health and network integrity.

If the repair process fails, these swellings may rupture, leading to the extracellular release of Aβ at the site of the axonal swellings rather than at the synapses. These Aβ aggregates can bind to synaptic receptors, lipids and cholesterol, further exacerbating neuronal and myelin damage with the eventual development of a mature

neuritic plaque.

Bartzokis [6] thus frames Aβ and tau accumulation not as primary causes, but as downstream consequences of repeated, unsuccessful myelin repair.

The loss of myelin impairs the brain's ability to maintain the high-frequency action potentials necessary for initiating long-term potentiation (LTP), a key process in memory formation. At the same time, disruptions in fast axonal transport may delay or block the delivery of proteins essential for LTP—affecting both the forward movement of synaptic components and the backward signaling of neurotrophic factors. These deficits in myelin repair may help explain why memory loss commonly emerges as the first and most persistent sign of Alzheimer's disease, preceding clinical diagnosis by years [6].

3.6. Rat brain anatomy and AD

The AD theory presented in Sec. 3.5 was investigated using the rat brain as a model system. This section provides a brief anatomical overview of the rat brain, presented in the classical anatomical planes used in neuroimaging: horizontal, coronal, and sagittal (see Fig. 3.5). The images are taken from the Waxholm Space (WHS) Rat Brain Atlas [38], a high-resolution 3D atlas of the adult rat brain that includes detailed anatomical mapping of both brain regions and major white matter fiber tracts. The atlas segments the brain into 222 labeled regions, including the cerebral cortex, hippocampal formation, striatopallidal structures, midbrain dopaminergic nuclei, thalamic cell groups, auditory system, and major WM bundles.

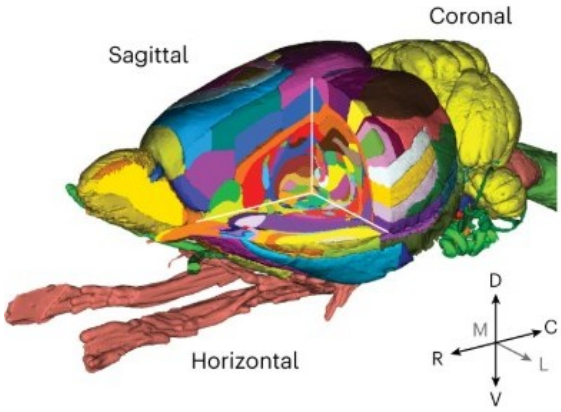

Figure 3.5: 3D surface visualizations from the WHS atlas [38] illustrating standard anatomical planes: coronal, sagittal, and horizontal. Image reproduced from [38].

In this project, the main structure of interest is the corpus callosum, a bundle of nerve fibers joining the two hemispheres of the brain. It is the largest white matter tract in the brain and is hypothesized to play a primary role in cognition [27]. Changes in WM parameters such as diffusivity and axonal fraction are investigated, expecting differences in AD with respect to the physiological state. To study the corpus callosum, coronal slices are used, as this plane provides a better visualization

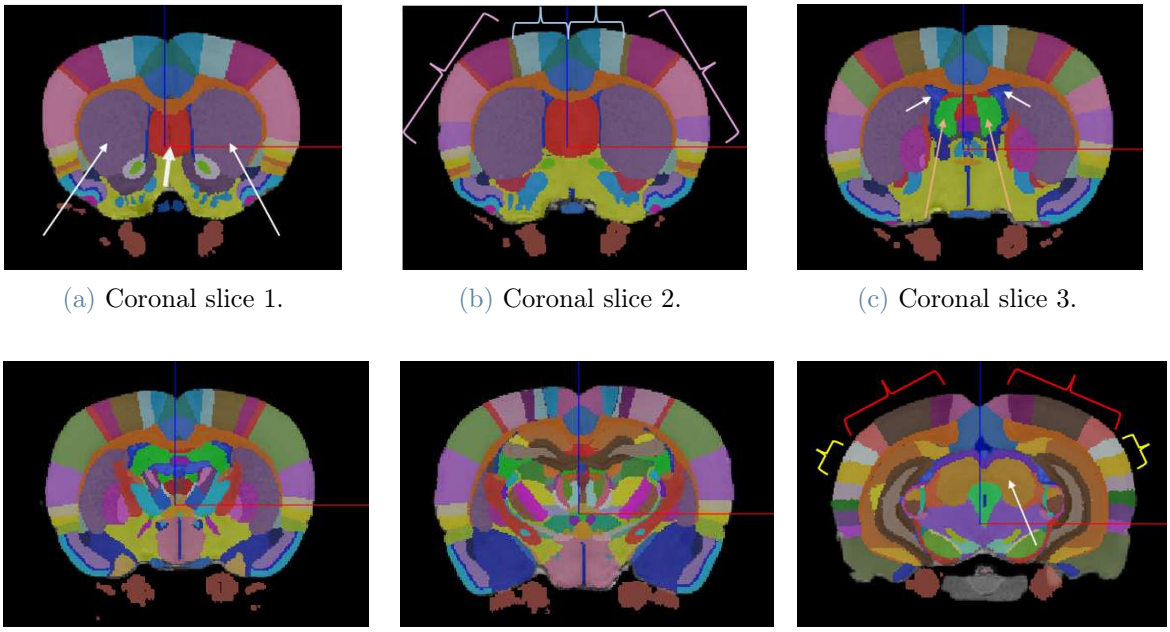

(a) Coronal slice 1. (b) Coronal slice 2. (c) Coronal slice 3.

(d) Coronal slice 4. (e) Coronal slice 5. (f) Coronal slice 6.

Figure 3.6: Six coronal slices of the rat brain arranged from rostral to caudal, illustrating anatomical changes along the anterior–posterior axis. Arrows and parentheses highlight the main brain structures described above. Adapted from [38].

of its morphology. Fig. 3.6 displays six WHS-segmented coronal slices, arranged from rostral to caudal. One can see that the corpus callosum, marked as orange, gets thinner moving caudally, eventually dividing in two branches. A variety of key brain structures can be identified across the slices, indicated by arrows and parentheses. In Fig. 3.6a, the two symmetrical violet structures correspond to the caudate putamen, while the red region marks the septal area. The light blue bands represent the primary motor cortex, and the neighboring darker blue bands indicate the secondary motor cortex. Adjacent to these motor areas lies the somatosensory cortex.

In Fig. 3.6c, the blue triangular structures are the lateral ventricles, and the green semicircles correspond to the fimbria of the hippocampus.

Moving further caudally, the cortical areas change. In Fig. 3.6f, the visual cortex is shown in purple, coral red, and brown, while the auditory cortex appears in ochre and gray. The central midbrain structure in this slice is the superior colliculus.

3.6.1. Rat model

In this section the transgenic rat model used is described.

The present work studies AD on the TgF344-AD rat model developed by Cohen et al. [11]. This double transgenic model co-expresses two human gene mutations: human amyloid precursor protein (hAPP) with the Swedish mutation and human presenilin-1 (hPSEN1) with Δ exon 9 deletion. Each mutation is independently associated with early-onset familial AD.

The model was chosen because TgF344-AD rats manifest a full spectrum of age-dependent AD-like neuropathology, including extracellular amyloid-beta plaque accumulation, tau hyperphosphorylation, gliosis, apoptotic neuronal loss in the hippocampus and cortex, and progressive cognitive decline [7], resembling the disease in humans [25, 50].
At early stages, subtle disruptions in brain connectivity and synaptic activity are present before visible plaque formation. As the disease progresses, more pronounced alterations in neurochemical balance, network dynamics, and brain structure appear. For example, $A\beta$ accumulation begins around six months of age and increases with time. Elevated tau phosphorylation is also observed early, even preceding substantial plaque deposition. By later stages, widespread neurodegeneration, glial activation, and cognitive deficits become evident [50].
Given the symptoms it manifests, the TgF344-AD model provides a valuable preclinical tool to study the temporal evolution of AD pathology. It enables investigation of both gray and white matter alterations, including neuronal degeneration and axonal pathology. By studying this model with ex vivo dMRI, it may be possible to detect early microstructural damage linked to tau-driven processes, which may precede and predict later-stage cognitive decline [50]. However, despite its strengths, this model has limitations. Reflects a familial, mutation-driven form of AD, while the vast majority of human AD cases are sporadic and multifactorial in origin. As such, the TgF344-AD model may not fully replicate the complex etiology or the heterogeneity seen in late-onset sporadic AD [50]. Nonetheless, it remains a highly informative tool for dissecting disease mechanisms, testing imaging biomarkers, and establishing translational relevance to human AD.

[7] A key behavioral symptom of AD—spatial memory impairment—can be assessed in rodents and is detectable in TgF344-AD rats from as early as 4–6 months of age.

4 | Methods

This chapter describes the experimental setup and design choices.

4.1. Sample preparation

The procedure used to prepare the sample is detailed below.

The sample consisted of female rat brains that were extracted at two distinct ages: 4 months and 17.5 months. These time points were selected to represent early and advanced stages of brain aging. The sample included both healthy control rats and rats exhibiting Alzheimer's-like symptoms, allowing for comparisons between normal aging and Alzheimer's disease pathology. The Alzheimer's rats were labeled as Tg/Tg (transgenic), where the double notation indicates that both alleles carry the transgene. Non-Alzheimer's rats were marked WT/WT (wild type). Heterozygous Tg/WT rats were also available but were excluded from the study, as a more pronounced Alzheimer's phenotype is expected in homozygous Tg/Tg animals.

The final dataset used in this project consisted of three WT/WT and three Tg/Tg rats at 4 months of age, and one Tg/Tg rat at 17.5 months. Each subject is identified by a unique ID, as listed in Table 4.1.

Rat type	**SubjID**
WT/WT rat 4 months	RA89, RA87, RA.BML.3841
Tg/Tg rat 4 months	RA71, RA76, RA86
Tg/Tg 17.5 months	RA114

Table 4.1: Subjects grouped by rat type and age.

The tissues were perfusion-fixed with 50 mL sodium phosphate buffer (SøPB), followed by 100 mL of 4% paraformaldehyde (PFA). After perfusion, the tissues were immersion-fixed in 4% PFA. Through protein cross-linking, chemical fixation effectively stops autolytic breakdown and maintains tissue structure. It is fundamental to reduce at its minimum the post-mortem interval (PMI), to maintain tissue integrity and limit the process of autolysis, such as myelin loosening and decreased anisotropy. Perfusion fixation usually acts on the cardiac system, using the intact blood vessels to flush fixatives throughout the tissue upon animal sacrifice. In this way, the fixative distribution is homogeneous throughout the body and the blood is removed efficiently. In this procedure, SøPB is first perfused to clear the blood and stabilise the pH. Then, PFA is perfused to chemically fix the tissue in situ.

Immersion-fixation instead is a technique where the tissue is immersed in a fixative solution (PFA) and the fixative will passively diffuse throughout the tissue over a period of time, to ensure complete fixation. This technique, however, increases the risk of autolytic effects [64].

As a consequence of chemical fixation, diffusivity decreases by a factor of 2 to 5 times at room temperature. This implies that higher b-values are needed to keep the product bD constant (from Eq. 3.42 in scalar form) and match the attenuation of an in vivo protocol. If the diffusivity decreases, also diffusion distances proportional to $\sqrt{Dt}$ follow the same pattern. Only increasing diffusion time keeps the same distances covered [64].

Schilling et al. [64] reports that some diffusion MRI studies on fixed tissue have identified an additional signal component in white matter, referred to as "isotropically-restricted water" or the "dot compartment," which is generally absent in vivo except in regions such as the cerebellum. Recent work [75] has further shown that the signal fraction of this fully restricted diffusion compartment is strongly temperature-dependent, exhibiting a significant increase when tissue temperature falls below approximately 32°C. Given that ex vivo measurements are performed at room temperature, it is important to acknowledge that this dot compartment is present and could bias the measurements.

In addition, fixation alters the relaxation rates, substantially decreasing T_1 and T_2.

The sample was placed in a test tube as seen in Fig. 4.3. The test tube was very long, because it was the only available option that could fit the diameter of the brains. First, a base of cotton was laid at the bottom of the tube, in the conical edge. Then the brain was pushed down gently, and more cotton was placed behind the brain for stabilization. Eventually, other cotton was added above the brain until the end of the tube was reached. The cotton and the brain were immersed in Fomblin. Fomblin is a a chemically inert perfluoropolyether (PFPE) fluorocarbon used in MRI scans because it is a proton-free liquid, containing no hydrogen atoms. As a result, it does not produce any MRI signal and does not need background suppression [28, 66]. It is important to avoid the presence of air bubbles in the test tube, because they can affect the quality of the image. They can be eliminated with subtle movements of the brain or cotton in the tube.

When placing the brain in the test tube, the tissue that was fixated undergoes some mechanical movements that can alter its properties. It is generally recommended to allow the sample some time to stabilize, for instance by performing a long non-diffusion-weighted structural scan before diffusion imaging. Due to time constraints, this was not always possible and was sometimes replaced with a shorter scan.

4.2. Experimental setup

In this section, the setup of the experiments is presented.

All the acquisitions are performed using a Bruker preclinical scanner BioSpec 70/20 USR. This scanner has a main field strength of 7 Tesla, a bore diameter of 20 cm,

maximum gradient strength of 660 mT/m and slew rate of 4570 T/m/s. It possesses an actively shielded gradient system and built-in shim coils to ensure high magnetic field uniformity. It is coupled with a Paravision™ 360, which is an intuitive platform designed for multidimensional MRI data acquisition, visualization, reconstruction, and analysis [8].

First of all, the RF coil was selected. The choice was between a combined transmitter-receiver coil and two separate ones. The first option was chosen for a more homogeneous SNR, as it is a volume coil (Bruker Biospin, RF RES 600 1H 059/035 QSN TR). The separate receiver is usually used to have a high SNR in a focal region. This was excluded because it requires very precise positioning of the coil and can cause the SNR to drop in unwanted regions. The coil was placed inside the scanner, then the sample was laid on the MR bed selected and slid inside the bore. It was made sure that the center of the sample was located in the correspondence of the center of the bore, longitudinally, in this case 63 cm inside from the reference laser. The test tube containing the sample was placed on a custom-made LEGO™ setup, secured to the MR bed using adhesive putty (e.g., UHU Patafix) and tape (see Fig. 4.2). A slight slope was created to move any residual air bubble to the top of the test tube, far away from the sample. This was obtained by placing two LEGO™ bricks in correspondence with the top of the test tube and one at the bottom. The test tube was oriented with the brain upside down to ensure that any residual air bubbles would rise to the top, away from the region of interest.

Mechanical stability was ensured by firmly tightening the screws of the sample holder and verifying that the sample was immobilized by the tape and adhesive putty, to minimize movement and prevent misalignments during acquisition. Nonetheless, minor shifts may still occur due to thermal effects, such as slight heating during scanning.

Once the sample was inside the scanner, frequency wobbling could be performed. This involves sweeping the radiofrequency signal across a range of frequencies around the expected Larmor frequency, to measure the coil's absorption spectrum and identify the resonance point. This allows manual tuning and matching of the RF coil to ensure it is optimally set to the Larmor frequency of the nuclei being imaged. After that, the resonance frequency of the coil was adjusted, together with the RF pulse power and the receiver gain. The B_0 field was then estimated, and high-order shimming was applied to reduce homogeneities. It is important to perform this step to correct for field discontinuities, such as those caused by an air bubble. Subsequently, a quick localizer was acquired to verify whether the sample was in the correct position. Ideally, the sample should be in the region where the field is more intense to maximize the SNR. The position can be adjusted with some subtle movements and checking with more localizers. Once the setup and placement of the sample were satisfactory, a RF metal shield was placed on the open end of the scanner to improve the shielding as seen in Fig. 4.1. After that, the actual scan could begin.

4.3. Experimental protocol

In this section, the MRI scans acquired are described in detail.

Figure 4.1: Metal cage acting as RF shield.

Figure 4.2: Side view of the sample mounted on the MRI bed. Note the slight slope to avoid air bubbles in the area of interest.

Figure 4.3: Rat brain in the test tube. The dark line marks the area under analysis.

The subjects listed in Table 4.1 were scanned using the following acquisition protocol:

- a T_2-weighted structural scan (RARE),
- trial scans, with a few slices and without diffusion weighting, to check the SNR.
- diffusion-weighted images. Different diffusion-weighted sequences have been implemented, and they will be described in detail in the next subsections.

For all diffusion sequences tested, the voxel size was fixed at $0.2 \times 0.2 \times 0.75$ mm^3, while the image dimensions were adjusted according to the brain size. The anisotropic voxel dimensions were chosen to enhance the signal-to-noise ratio, accepting the trade-off of increased partial volume effects.

4.3.1. PGSE sequence

This section outlines the experimental design of a PGSE sequence.

This sequence was acquired with low b-value (3500 s/mm^2) for DTI fitting and with

higher diffusion weightings (15000 and 18000 s/mm^2) for the estimation of parallel and perpendicular diffusivities as explained in Sec. 3.3.1. In these acquisitions, a little variation on the PGSE sequence is applied, following the recommendation of [64]. Rather than using the Spin Echo (SE) sequence as a base of the dMRI scan, which would be time-consuming as a single k-space line would be read at each RF pulse, a multi-shot Echo-planar imaging (EPI) was chosen. In a classic EPI acquisition, the entire k-space is acquired in one shot. While this allows very fast imaging, it comes at the cost of reduced SNR compared to SE techniques. As a trade-off, multishot EPI acquires k-space in N shots, extending the acquisition time and hence the SNR. Additionally, the signal-to-noise ratio can be further enhanced by increasing the number of averages, which helps to reduce noise and minimize potential artifacts. SE is, in general, more robust to motion, but dealing with ex vivo samples, this does not represent a major issue. The design choices were $N \in 10, 11, 12$ shots or k-space segments and 16 averages. The SNR increases with the square root of the acquisitions, hence by a factor of $\sqrt{16} = 4$. When the number of shots equals the number of lines of the image, then a SE is obtained. N varies between 10,11,12 because some images required a higher N to avoid ghosting artifacts. With these parameters, the scanning time of multishot EPI with 16 averages equals that of SE with two averages, resulting $\sqrt{\frac{16}{2}} \approx 2.83$ increase in SNR.

The choice of the number of directions was based on [3]. They show that 30 directions are enough to robustly characterize the spherical average of the signal measured in thin cylinders. Therefore, 32 directions were chosen. It is important to note that the more the number of directions, the longer the scanning time. A uniform direction distribution was obtained using the electrostatic repulsion algorithm [10, 34]. The resulting b-vector distribution was loaded into the scanner and applied, as illustrated in Fig. 4.4.

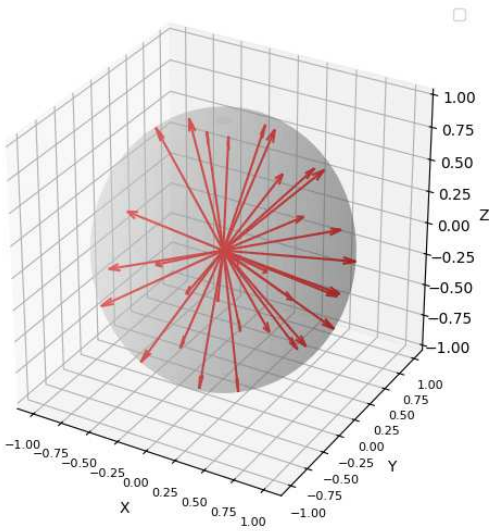

Figure 4.4: Distribution of b-vectors on the unit sphere.

The next parameters to be set were the gradient duration δ, the separation Δ, and the b-value. The gradient amplitude follows inverting Eq. 3.46.

δ and Δ play a fundamental role in the diameters that can be probed. If the gradient pulse duration δ is too long, the center-of-mass effect occurs (see Eqs. 3.5 and 3.6), causing the restricted compartment to behave like a dot or stick [46]. This results in the loss of measurable diameter and, consequently, no perpendicular diffusivity to probe. Therefore, δ must be set as short as possible to mitigate this phenomenon. At the same time, the molecules need sufficient time to interact with restrictions in their environment, such as axonal walls.
To estimate the distance spanned by molecules during the pulse timings, the root mean square displacement of free water in three dimensions was calculated using Einstein's theory of Brownian motion [17] as

$$\langle r^2 \rangle = 6Dt, \tag{4.1}$$

where D is the diffusion coefficient, approximated as $0.5 \times 10^{-3}\, mm^2/s$ according to [56], considering ex vivo white matter tissue at approximately $20°C$. Here, t is the effective diffusion time, given by

$$t = \tau = \Delta - \frac{\delta}{3}. \tag{4.2}$$

With this reasoning, for $b = 3500\,\mathrm{s/mm^2}$, it it was possible to set $\delta = 7\,\mathrm{ms}$ and $\Delta = 15\,\mathrm{ms}$, resulting in a root mean square displacement of:

$$\sqrt{\langle r^2 \rangle} = \sqrt{6Dt} = \sqrt{6 \cdot (0.5 \cdot 10^{-9}\,\mathrm{m^2/s}) \cdot \left(15 - \frac{7}{3}\right) \cdot 10^{-3}\,\mathrm{s}} \approx 6.2\,\mu\mathrm{m}. \tag{4.3}$$

These timings required a gradient power of 43%.

The average axonal diameter in the rat brain is approximately $1\,\mu$m in the genu and splenium, and $3\,\mu$m in the body of the corpus callosum [5]. This diffusion distance is thus appropriate to ensure that water molecules can reach and probe axonal boundaries.

For $b = 15000\,\mathrm{s/mm^2}$ and $b = 18000\,\mathrm{s/mm^2}$, δ was set to 10 ms and Δ to 16 ms. The gradient power was 62.0% and 67.9% for these b-values, respectively. Longer pulses are needed to avoid exceeding the gradient power limit. However, the RMS displacement remained essentially unchanged due to the square root relationship:

$$\sqrt{\langle r^2 \rangle} = \sqrt{6Dt} = \sqrt{6 \cdot (0.5 \cdot 10^{-9}\,\mathrm{m^2/s}) \cdot \left(16 - \frac{10}{3}\right) \cdot 10^{-3}\,\mathrm{s}} \approx 6.2\,\mu\mathrm{m}. \tag{4.4}$$

The repetition time TR was set to 2500 ms.

4.3.2. PGSE built as a free gradient waveform

This section describes the construction of a PGSE sequence as a custom implementation.

The Paravision™ 360 system available at the Danish Research Centre for Magnetic Resonance (DRCMR) [15] includes a user interface that enables the design of custom gradient waveforms beyond the conventional PGSE scheme. This interface was employed to create the TDE sequence (see Sec. 3.3.1). To better understand the working principles of the user-defined free waveform tool, a standard PGSE sequence was first implemented. This served as a benchmark, with the goal of reproducing the image obtained using the default diffusion sequence in normal mode with a diffusion weighting $b = 3500 s/mm^2$.

To create a free waveform, a gradient file must be written. An example gradient file was used as a template. The system requires two separate gradient files: one for the waveform before the 180° RF pulse, and one for the waveform after. Key parameters that need to be specified by the user in the file include the duration of the gradient (intended as the total duration of any waveform applied along the dimensions x, y, z), the amplitude of the pulses, and the number of sampling points. The latter depends on the gradient duration and resolution. In this case, the same gradient time resolution as the reference example —24 μ s— was adopted. This resolution is well within the system's capabilities, which support an internal timing resolution of 8 μs, as reported by Matthew Budde in the waveform design guide [9]. The gradient time resolution is calculated by dividing the total duration by the number of sampling points. The duration was manually set to the desired value ($\delta = 7$ms) and the number of points was adjusted to maintain the same resolution. The amplitude of the gradients can be set to a maximum of 1. For simplicity and interpretability, it was fixed at 1, and the actual physical amplitude was controlled using the gradient scaling input in the ParaVision™ 360 interface. The same gradient power percentage used in the standard PGSE sequence (43%) was adopted, achieving a b-value of 3500 s/mm^2 corresponding to a gradient amplitude g = 286 mT/m. The echo time was also matched to the standard sequence, set at 30 ms.

The gradients require ramp-up and ramp-down periods. These transitions were defined using the system's maximum slew rate, which is 4570 $mT/m/ms$, to ensure the fastest switching possible within system limits.

Given the maximum slew rate of the scanner and the maximum gradient amplitude used in the scan, the gradient ramp time can be calculated as:

$$\text{Ramp time} = \frac{g_{\max}}{\text{Slew rate}} \tag{4.5}$$

By dividing the ramp time by the system's sampling frequency, one finds the number of samples used in this ramp time. When multiple gradient strengths are applied, the one used to calculate the slew rate must be the maximum one.

To match the imaging conditions of the standard PGSE sequence, a multi-shot EPI readout was employed, as it was the acquisition method used in that protocol.

Interestingly, it was observed that using the free gradient waveform software requires multi-shot EPI to achieve a reduced echo time. In single-shot EPI, the TE is fixed at the center of the readout train. The interval between the end of the diffusion gradient and the TE is mirrored before the 180° pulse—i.e, between the initial 90° pulse and the onset of the first diffusion gradient—resulting in a prolonged TE and significant signal attenuation. By increasing the number of EPI segments, this pre-diffusion delay was reduced, allowing for a shorter TE comparable to that of the non-custom sequence. An example of the problem can be seen in Figure 4.5.

A graphical simulation was used to visualize and check the waveform setup. For example, the time required for each read-out line was calculated, and the number of segments needed to decrease TE was derived, given the image dimensions.

(a) PGSE obtained from the free gradient waveform interface with single-shot EPI readout.

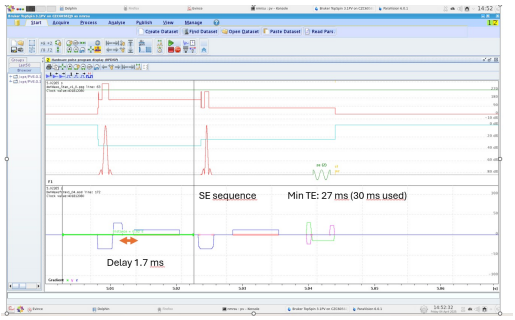

(b) PGSE obtained from the free gradient waveform interface with single-line SE readout.

Figure 4.5: Simulation interface of the sequence created with the gradient waveform program. On the left, one can see the delay between the 90° pulse and the onset of the first gradient, due to the single-shot EPI read-out. Instead, on the right, a Spin Echo sequence is used. The delay is minimum because of the shorter TE.

All acquisition parameters were carefully matched between the standard and custom sequences. In particular, double sampling was enabled in the custom sequence to match the effective bandwidth of the standard one. Double sampling means that each k-space line is sampled twice (once in each direction). The data from the two directions are reconstructed as separate magnitude images and subsequently summed, effectively removing Nyquist ghosts caused by mismatches between odd and even echoes. Without double sampling, the effective bandwidth obtained with the custom (free gradient) waveform was approximately half that of the standard sequence.

The final imaging bandwidths were 99.431 kHz for the standard sequence and 99.734 kHz for the custom sequence. This slight discrepancy is attributed to a minor difference in image size: 70×77 pixels in the standard sequence versus 75×77 pixels in the custom sequence, where the first dimension is the read-out (RO) direction and the second the phase encoding (PE) one. Since imaging bandwidth in MRI is directly related to the field of view (FOV) along the frequency encoding direction (RO), a change in image matrix size can result in a small variation in bandwidth.

This relationship is given by:

$$\mathrm{BW} = \frac{\gamma}{2\pi} \cdot g_{ro} \cdot FOV_{ro} = \frac{1}{\Delta t} \tag{4.6}$$

where g_{ro} is the readout gradient amplitude, and FOV_{ro} is the field of view in the readout direction, and Δt is the time between successive readout samples. This equation shows that small changes in FOV, when other parameters are fixed, can produce measurable differences in bandwidth [21]. A higher bandwidth increases the noise level due to the broader frequency range, resulting in lower SNR. However, it also allows for a larger minimum FOV, a shorter minimum TE, reduced echo spacing (which helps minimize distortions and blurring), and fewer artifacts overall [23]. Ideally, one of the two scans would have been repeated to exactly match the FOVs. However, given that the results were already satisfactory and the difference was minor, this small mismatch was accepted and accounted for in the interpretation of the resulting images.

4.3.3. Triple Diffusion Encoding - TDE

This section outlines the design of the triple diffusion encoding. The protocol was developed for a sample rat and subsequently extended to the remaining subjects. Therefore, the results are referred to the control case RA.BML.3841 (see Table 4.1).

The parameter design was inspired by the work of [61] presented in Section 3.3.1. However, since their data were acquired in vivo, adaptations were necessary to account for the lower diffusivity in ex vivo fixed tissue at room temperature, which is usually reduced by a factor of 2-5 (see Sec.4.1). Consequently, the axial and radial b-values were adjusted accordingly. To determine appropriate b-values, several preliminary experiments were conducted. The first step was to verify the range of b-values over which the approximation in Equation 3.73 remains valid. For this reason, the PGSE data with b = 3500 s/mm^2 was used to fit a DTI model, enabling estimation of DTI's axial, radial, and mean diffusivity values and evaluation of tissue integrity. This ensured that fixation had not significantly degraded contrast between white and gray matter. The DTI fitting revealed that diffusivity values were consistent with ex vivo brain tissue.

To ensure the validity of the spherical mean signal approximation of Eq. 3.73, the following condition must be satisfied [31]:

$$(b_{\parallel} - b_{\perp})(D_{\parallel} - D_{\perp}) > 3.4. \tag{4.7}$$

Using the average axial and radial diffusivity values estimated from the DTI fitting of white and gray matter[1]:

$$D_{\parallel} - D_{\perp} \approx (0.4 - 0.2) \times 10^{-9}\,\mathrm{m}^2/\mathrm{s} = 0.2 \times 10^{-9}\,\mathrm{m}^2/\mathrm{s} = 2 \times 10^{-4}\,\mathrm{mm}^2/\mathrm{s}. \tag{4.8}$$

[1]Note that it is a conservative approach as the perpendicular diffusivity found with DTI is higher than literature values [77].It could be caused by partial volume effects.

This implies:

$$b_{\parallel} - b_{\perp} > \frac{3.4}{2 \times 10^{-4}\, mm^2/s} = 17000 s/mm^2. \tag{4.9}$$

To satisfy this requirement, b-values of 18000 s/mm^2 (axial) and 1000 s/mm^2 (radial) were selected. Comparing with [61], they used axial and radial b-values of 4000 s/mm^2 and 307 s/mm^2, respectively. The corresponding b-value ratio in their study was $4000/307 \approx 12.02$, whereas in the present work the ratio is $18000/1000 = 18$. This increased ratio arises from the need to reduce the echo time and minimize signal attenuation, which is especially important in ex vivo acquisitions with long sequences. For this reason, the radial b-value was kept lower than what would be expected if directly scaling the proportion used by [61]. Meanwhile, a high axial b-value remains essential to suppress the extracellular signal and enhance sensitivity to restricted diffusion components.

With the b-values defined, the gradient durations δ and diffusion times Δ were selected. These parameters are constrained by the following:

- $\delta < \Delta$;
- Scanner gradient limit of 660 mT/m;
- Power usage should remain below 80% of maximum.

To minimize TE and optimize signal quality, a gradient amplitude of $g = 500$ mT/m was used, corresponding to 75.2% of the system's maximum capacity. This setting balances strong diffusion weighting with manageable echo times.

The same gradient amplitude g was used for both radial and axial directions to simplify implementation on the scanner and facilitate interpretation in simulations. The different $b_{\parallel}$ and $b_{\perp}$ were obtained by tuning the parameters δ and Δ. To guide parameter selection, Einstein's equation for the root mean square displacement in free diffusion (Eq. 4.1) was used.

In the study by [61], the average axial diffusivity (D_a) measured in vivo was reported as 2.24×10^{-3} mm^2/s. Accounting for the typical 2–5 fold reduction in diffusivity due to fixation and room temperature in ex vivo conditions, a conservative estimate of 0.5×10^{-3} mm^2/s was used in this work, corresponding to the worst-case reduction factor of 5. This assumption is also supported by the findings of [56]. Accordingly, the root mean square displacement (RMSD) calculated under this assumption represents the lower bound; higher diffusivity values would yield proportionally larger displacements.

Various combinations of δ and Δ were tested to produce an RMSD comparable to typical axon diameters, especially for the perpendicular b-value, which corresponds to diffusion exactly aligned perpendicular to the axon. As discussed previously, axon diameters in the rat corpus callosum typically range from 1 to 3 μm depending on the region [5]. Therefore, the diffusion time was selected to produce an RMSD slightly above 3 μm to ensure that the axon diameter was effectively probed. It is important to note that an RMSD exceeding the average axon diameter is not a concern in this context. The radial diffusion gradients serve primarily to filter

signal contributions from specific directions. The combined action of the three diffusion gradient directions effectively probes prolate tensor geometries, enabling differentiation between intra- and extracellular compartments, and isolating axonal diffusivity contributions. After exploring different parameter sets that satisfied the target b-value, $\delta = 3$ ms and $\Delta = 7.2$ ms were selected, resulting in an RMSD of approximately 4.24 μm and a radial b-value close to $1000\,\mathrm{s/mm^2}$:

$$b_\perp = \gamma^2 \left(500 \times 10^{-3}\,\mathrm{T/m}\right)^2 \left(3 \times 10^{-3}\,\mathrm{s}\right)^2 \left(7.2 \times 10^{-3}\,\mathrm{s} - \frac{3 \times 10^{-3}\,\mathrm{s}}{3}\right) \approx 1000\,\mathrm{s/mm^2} \tag{4.10}$$

$$\mathrm{RMSD} = \sqrt{6 \times 0.5 \times 10^{-9}\,\mathrm{m^2/s} \times \left(7.2 \times 10^{-3}\,\mathrm{s} - \frac{3 \times 10^{-3}\,\mathrm{s}}{3}\right)} \approx 4.3\,\mu\mathrm{m} \tag{4.11}$$

For the axial direction, the choice of diffusion time is less problematic. One key consideration is whether to model axons as sticks, which assumes long pulse durations that lead to the center-of-mass effect. In [61], a long $\Delta = 37\,\mathrm{ms}$ and $\delta = 18.55\,\mathrm{ms}$ were used due to clinical scanner limitations, but this would result in an excessively long echo time in the ex vivo setting.
Hence, shorter δ and Δ were tested. Following the same reasoning as for the perpendicular b-value, given a desired $b_\parallel = 18000\,\mathrm{s/mm^2}$ and $g = 500\,\mathrm{mT/m}$, a combination of $\delta = 8.6\,\mathrm{ms}$ and $\Delta = 16\,\mathrm{ms}$ was chosen. Shorter δ values were also tried, but the resulting Δ became too long, increasing the diffusion time and hence the echo time, which must be minimized to improve SNR.

$$b_\parallel = \gamma^2 \left(500 \times 10^{-3}\,\mathrm{T/m}\right)^2 \left(8.6 \times 10^{-3}\,\mathrm{s}\right)^2 \left(16 \times 10^{-3}\,\mathrm{s} - \frac{8.6 \times 10^{-3}\,\mathrm{s}}{3}\right) \approx 18000\,\mathrm{s/mm^2} \tag{4.12}$$

$$\mathrm{RMSD} = \sqrt{6 \times 0.5 \times 10^{-9}\,\mathrm{m^2/s} \times \left(16 \times 10^{-3}\,\mathrm{s} - \frac{8.6 \times 10^{-3}\,\mathrm{s}}{3}\right)} \approx 6.3\,\mu\mathrm{m} \tag{4.13}$$

With these δ and Δ, the actual b-values obtained were approximately 17444 s/mm^2 and 1000 s/mm^2 for the parallel and perpendicular directions, respectively. Considering possible diffusivity fluctuations, these values were deemed acceptable.

To reduce TE the acquisition bandwidth was increased from 100 kHz to 150 kHz. Although this adjustment could introduce Nyquist ghosting artifacts, enabling double sampling avoided this issue (see Sec. 4.3.1).

With these settings, TE was set to the minimum possible for each subject, slightly

above 50 ms. Precise values can be seen in Table 4.2.

SubjID	TE [ms]
RA 87, RA.BML.3841	52.13
RA89, RA76	52.58
RA 71, RA86	51.26
RA114	53.06

Table 4.2: Echo times used for each subject in the TDE acquisition.

Two repetition times (TRs) were tested, 2500 ms and 3500 ms, to compare their effect on SNR. Increasing TR improves SNR but also increases scan time. A scan time of 2500 ms (4 hours) was chosen as a feasible compromise; 3500 ms TR would take 5 hours 36 minutes, and 5000 ms would take 8 hours.

To further increase SNR, 16 averages were acquired. The number of EPI segments, N, was set to 10,11 or 12 depending on the subject.

Figure 4.6 shows the gradient waveform built using the parameters described earlier. As shown, the spacing between axial and radial gradients was minimized to reduce the echo time. The gradient amplitude was modulated dynamically once the sequence was loaded on the scanner.

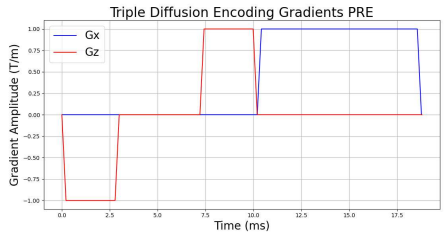

(a) Gradients along x and z directions, before application of the 180° pulse.

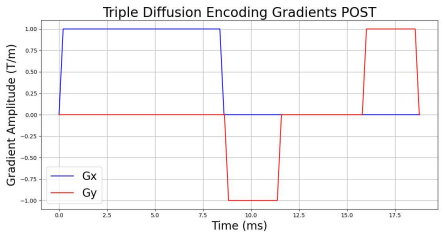

(b) Gradients along x and y directions, after application of the 180° pulse.

Figure 4.6: Pre- and post- 180° pulse TDE gradient waveforms.

Figure 4.7 shows the TDE as displayed in the simulator available in the Paravision™ 360 interface. For visualization purposes, only a single average and a single shot are shown, as the full sequence becomes too complex for the simulator to process. Note that the gradient directions in the figure do not correspond to the actual physical directions used during acquisition.

This acquisition was coupled with the two SDEs at b-values of 18000 s/mm^2 and 15000 s/mm^2, to derive the axial and radial diffusivities as exposed in Sec. 3.3.1.

4.3.4. Sequence for Spherical variance T_2 fitting

This section outlines the technical decisions made in designing the diffusion protocol used to estimate axonal T_2 as described in Section 3.4.

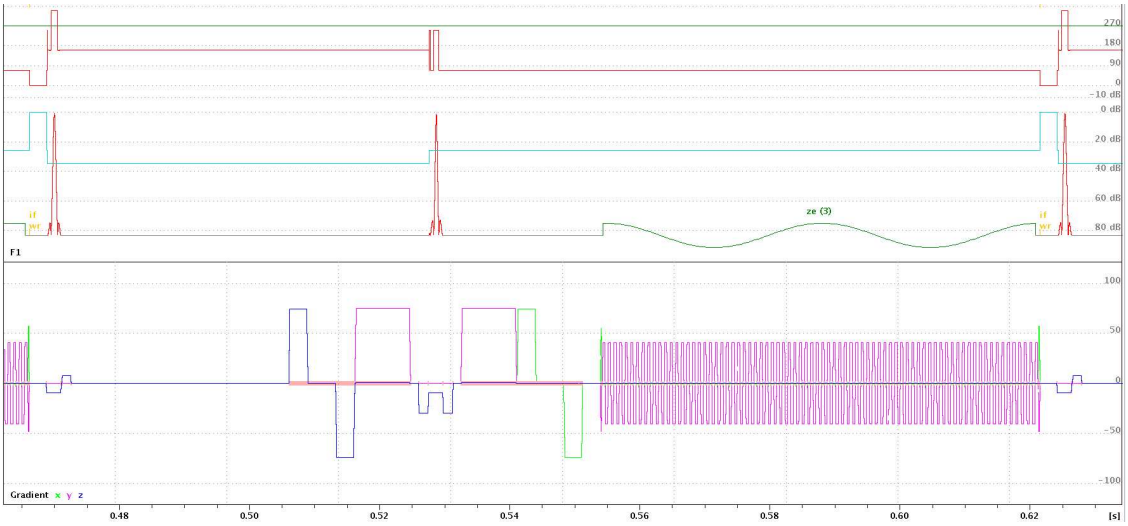

Figure 4.7: Triple Diffusion Sequence as shown in the simulation of the Paravision™360.

Three diffusion-weighted images with three different echo times were acquired using the control subject RA87. The acquisition was performed using a PGSE sequence. The TEs were selected to be equally spaced: 35 ms, 50 ms, and 65 ms. The choice of b-value was guided by the level of noise observed in the spherical variance estimate. An initial trial using a high b-value of 23 000 s/mm^2 resulted in T_2 maps that were excessively noisy. Subsequently, lower b-values of 18000 s/mm^2 and 15000 s/mm^2 were tested, with an increased number of averages. Only 4 were used in the beginning and 9 in the following acquisitions, with an increase of $\sqrt{9/4} = 1.5$ in SNR. The decrease in b-value and increase in averages improved the SNR and the quality of the T_2 map. The final analysis was performed on the b-value 15000 s/mm^2. The number of segments was fixed to 10, δ was set to 10 ms and Δ to 16 ms. Gradient power was 412.04 mT/m, using 61.97% of the power. The repetition time TR was 2500 ms.

4.4. Data processing

This section describes the adopted data preprocessing method.

The acquired data were processed using a pipeline inspired by the work of the MaP-science group [65]. Since their code was originally developed for standard acquisition sequences, it had to be adapted to support the custom free waveform sequence. This was necessary because the `methods` file produced by the scanner had a different structure. The first step of the pipeline consisted of the BIDsification of the data. BIDS, which stands for *Brain Imaging Data Structure*, is a standardized format for organizing and describing neuroimaging and behavioral datasets. This structure greatly simplifies data sharing and ensures compatibility across research groups. An example of the conversion from DICOM to BIDS format is shown in Figure 4.8. As illustrated, the data are separated into anatomical and diffusion-weighted folders. Each contains a `.json` file with information about the sequence, and a `.nii` file with image data. Anatomical images are three-dimensional, with dimensions (x, y, z), while diffusion-weighted images are four-dimensional (x, y, z, t),

where t is the number of diffusion directions plus $b = 0$ volumes. The b_0 images are acquired alongside diffusion-weighted images and are used for signal normalization. The diffusion folder also includes `.bvec` and `.bval` files that define gradient directions and corresponding b-values.

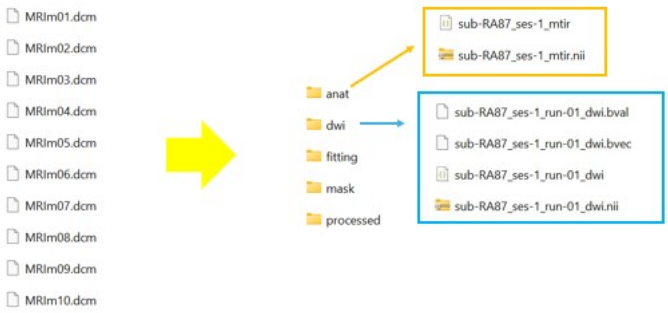

Figure 4.8: Reorganization of data in BIDS format. On the left there are the images in DICOM format, on the right the subsequent BIDS organization.

The second step of the preprocessing was the denoising, for which two methods were tested. The first employed the Marchenko-Pastur Principal Component Analysis (MP-PCA) method [13], implemented via the `dwidenoise` command in MRtrix3 [74]. The second method aimed to remove the Rician noise bias.

The MP-PCA method uses the Marchenko-Pastur (MP) distribution from random matrix theory to determine the threshold between the signal and noise components. By analyzing the eigenvalue spectrum of local data patches, the algorithm can separate meaningful signal variations from random noise, excluding the components with eigenvalues below the MP threshold. This approach assumes the noise to be additive white Gaussian noise (AWGN), which means that it is added to the true signal, is uncorrelated across voxels and volumes (whiteness), and follows a normal distribution with zero mean $\eta \sim \mathcal{N}(0, \sigma^2)$. The noise is subtracted from the image, and the result is an increase in SNR. However, the noise of magnitude images (commonly used in dMRI) does not follow a Gaussian distribution, but it is usually Rician. Only the noise of real or imaginary images is Gaussian. If the SNR is high enough, the Rician distribution tends to the Gaussian one [24]

The second denoising method, inspired by [41], consists of four steps. First, the noise variance is estimated. A variance stabilization transformation (VST) is then applied to the Rician data to normalize the standard deviation, transforming the data to approximate Gaussian noise with a stabilized standard deviation near 1. This transformation enables the use of conventional denoising techniques. In this case, denoising is performed by applying the optimal shrinkage of singular values from local 3D cubic patches, as described by Gavish and Donoho [20], which minimizes mean squared error (MSE). Unlike thresholding methods, which define a cutoff and discard singular values below that threshold (assuming they are noise), optimal shrinkage retains all singular values while reducing the influence of noise through a smooth attenuation function. This allows for more effective denoising while pre-

serving underlying signal structure. Eventually, an Exact Unbiased Inverse Variance Stabilizing Transformation (EUIVST) maps the denoised data back into the original space, removing the bias introduced by the Rician noise [19]. The overall denoising technique used was that adapted [58].

Most of the data acquired in this project falls within the high b-value regime, where the signal-to-noise ratio is low and the noise deviates significantly from a Gaussian distribution. For this reason, the second denoising method was chosen, as it is expected to offer greater robustness under these conditions.

After denoising, Gibbs ringing artifacts were removed using the `dwidegibbs` command from MRtrix3 [74]. These artifacts arise from the truncation of the Fourier series used to reconstruct MR images from k-space data. Because MRI samples only a finite portion of k-space, high-frequency components—necessary to accurately represent sharp intensity transitions—are missing. When signal intensity changes gradually across space, only a few low-frequency components are needed, and truncation has minimal impact. In contrast, sharp boundaries require higher frequency components to be accurately represented. Without them, the truncated Fourier approximation introduces oscillatory artifacts near these edges, characterized by alternating over- and undershoots. Since Gibbs artifacts are a fundamental consequence of the Fourier representation, they can appear in both phase-encoding and frequency-encoding directions. However, they are typically more pronounced along the phase-encoding axis, where fewer k-space lines are acquired.
The `mrdegibbs` algorithm was therefore applied along both the phase- and frequency-encoding axes. While these artifacts predominantly affect $b = 0$ images, they can also subtly contaminate diffusion-weighted images. Since the processing did not remove meaningful anatomical features, Gibbs removal was applied to both image types [59].

As a third step, the dataset was split into two parts: the full diffusion dataset (including b_0 images) and a separate average b_0 image, computed across the b_0 volumes within each scan. This average b_0 image was used in steps 4 and 5.

The alignment step provided in the reference pipeline was skipped because all the images were acquired in the same modality and ex vivo, so motion was negligible, aside from minor mechanical shifts (e.g., due to softening of the mounting material, such as Patafix). Visual inspection generally confirmed the absence of motion artifacts, justifying the exclusion of this procedure. In cases where mechanical motion was detected, the affected images were excluded from the analysis.

In the fourth step, a brain mask was generated using Otsu thresholding [2], which segments foreground from background based on intensity variance. For datasets with multiple diffusion acquisitions, the mask was computed from the averaged b_0 of the first scan. This mask was used in later stages to limit computations and improve visualization of parameter maps.

The fifth step consisted of normalizing each diffusion image by the mean intensity of the corresponding b_0 image obtained from the splitting. Averaging multiple b_0 images enhances the signal-to-noise ratio by reinforcing the consistent underlying

[2]Implemented with the Python function `skimage.filters.threshold_otsu`.

signal across repeated acquisitions, while uncorrelated random noise tends to cancel out through averaging. This normalization must be performed after denoising, as artifacts such as Gibbs ringing could otherwise affect the result.

Finally, the powder-averaged (or spherical mean) signal was computed by averaging the diffusion-weighted signal across all directions at a given b-value, yielding a signal independent of the axon distribution (see Sec. 3.2.2).

The resulting images were then used as input for the subsequent modeling steps.

4.5. Data analysis and parameter inference

This section outlines how the acquired data were modeled and analyzed to extract the parameters of interest.

4.5.1. Diffusivity, μFA and Axonal Signal Fraction Estimation

This section describes how the parameters of interest were inferred.

The data acquired with TDE, along with the two SDE acquisitions at high b-values, were used to derive parallel and perpendicular diffusivities, as well as axonal signal fractions in rats with and without Alzheimer's disease, as detailed in Section 3.3.1.

Initially, the estimation of the diffusivities was attempted by inverting Eq. 3.74 and Eq. 3.78. This method involves taking the logarithm of signal ratios, which becomes unstable at high b-values due to low SNR, sometimes resulting in non-physiological negative values.

To address this, different optimization frameworks were evaluated: non-linear least squares fitting, differential evolution [70], and random forest regression. However, when applied directly to the signal ratios (Eq. 3.74 and Eq. 3.78), these methods failed to converge or yielded implausible parameter values. Therefore, the fitting procedure was reformulated to directly model the measured signals S_1, S_2, and S_{TDE} using Eq. 3.80 for SDE and Eq. 3.72 for TDE. Among the tested strategies, NLLS was chosen for its simplicity and computational efficiency. In this formulation, parameter inference relies on minimizing the sum of squared differences between the measured signals y_i and the corresponding model predictions $f(x_i;\boldsymbol{\theta})$. The parameter vector is defined as $\boldsymbol{\theta} = [C, D_{\parallel}, D_{\perp}]$ and the objective function is given by

$$\boldsymbol{\theta} = \min_{\boldsymbol{\theta}} \sum_{i=1}^{n} \left[y_i - f(x_i;\boldsymbol{\theta}) \right]^2 , \tag{4.14}$$

where $y_i \in \{\bar{S}_1, \bar{S}_2, \bar{S}_{\mathrm{TDE}}\}$ and $f(x_i;\boldsymbol{\theta})$ denotes the modeled signal corresponding to the respective diffusion encoding scheme (Eq. 3.80 for SDE and Eq. 3.72 for TDE).

Directly fitting the raw signals rather than their ratios preserves the additive Gaus-

sian noise structure, satisfying the assumptions of NLLS fitting. These hypotheses include independence of residuals, normal distribution with zero mean, and constant variance (homoskedasticity) [1]. In contrast, using ratios of noisy signals introduces non-Gaussian, non-additive, heteroskedastic noise, violating these assumptions and making estimation statistically unreliable.

Microscopic fractional anisotropy was subsequently computed from the estimated parameters using Eq. 3.50, with $\lambda_1 = D_{\parallel}$ and $\lambda_2 = \lambda_3 = D_{\perp}$.

4.5.2. Regions of interest

This section displays the Region of Interests (ROIs) used for the statistical analysis.

Three ROIs were segmented: one for white matter, located in the center of the corpus callosum, and two in gray matter, consisting of symmetric cortical regions in the motor and somatosensory areas [38]. Manual segmentation was performed on a set of 4 slices to increase the number of voxels over which to perform statistical analysis and hence improve robustness (the 4 slices contained the corpus callosum at its maximum thickness, in the central region of the brain). These ROIs were drawn on the axial diffusivity map for DTI, while on the radial one for TDE, as it was less noisy. A preliminary statistical test confirmed no significant difference between the left and right gray matter ROIs of each cortical region, as expected, allowing them to be treated as a single region for further analysis.

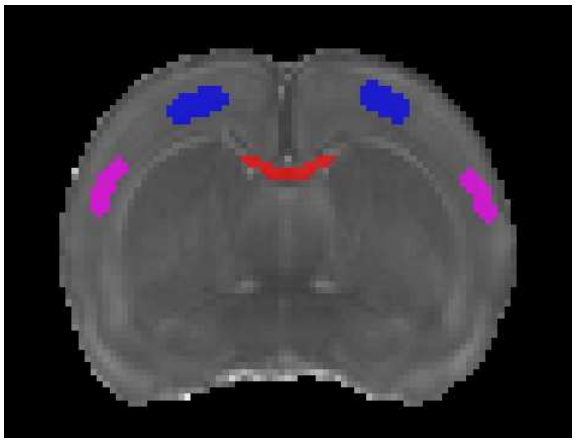

Figure 4.9: Example of ROIs drawn on a slice of RA.BML.3841. The red one belongs to the corpus callosum, while the blue ones to the motor cortex, and the purple ones to the somatosensory cortex.

4.5.3. Statistical analysis methods

This section presents the stastical analysis performed.

First, diffusivity estimates and microscopic fractional anisotropy obtained from TDE were statistically compared with those derived from DTI fitting of images acquired at $b = 3500$ s/mm^2, used as a reference for comparison. Importantly, axonal signal

fraction cannot be derived using a DTI approach, as it does not distinguish between different tissue compartments.

Normality was assessed for each dataset to guide the choice of statistical tests. Sample size plays a critical role in the interpretation of normality tests: when samples are small, tests often accept the null hypothesis that data follow a Gaussian distribution. In contrast, for large samples, even minor deviations from normality can lead to statistically significant rejection. In this study, although each group only had three brains, a large number of voxel-wise measurements were sampled per subject (approximately 300 for white matter and 800 for gray matter in motor cortex, and 700 for somatosensory cortex), resulting in effectively large sample sizes. To address this, both the Shapiro-Wilk test and the Kolmogorov-Smirnov (KS) test were employed. The KS test is generally less sensitive to sample size and tends to accept the null hypothesis unless deviations are substantial, especially when skewness and kurtosis are near zero. This makes it a useful complement to the Shapiro-Wilk test, which may over-reject normality in large datasets. These tests were followed by a histogram inspection, especially when the results disagreed [16]. A significant result (in this case $p < 0.05$) indicates a departure from normality, guiding the decision between parametric (independent samples t-test) and nonparametric (Mann–Whitney U test) methods [45]. The Mann-Whitney U test, also known as the Wilcoxon rank sum test, evaluates differences between two independent groups without assuming any specific distribution, while the t-test requires normally distributed data [43]. Normality was assumed only when both the Shapiro-Wilk and Kolmogorov-Smirnov tests failed to reject the null hypothesis ($p > 0.05$) for both groups, unless the histograms proved differently. In all other cases, nonparametric tests were used to ensure robustness against violations of normality assumptions.

The samples from the two methods were considered independent, as the ROIs differed between the TDE and DTI maps, because some subjects had scans acquired in different sessions.

The Mann–Whitney U test operates by ranking all observations from both groups combined and comparing the sum of ranks between groups. Because it relies on ranks rather than raw values, it is robust to outliers and deviations from normality. However, it can be less sensitive to subtle differences in central tendency or variance when the distributions have similar rank patterns but differ in shape. Moreover, while statistical tests can determine whether a significant difference exists between groups, they do not indicate the direction or magnitude of that difference. A simple comparison of sample means or medians offers a point estimate of central tendency, but this single value does not capture the variability of the estimate across repeated samples or clarify which group tends to have higher values.

To address these limitations, a complementary bootstrap resampling procedure was applied to estimate the sampling distribution of the difference in central tendency (mean if the data distribution is symmetric, median if it is skewed [60]). Specifically, 10 000 bootstrap samples were generated by resampling with replacement from each group, and the difference in central tendency was computed for each iteration. This procedure produced a robust, empirical distribution of the mean or median difference for each parameter and ROI. This approach offers several advantages: it makes no

assumptions about the underlying data distribution, is well suited to small sample sizes, and enables inference on the likely sign of the group difference. In particular, if the bootstrap distribution lies consistently above or below zero, it suggests a stable and directionally consistent effect between groups [67].

Subsequently, differences in diffusivities, microscopic anisotropy, and axonal signal fraction between control and 4-month-old Alzheimer's rats were tested for statistical significance across segmentation labels and methods. Axonal signal fraction was evaluated only in the TDE-based model. Since comparisons were made across subjects, independent samples tests were employed, with the choice between parametric and nonparametric methods determined by the results of normality testing. In addition to hypothesis testing, group differences were also evaluated using bootstrap distributions of the mean or median difference.

The 17-month-old subject was excluded from statistical analysis due to the limited sample size. Instead, a qualitative assessment was performed.

4.5.4. T_2 estimation

This section describes the procedure used to estimate axonal T_2.

Axonal T_2 was first derived using the spherical variance method (Eq. 3.84), by computing the variance directly from the signal (Eq. 3.83), following the preprocessing described in Section 4.4. To reduce the impact of noise, the variance was also estimated using the spherical harmonics expansion (Eq. 3.87), focusing on the $l = 2$ harmonic band, which is expected to contain most of the relevant signal content [44]. In both cases, the estimation used signals acquired at the shortest and longest echo times (35 ms and 65 ms, respectively). The resulting axonal T_2 values were then compared to those derived from the spherical mean method.

5 | Results

In this section, the results are exposed. First, some images of the experimental design are shown to motivate the choices made. Then, the results of the preprocessing are reported, followed by the parameter estimate maps.

5.1. PGSE implemented as a gradient waveform

This section presents a comparison between diffusion-weighted images acquired at $b = 3500$ s/mm^2 using the standard PGSE implementation and those acquired using the waveform-based software implementation. Both acquisitions included double sampling (see Sec. 4.3.2).

The SNRs were comparable: taking the mean of the signal in a homogeneous region of the corpus callosum and the standard deviation in the background, the resulting SNR was 116 for the waveform, and 120 for the normal setup. The respective b_0 images are displayed in Figure 5.1, while diffusion-weighted images from the first sampled direction are presented in Figure 5.2.

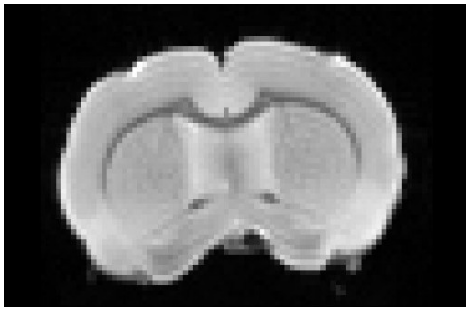

(a) First b_0 image acquired with the standard protocol.

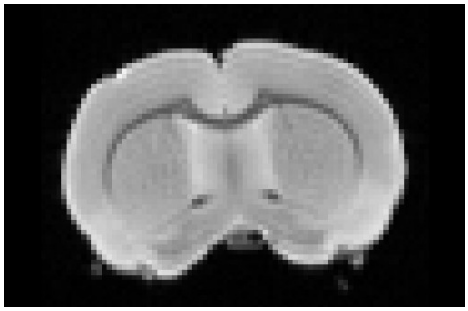

(b) First b_0 image acquired with the waveform-based protocol.

Figure 5.1: Comparison of raw b_0 images of subject RA87 acquired using the standard EPI implementation (left) and the gradient waveform software (right), both with double sampling.

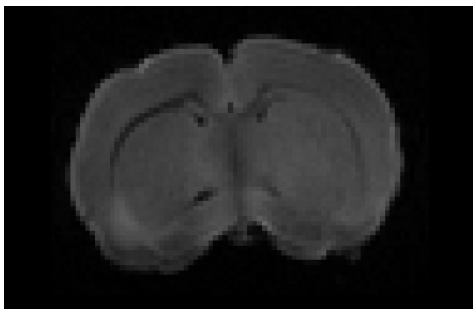

(a) First diffusion direction image acquired using the standard protocol.

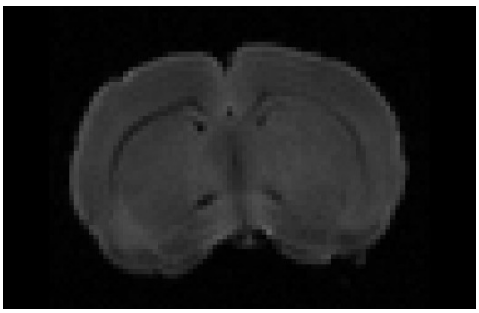

(b) First diffusion direction image acquired using the waveform-based protocol.

Figure 5.2: Comparison of DWIs (first direction) of subject RA87 acquired using the standard implementation (left) and the gradient waveform software (right).

5.2. Choice of the voxel size

This section presents the results of the single diffusion encoding acquisition at $b = 3500$ s/mm^2, comparing two different voxel sizes. The in-plane resolution was kept constant at 0.2×0.2 mm^2, while the slice thickness varied between 0.2 mm and 0.75 mm.

Figures 5.3 and 5.4 illustrate the effect of slice thickness on image quality. These data were acquired on subject RA.BML.3841. The SNR of the b_0 image was 80 for the 0.2 mm slice and 138 for the 0.75 mm slice. Despite the lower SNR, the thinner slice exhibits higher anatomical contrast between different structures.

The axial diffusivity maps derived from DTI fitting are shown in Figure 5.5. The thinner slice has higher contrast between anatomical structures, although the slices are not exactly matched due to the difference in thickness.

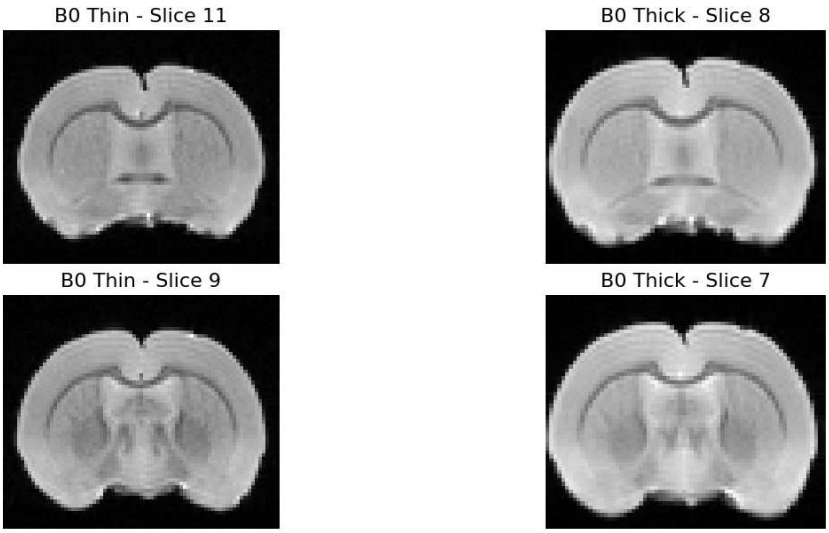

Figure 5.3: First b_0 image acquired with slice thickness 0.2 mm (left) and 0.75 mm (right).

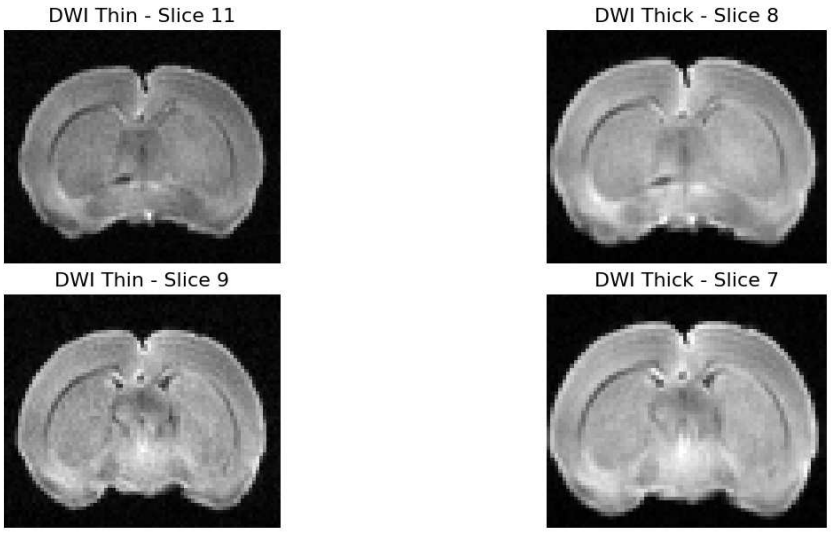

Figure 5.4: First diffusion direction of the DWI at $b = 3500$ s/mm^2 acquired with slice thickness 0.2 mm (left) and 0.75 mm (right).

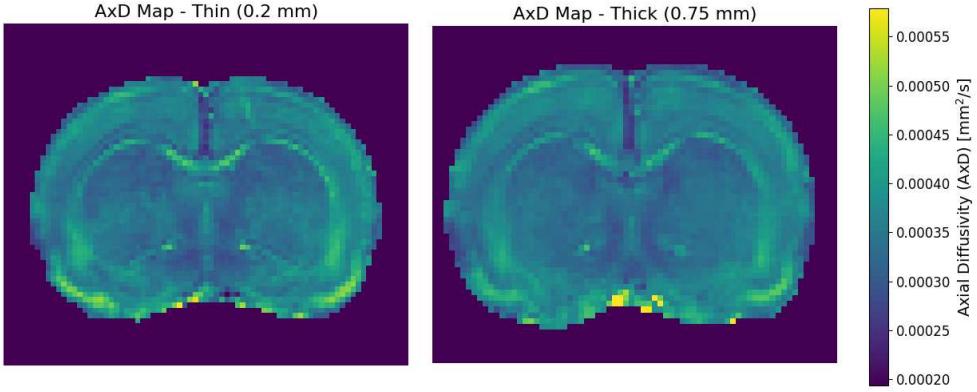

Figure 5.5: Axial diffusivity (first eigenvalue from DTI fitting) from DWI at $b = 3500$ s/mm^2, with slice thickness 0.2 mm (left) and 0.75 mm (right). Note that the contrast was increased for better visualization.

5.3. TDE sequence

This section showcases images relevant to the design steps of the TDE sequence, followed by the final image setup. The signal-to-noise ratio obtained with this sequence for each subject is reported in Table 5.1. The signal ROI was placed in the corpus callosum, while the noise ROI was taken from the background.

SubjID	RA87	RA89	RA.BML.3841	RA71	RA76	RA86	RA114	Mean
SNR	59	54	59	47	50	53	62.5	55

Table 5.1: SNR values for different subjects in the b_0 image of the TDE acquisition.

Figure 5.6 displays the finalized images acquired using the TDE sequence developed

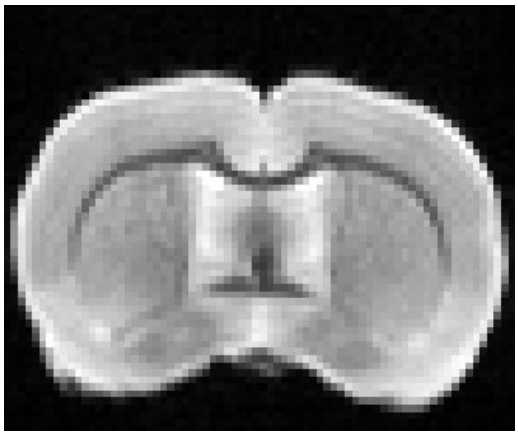

(a) First b_0 image acquired with the TDE scheme for subject RA87.

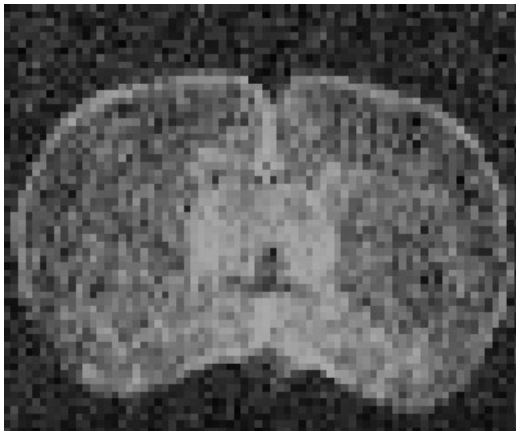

(b) First diffusion direction image acquired with TDE for subject RA87.

Figure 5.6: Display of b_0 and first diffusion direction images acquired with the TDE sequence, with increased contrast.

and described in Section 4.3.3. The SNR values in Table 5.1 provided sufficient tissue contrast in the diffusion-weighted images, despite the presence of some noise.

The images shown in Figure 5.6 are the result of preliminary experiments demonstrating increased SNR after applying double sampling, increasing averages, and using thicker slices. For example, Figure 5.7 compares b_0 acquisitions using the TDE sequence with slice thicknesses of 0.2 mm and 0.75 mm, while Figure 5.8 compares the corresponding diffusion-weighted images. Data acquired with thinner slices appear noisier and grainier, with a b_0 SNR around 24, resulting in diffusion images largely buried in noise. Conversely, thicker slices yield b_0 images with SNR around 50, producing still noisy diffusion-weighted signals, but the rat brain is clearly discernible. Note that they are not the exact same slice due to the different thickness.

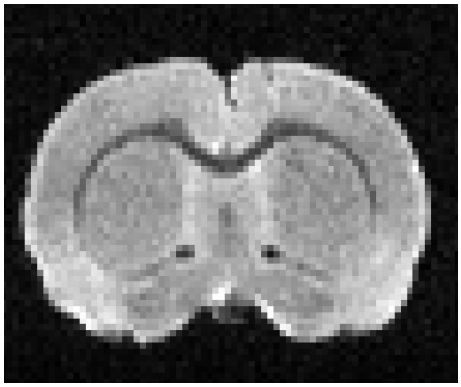

(a) First b_0 image acquired with TDE scheme for RA.BML.3841 with 0.2 mm slice thickness.

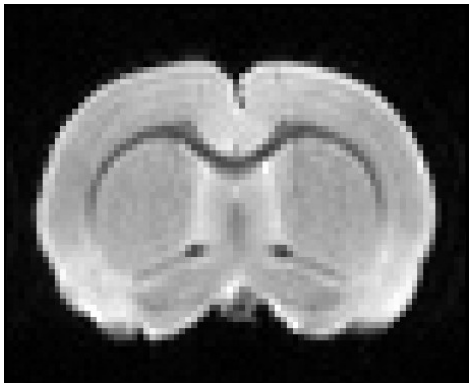

(b) First b_0 image acquired with TDE scheme for RA.BML.3841 with 0.75 mm slice thickness.

Figure 5.7: Comparison of TDE b_0 images acquired with two different slice thicknesses.

Figure 5.9 illustrates Nyquist ghosting artifacts observed after an increase in bandwidth, before double sampling.

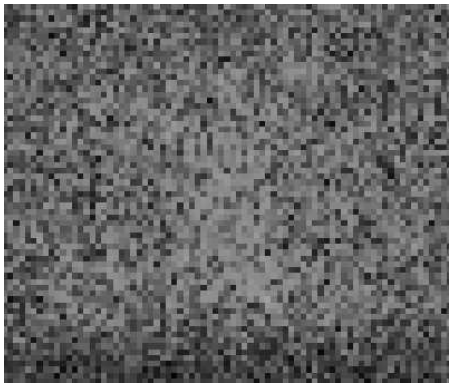

(a) First diffusion direction image acquired with TDE for RA.BML.3841 with slice thickness 0.2 mm.

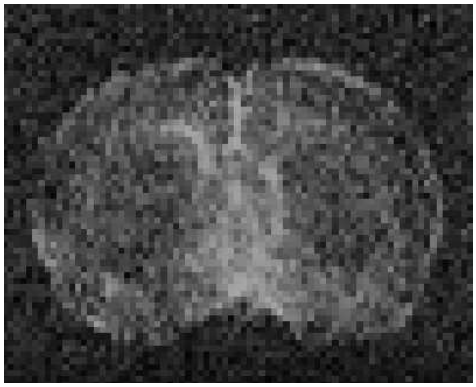

(b) First diffusion direction image acquired with TDE for RA.BML.3841 with slice thickness 0.75 mm.

Figure 5.8: Comparison of diffusion-weighted images acquired with TDE using two different slice thicknesses.

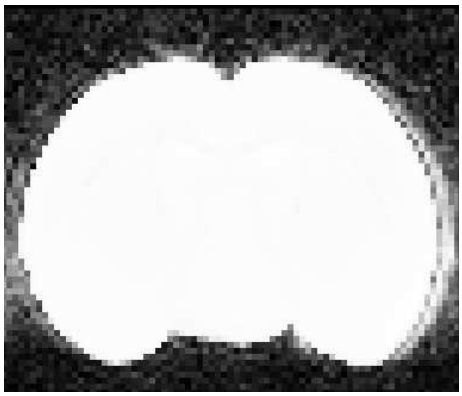

Figure 5.9: Nyquist ghost artifact observed before double sampling was implemented. Note that the contrast was increased.

Shim maps offer insight into intensity variations within the images. For instance, subjects RA86 and RA87 show differences in shim homogeneity affecting image quality. While RA87's shim map is in general uniform and gray (the desired condition), RA86 shows less uniformity with a dark spot likely caused by an air bubble.

(a) Shim map calculated for RA87.

(b) Shim map calculated for RA86.

Figure 5.10: Comparison of shim maps illustrating differences in homogeneity.

5.4. Data processing

This section reports the output of the preprocessing pipeline for a representative subject (RA.BML.3841), with results shown for the single diffusion encoding acquisition at $b = 18000$ s/mm^2.

5.4.1. Denoising

Figures 5.11 and 5.12 compare the raw data with the results after denoising using the MPPCA and Rician noise removal methods, for both the b_0 image and one diffusion-weighted direction. Rician denoising produces cleaner images, especially in the diffusion-weighted contrast, where the corpus callosum is clearer and less grainy than the corresponding MPPCA denoised image.

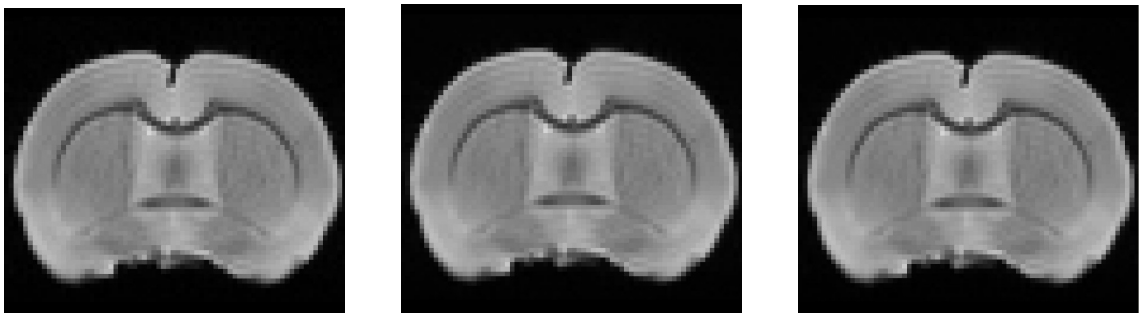

(a) Raw b_0 image.

(b) MPPCA denoised b_0 image.

(c) Rician denoised b_0 image.

Figure 5.11: Comparison of b_0 images: raw (let), MPPCA-denoised (middle), and Rician-denoised (right).

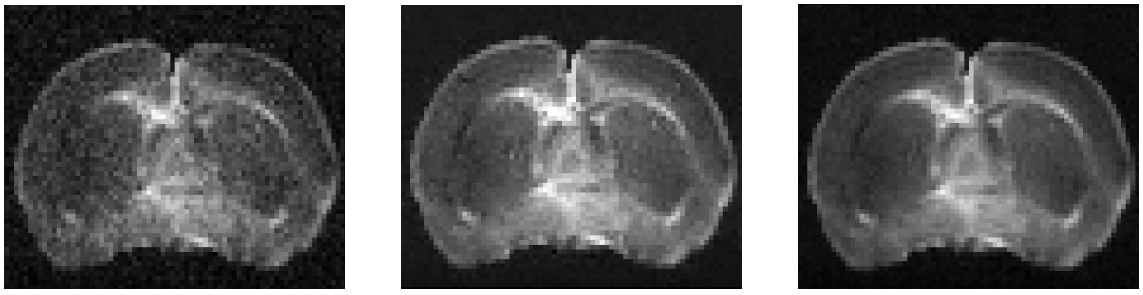

(a) Raw diffusion-weighted image.

(b) Denoised diffusion-weighted image using MPPCA.

(c) Denoised diffusion-weighted image using Rician noise removal.

Figure 5.12: Comparison of raw (left), MPPCA-denoised (middle), and Rician-denoised (right) diffusion-weighted images for the second diffusion direction. All images are shown with increased contrast.

Fig. 5.13 shows the difference between Rician noise and Gaussian noise, on the right.

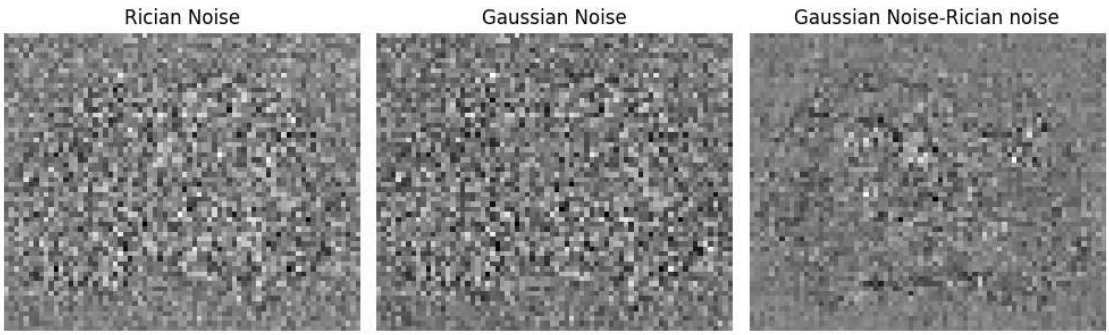

Figure 5.13: Residual noise maps obtained by subtracting the denoised images from the raw input. The left figure corresponds to Rician noise floor, the middle to MPPCA (Gaussian) noise, and the right shows the difference between the two residuals.

Since Rician denoising was selected (see Section 4.4), all subsequent results refer to images processed with this method.

5.4.2. Gibbs Ringing Removal

Figure 5.14 shows the effect of Gibbs ringing removal. Although some residual ringing remains, its intensity is reduced, with the effect being more noticeable in the b_0 image.

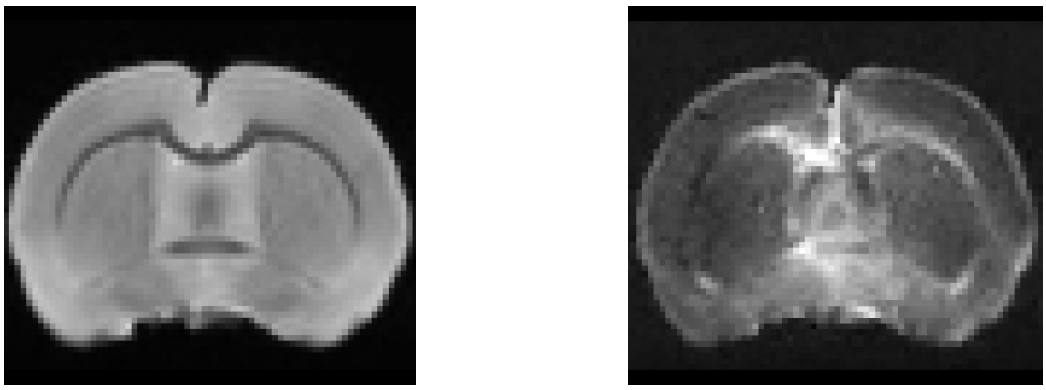

(a) b_0 image after Gibbs ringing removal.

(b) DWI (second direction) after Gibbs ringing removal.

Figure 5.14: Effect of Gibbs ringing removal on b_0 and diffusion-weighted image.

5.4.3. Masking, Normalisation and Powder Average

The splitting of diffusion-weighted and b_0 images is not shown here since it simply separates the datasets for subsequent processing. Next, the brain mask was

generated from the average b_0 image using Otsu thresholding, as illustrated in Figure 5.15a.

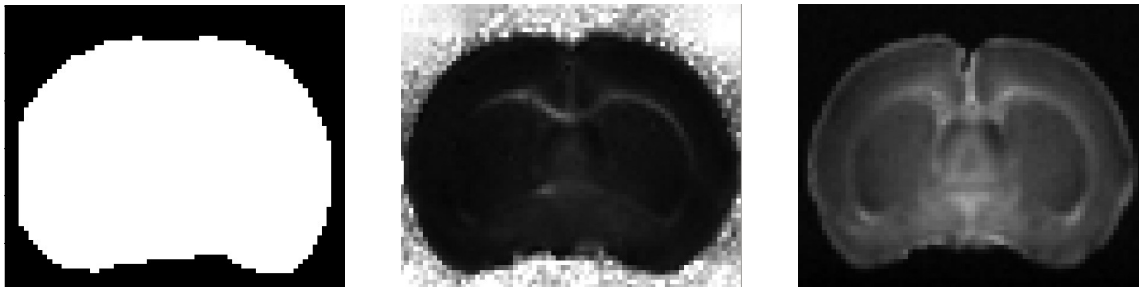

(a) Mask derived with Otsu thresholding.

(b) Normalized DWI (second direction).

(c) Powder average image.

Figure 5.15: Visualisation of mask generation, image normalisation, and powder averaging.

The following normalization enhanced the contrast between the corpus callosum and the rest of the brain structures, as illustrated in Figure 5.15b. Eventually, 5.15c shows the powder average derived from the diffusion image. In anisotropic regions such as the corpus callosum, structures appear slightly more blurred due to averaging across directions.

5.5. Parameters estimated from TDE

In this section, parameter estimates and their associated statistical results are presented. The section begins with the display of full maps for one control (RA.BML.3841) and one Alzheimer's subject (RA86). The statistical analysis of such diffusion metrics follows. For each parameter, except for ASF, values derived from TDE (as detailed in Section 4.5.1) are compared with those obtained from DTI. Eventually, group comparisons between the Alzheimer's disease and healthy control cohorts are performed.

5.5.1. Full maps Display

This section displays the diffusion parameter maps estimated for two representative subjects: a control rat (RA.BML.3841) and an Alzheimer's model rat (RA86).

Parallel diffusivity is higher in the corpus callosum compared to the cortex, while perpendicular diffusivity shows the opposite trend. The axonal signal fraction maps show high values in the corpus callosum, between 70–80%, with some outliers reaching 100%. In some slices, other white matter tracts, such as the corticofugal tract and the corona radiata, are also partially visible (see Figure 5.18). The microscopic fractional anisotropy maps highlight regions with well-aligned white matter fibers, and the highest values are found in the corpus callosum.

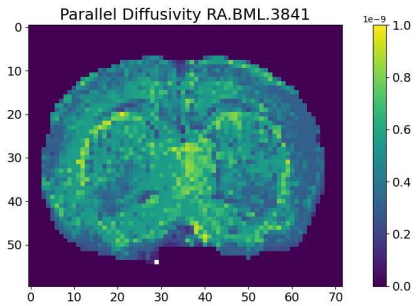

(a) Parallel Diffusivity.

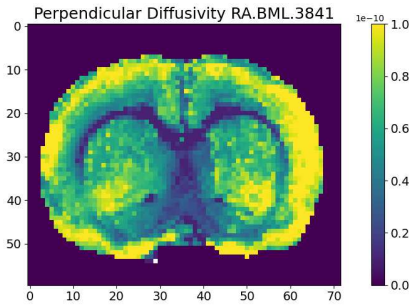

(b) Perpendicular Diffusivity.

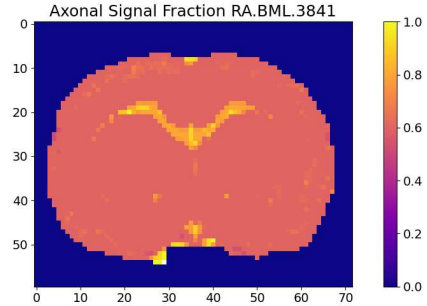

(c) Axonal Signal Fraction.

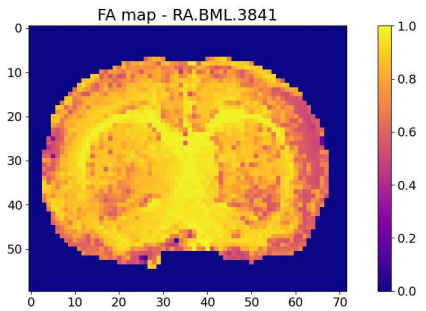

(d) Fractional Anisotropy.

Figure 5.16: Overview of estimated diffusivity-related maps from the TDE model for slice 9 of RA.BML.3841.

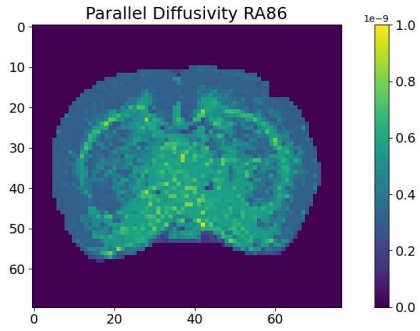

(a) Parallel Diffusivity.

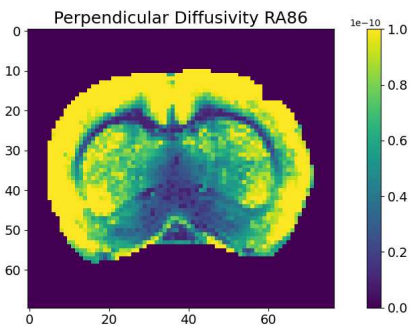

(b) Perpendicular Diffusivity.

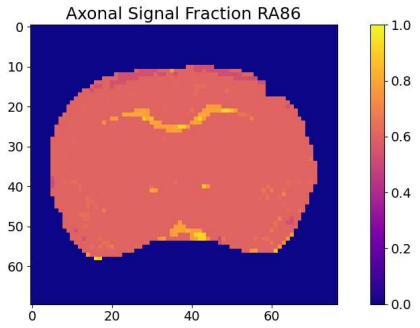

(c) Axonal Signal Fraction.

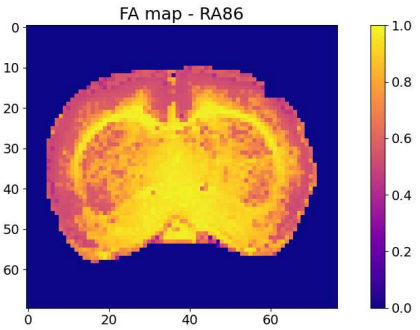

(d) Fractional Anisotropy.

Figure 5.17: Overview of estimated diffusivity-related maps from the TDE model for slice 9 of RA86.

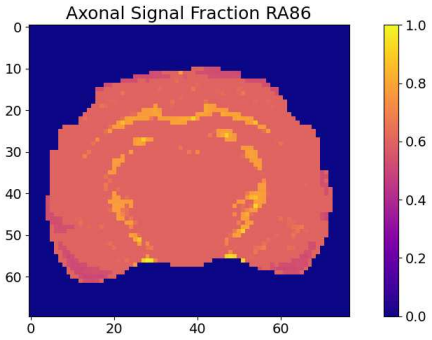

Figure 5.18: Axonal signal fraction in slice 6 of RA86, highlighting the corona radiata.

Figure 5.19 shows the effect of Rician denoising on the subject with the lowest SNR (RA71). Although the difference is modest, the corpus callosum appears more defined and thicker after Rician noise floor removal.

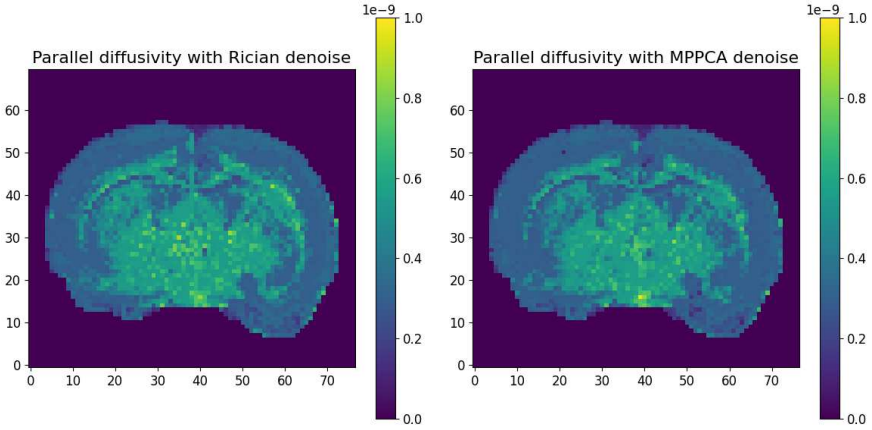

Figure 5.19: Comparison of parallel diffusivity map for RA71 from the images with Rician denoising (left) and MPPCA one (right).

5.5.2. Parallel diffusivity

This section analyzes the parallel diffusivity estimates.

Comparison of DTI vs TDE method in the control group

The normality tests proved that only the DTI estimates in the corpus callosum were normally distributed. Figure 5.20 shows the voxel-wise distribution of AxD values for both methods in white matter and gray matter.

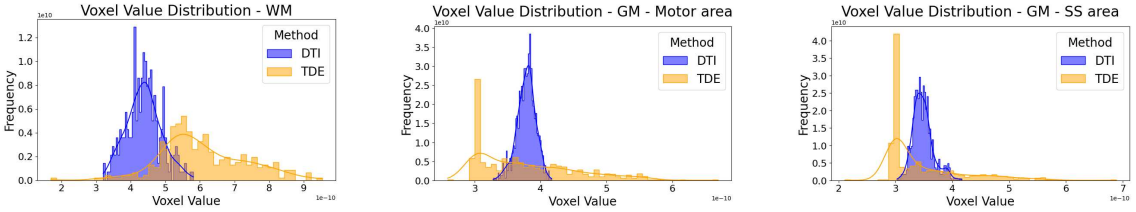

(a) Voxel distribution of WM.

(b) Voxel distribution of motor cortex (GM).

(c) Voxel distribution of somatosensory cortex (GM).

Figure 5.20: Histogram of voxel-wise AxD values across all slices, for DTI and TDE methods.

Comparing DTI and TDE within each ROI showed significant differences: $p = 6.67 \times 10^{-68}$ in WM, $p = 2.28 \times 10^{-7}$ in GM motor area, and $p = 5.11 \times 10^{-26}$in GM somatosensory area. Statistical significance was also found within each method between the two cortical areas. Additionally, the bootstrap 95% confidence interval for the mean or median difference shows that parallel diffusivity in WM is higher with TDE than with DTI. In contrast, the interval for GM indicates that parallel diffusivity estimated with DTI is higher than the one for TDE. This finding is further supported by the mean values presented in Table 5.2.

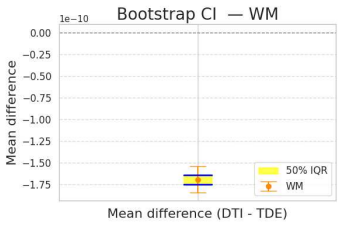

(a) Bootstrap distribution for WM.

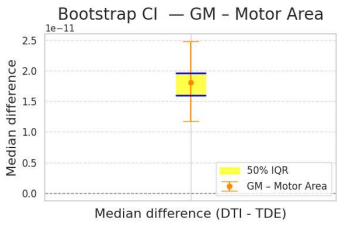

(b) Bootstrap distribution for GM, motor cortex.

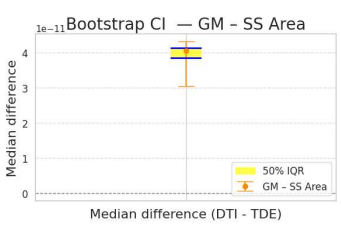

(c) Bootstrap distribution for GM, somatosensory (SS) cortex.

Figure 5.21: Bootstrap 95% confidence intervals for the mean or median difference in AxD between TDE and DTI in WM (left), motor area (middle), and somatosensory area (right). Yellow boxes indicate the interquartile range.

Label	Method	Mean [m^2/s]	Variation DTI-TDE [%]
WM	DTI	4.38×10^{-10}	-38.73%
WM	TDE	6.07×10^{-10}	
GM (motor)	DTI	3.78×10^{-10}	0.06%
GM (motor)	TDE	3.77×10^{-10}	
GM (ss)	DTI	3.48×10^{-10}	0.56%
GM (ss)	TDE	3.46×10^{-10}	

Table 5.2: Table showing the mean values of axial diffusivity for each ROI and method, along with the mean percentage difference between DTI and TDE methods.

Comparison between Healthy and Alzheimer's rats

The data were found to be non normal and a Mann-Whitney U test was performed, which revealed statistical significance between Alzheimer and control rats of 4 months of age for every label and method. To highlight differences, mean values and the percentage of variation between the two groups in the same ROI and with the same method were calculated and displayed in Tables 5.3 and 5.4.

The 95% CI bootstrap distribution of the median difference is displayed in Fig. 5.22. Parallel diffusivity is lower in Alzheimer's rats compared to controls when measured with the TDE method in the three ROIs, whereas no clear pattern is observed with the DTI method.

Group	Method	Label	Mean AxD [m^2/s]
Alzheimer	DTI	WM	4.07×10^{-10}
Alzheimer	DTI	GM (motor)	3.87×10^{-10}
Alzheimer	DTI	GM (ss)	3.55×10^{-10}
Alzheimer	TDE	WM	4.91×10^{-10}
Alzheimer	TDE	GM (motor)	3.15×10^{-10}
Alzheimer	TDE	GM (ss)	3.06×10^{-10}
Control	DTI	WM	4.38×10^{-10}
Control	DTI	GM (motor)	3.78×10^{-10}
Control	DTI	GM (ss)	3.48×10^{-10}
Control	TDE	WM	6.07×10^{-10}
Control	TDE	GM (motor)	3.78×10^{-10}
Control	TDE	GM (ss)	3.46×10^{-10}

Table 5.3: Table showing the mean parallel diffusivity of each tissue type, distinguished by method and group.

Method	Label	Variation [%]
DTI	WM	-7.04
DTI	GM (motor)	2.45
DTI	GM (ss)	2.11
TDE	WM	-19.21
TDE	GM (motor)	-16.64
TDE	GM (ss)	-11.60

Table 5.4: Table showing the percentage mean difference of parallel diffusivity between Alzheimer and control rats of each tissue type, distinguished by method.

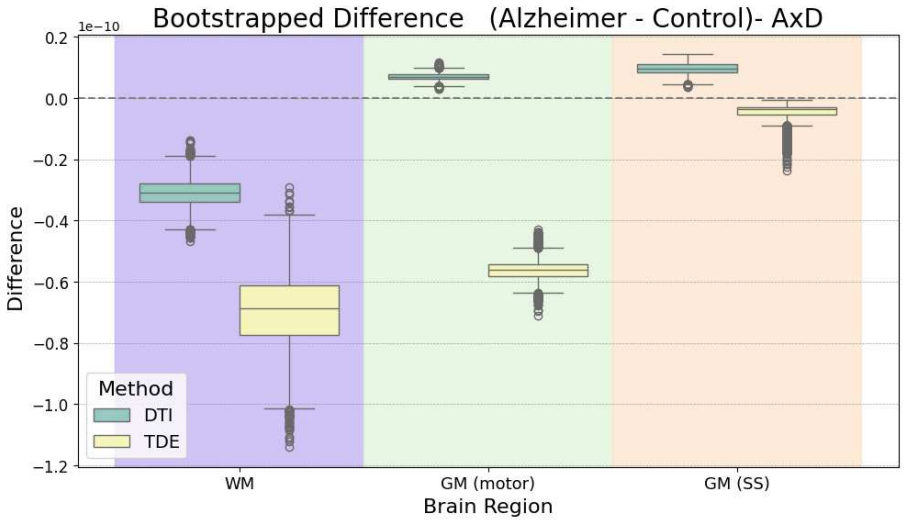

Figure 5.22: Plot of the bootstrap distribution for parallel diffusivity.

5.5.3. Perpendicular diffusivity

In this section, the analysis of perpendicular diffusivity is reported.

Comparison of DTI vs TDE method in the control group

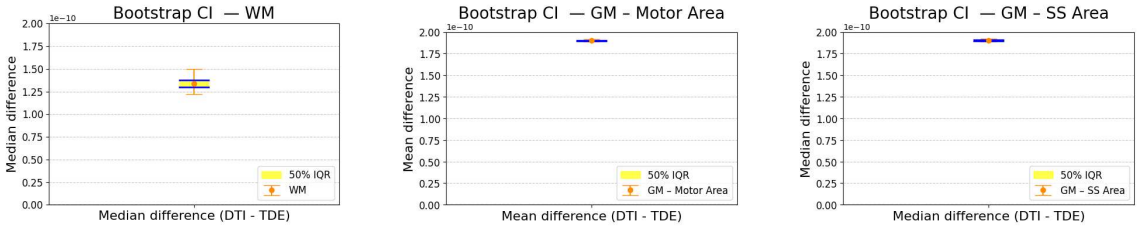

(a) Bootstrap distribution for WM.

(b) Bootstrap distribution for GM, motor area.

(c) Bootstrap distribution for GM, somatosensory area.

Figure 5.23: 95% confidence intervals for the mean or median difference between DTI and TDE estimates of perpendicular diffusivities. The yellow band highlights the 50% interquartile range. WM is shown on the left, motor area of GM in the middle, and somatosensory area of GM on the right. Note that the intervals in WM are very narrow.

Due to non-normality of the data, the Mann-Whitney U test was applied. Results showed statistically significant differences between the two methods in each ROI, with $p = 1.88 \times 10^{-93}$ for WM, $p = 7.93 \times 10^{-262}$ for GM (motor area), and $p = 6.31 \times 10^{-221}$ for GM (somatosensory area). Significant differences are also found between the 2 ROIs of GM. Moreover, the bootstrap 95% CI for mean or median difference revealed that perpendicular diffusivity in both WM and GM is higher with DTI than TDE (Fig. 5.23)

Comparison between Healthy and Alzheimer's rats

The data were again non-normal, so a Mann-Whitney U test was performed. Statistical significance between Alzheimer's and control rats was observed for GM across all labels and methods, except for DTI in the somatosensory area. For WM, only the TDE method showed a statistically significant difference. To assess this, mean values and the percentage of variation between the two groups in the same ROI and with the same method are calculated and displayed in Tables 5.5 and 5.6.
The bootstrap distribution plot confirms the lack of significance for DTI in WM, as its 50% interquartile range crosses zero. Instead, the plot for the TDE method shows that the perpendicular diffusivity of the Alzheimer rats is higher than the control ones. Interestingly, while the mean variation in white matter reaches 38%, the bootstrap confidence interval is relatively narrow. This discrepancy is likely due to the use of the median in the bootstrap estimation, in presence of a skewed distribution.

Group	Method	Label	Mean RD [m^2/s]
Alzheimer	DTI	WM	1.61×10^{-10}
Alzheimer	DTI	GM (motor)	2.92×10^{-10}
Alzheimer	DTI	GM (ss)	2.97×10^{-10}
Alzheimer	TDE	WM	1.91×10^{-11}
Alzheimer	TDE	GM (motor)	1.14×10^{-10}
Alzheimer	TDE	GM (ss)	1.11×10^{-10}
Control	DTI	WM	1.63×10^{-10}
Control	DTI	GM (motor)	2.89×10^{-10}
Control	DTI	GM (ss)	2.96×10^{-10}
Control	TDE	WM	1.37×10^{-11}
Control	TDE	GM (motor)	9.92×10^{-11}
Control	TDE	GM (ss)	1.01×10^{-10}

Table 5.5: Mean perpendicular diffusivity in each tissue type, distinguished by method and group.

Method	Label	Variation [%]
DTI	WM	-1.04
DTI	GM (motor)	1.06
DTI	GM (ss)	0.51
TDE	WM	38.64
TDE	GM (motor)	15.07
TDE	GM (ss)	10.59

Table 5.6: Table showing the percentage mean difference of perpendicular diffusivity between Alzheimer and control rats of each tissue type, distinguished by method.

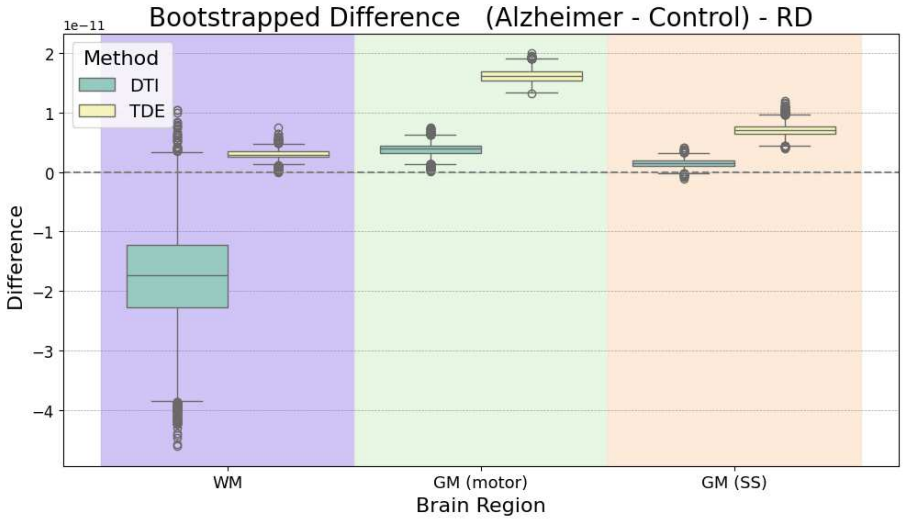

Figure 5.24: Plot of the bootstrap distribution for perpendicular diffusivity.

5.5.4. Fractional Anisotropy

This section describes the results for fractional anisotropy.

Comparison of DTI vs TDE method in the control group

The normality test revealed that only the DTI data acquired in the somatosensory cortex were normal, but due to the comparison with a non normal dataset, the Mann-Whitney U test was applied. This revealed statistically significant differences between the two methods in the control group, with p-values of 4.02×10^{-29}, 4.04×10^{-64}, and 7.41×10^{-56} for WM and GM in motor cortex, and GM in somatosensory cortex, respectively. Significance was also found between the two areas of gray matter. Moreover, the bootstrap 95% confidence interval for the mean or median difference showed that FA in both WM and GM is higher when estimated with TDE compared to DTI. The difference is between 0.4 and 0.5 for both regions.

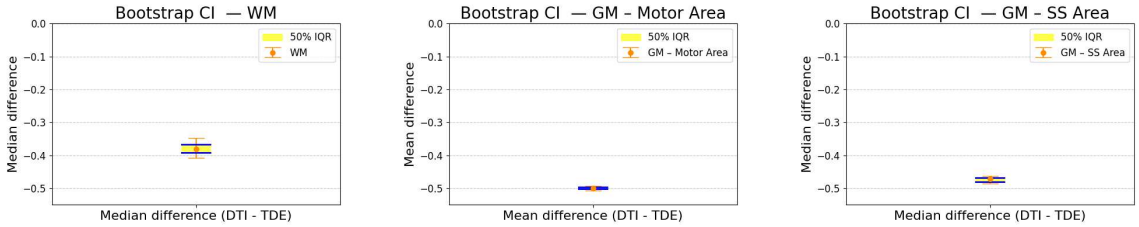

(a) Bootstrap distribution for WM.

(b) Bootstrap distribution for GM, motor area.

(c) Bootstrap distribution for GM, somatosensory area.

Figure 5.25: 95% confidence intervals for the mean or median difference between DTI and TDE estimates of fractional anisotropy. The yellow band highlights the 50% interquartile range. WM is shown on the left, motor area of GM in the middle, and somatosensory area of GM on the right. Note that the intervals in WM are very narrow.

Comparison between Healthy and Alzheimer's rats

The Mann-Whitney U test was performed, which showed statistical significance between Alzheimer and control rats for the TDE acquisitions. For the DTI ones, only the somatosensory cortex registered the difference. To support these findings, the mean FA values and percentage variations between the two groups for each ROI and method are summarized in Tables 5.7 and 5.8.

The 95% CI bootstrap distribution is displayed in Fig. 5.26. The CIs for FA calculated with DTI touch zero, consistent with the lack of significance observed in the Mann-Whitney test. The CI derived for the TDE estimates, confirm the trend of the statistical test, with decreased FA for the Alzheimer's rat, more remarkably in motor area GM.

Group	Method	Label	Mean FA
Alzheimer	DTI	WM	0.52
Alzheimer	DTI	GM (motor)	0.16
Alzheimer	DTI	GM (ss)	0.13
Alzheimer	TDE	WM	0.94
Alzheimer	TDE	GM (motor)	0.56
Alzheimer	TDE	GM (ss)	0.56
Control	DTI	WM	0.57
Control	DTI	GM (motor)	0.17
Control	DTI	GM (ss)	0.12
Control	TDE	WM	0.97
Control	TDE	GM (motor)	0.67
Control	TDE	GM (ss)	0.64

Table 5.7: Table showing the mean FA of each tissue type, distinguished by method and group.

Method	Label	Variation [%]
DTI	WM	-8.76
DTI	GM (motor)	-10.71
DTI	GM (ss)	12.21
TDE	WM	-3.15
TDE	GM (motor)	-16.38
TDE	GM (ss)	-11.94

Table 5.8: Table showing the mean percentage difference of FA between Alzheimer and control rats of each tissue type, distinguished by method.

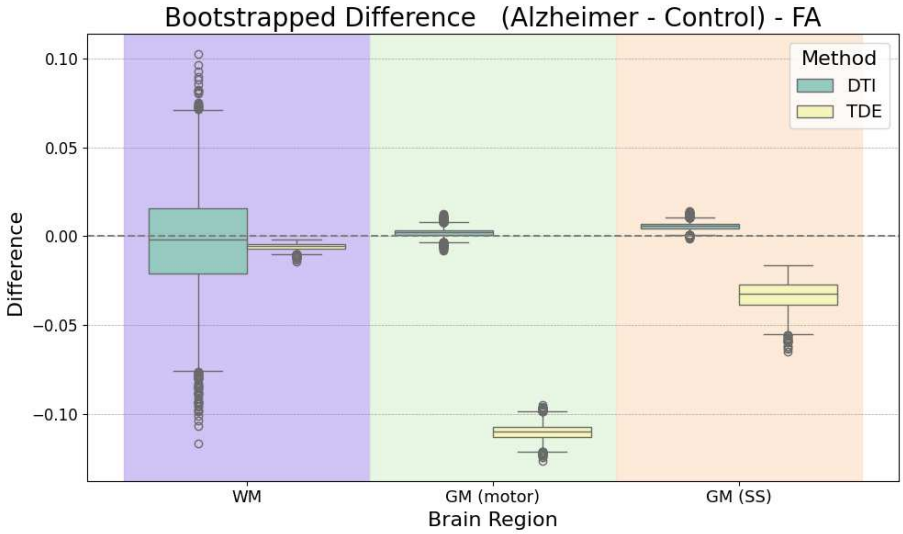

Figure 5.26: Plot of the bootstrap distribution for FA.

5.5.5. Axonal Signal Fraction

This section presents the analysis of the axonal signal fraction, which was computed only for the TDE acquisitions.

Comparison between Healthy and Alzheimer's rats

The data were found to be non-normal and a Mann-Whitney U test was performed. A statistically significant difference was found between Alzheimer and control rats in GM (especially in motor cortex), but not in WM. Additionally, significant differences were found between the two cortical areas.
Tables 5.9 and 5.10 report the mean ASF values and the percentage differences between the groups for each tissue type.

Group	Label	Mean ASF
Alzheimer	WM	0.75
Alzheimer	GM (motor)	0.59
Alzheimer	GM (ss)	0.606
Control	WM	0.74
Control	GM (motor)	0.61
Control	GM (ss)	0.60

Table 5.9: Table showing the mean ASF of each tissue type for TDE data.

Label	Variation [%]
WM	1.56
GM (motor)	-3.69
GM (ss)	-0.36

Table 5.10: Table showing the mean percentage difference of ASF between the mean Alzheimer and control rats of each tissue type.

The 95% CI bootstrap distribution of the mean or median difference is displayed in Fig. 5.28. It shows no significance for any tissue type. In fact in WM, the confidence interval (built on the mean) includes zero, and in GM the intervals (built on the median) are approximated to 0, indicating no difference, even if the test stated the opposite. The data distributions are displayed to motivate this trend in Figure 5.27.

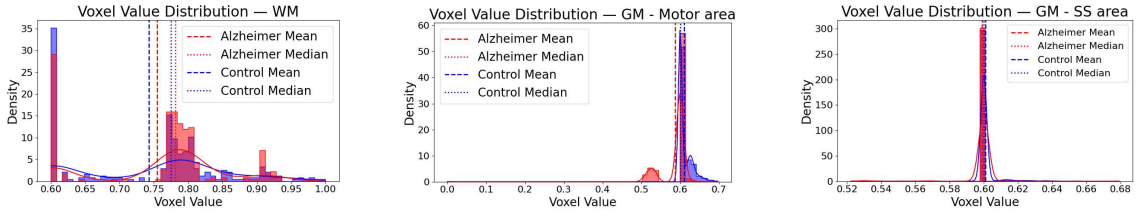

(a) Voxel distribution of WM.

(b) Voxel distribution of motor cortex (GM).

(c) Voxel distribution of somatosensory cortex (GM).

Figure 5.27: Histogram of voxel-wise ASF values across all slices for the different ROIs.

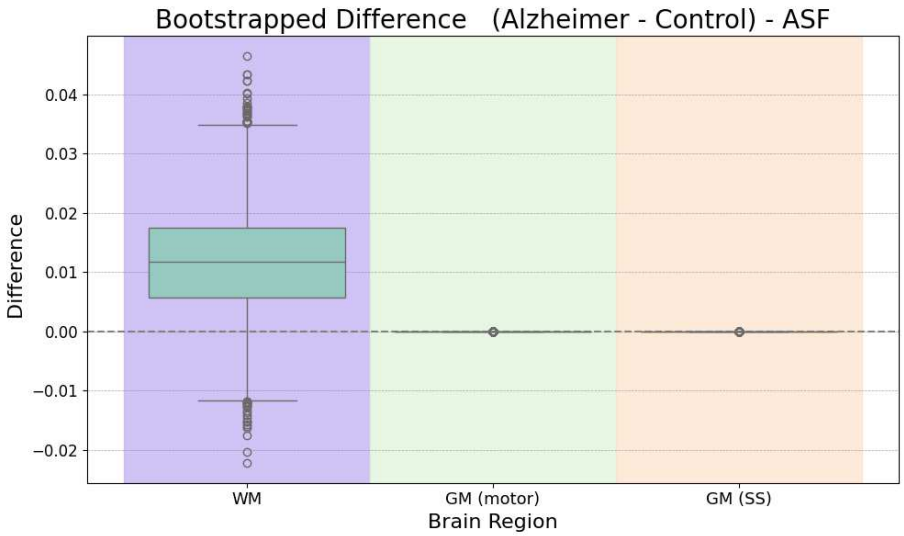

Figure 5.28: Bootstrap distribution of the mean ASF difference between Alzheimer and control rats. The yellow area highlights the 50% interquartile range.

5.5.6. Older Alzheimer's rat

The results for the 17-month-old subject are displayed in this section.

Perpendicular diffusivity, ASF, and FA exhibit trends similar to those observed in 4-month-old rats. However, the parallel diffusivity map does not clearly delineate the corpus callosum. Although a dark intensity band may be mistaken for the corpus callosum, it is in fact not part of this structure. When a region of interest of the corpus callosum—extracted from the perpendicular diffusivity map—is overlaid on the parallel diffusivity image, it highlights an area located just above the dark band, but which does not differ in contrast from the cortex (see Figure 5.30a).
Means are reported in Table 5.11 and are compared with the corresponding values from the 4-month-old cohort.
The TDE-derived parallel diffusivity map for the 17-month-old subject shows notable differences relative to the younger rats. In gray matter, parallel diffusivity is higher than in both the Alzheimer's disease and control groups at 4 months, while in white matter, it is higher than in the AD group but lower than in controls. Additionally, the mean values in WM and GM are very similar, resulting in limited tissue contrast. The DTI-derived axial diffusivity in WM is comparable to the mean value observed in the AD group, while in GM it aligns more closely with the control group. In terms of TDE radial diffusivity, the value in GM is lower than that of both the AD and control groups. In WM, it is only slightly elevated. This pattern contrasts with that observed in the GM DTI data, where the trend is reversed. The WM value aligns with both groups of younger rats. Microscopic fractional anisotropy is higher in both GM and WM compared to the 4-month-old rats, again displaying an opposite trend with respect to the GM DTI-derived FA values. The WM value aligns with the younger Alzheimer group. Lastly, the ASF in WM is slightly increased compared to the younger cohort, while the value in GM remains essentially unchanged.

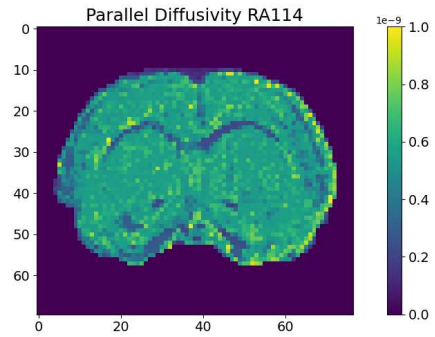

(a) Parallel Diffusivity

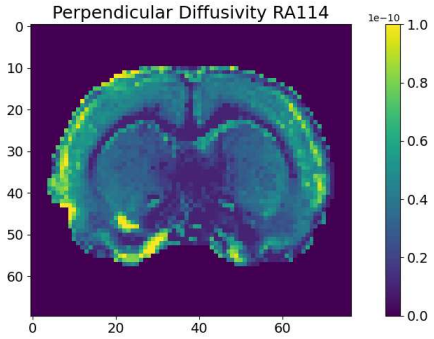

(b) Perpendicular Diffusivity

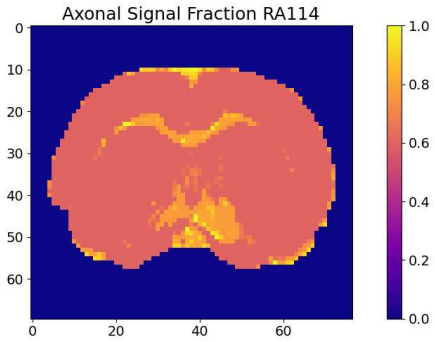

(c) Axonal Signal Fraction (FA)

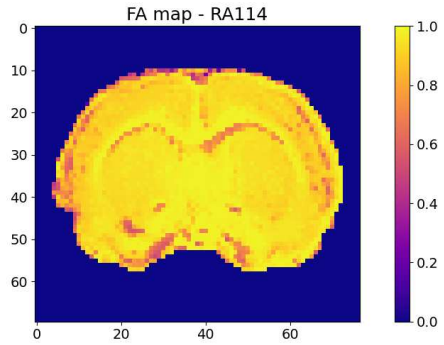

(d) Fractional Anisotropy

Figure 5.29: Overview of estimated diffusivity-related maps from the TDE model for slice 12 of RA114.

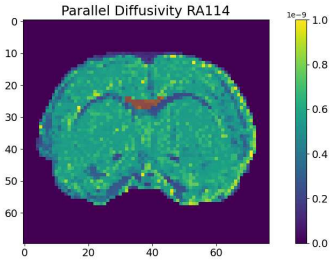

(a) Parallel diffusivity map for RA114 with a ROI overlaid on the corpus callosum, estimated with TDE.

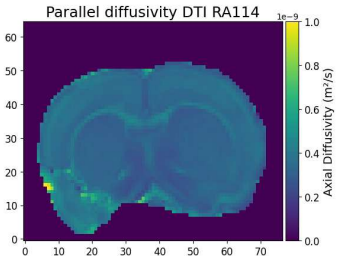

(b) Parallel diffusivity map for RA114 estimated with DTI.

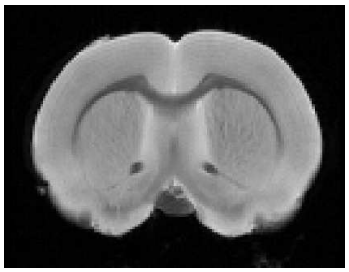

(c) T2-weighted anatomical scan of RA114 to compare the anatomical structures in the diffusivity maps.

Figure 5.30: Comparison of parallel diffusivity maps estimated with TDE and DTI alongside the corresponding anatomical T_2-weighted scan for subject RA114.

Method	Label	Mean AxD [m^2/s]	Mean RD [m^2/s]	Mean FA	Mean ASF
DTI	WM	4.06×10^{-10}	1.65×10^{-10}	0.52	–
DTI	GM	3.77×10^{-10}	2.98×10^{-10}	0.14	–
TDE	WM	5.74×10^{-10}	1.09×10^{-11}	0.98	0.60
TDE	GM	5.80×10^{-10}	4.76×10^{-11}	0.91	0.79

Table 5.11: Mean values of the extracted parameters in the two regions of interest, divided by method.

5.6. Axonal T_2

This section presents the estimates for axonal T_2.

The estimates of T_{2a} are displayed in Figure 5.31. The map obtained with the spherical mean technique is cleaner; however, the corpus callosum is distinguishable in both structures. The mean T_2 calculated in the ROI surrounded by the red mark was 125 ms for T_{2mean}, 72 ms for T_{2var} using Eq. 3.83, and 71 ms for T_{2var} using Eq. 3.87. The visual inspection of the T_2 map obtained with spherical harmonics expansion of the signal does not reveal any SNR improvement.

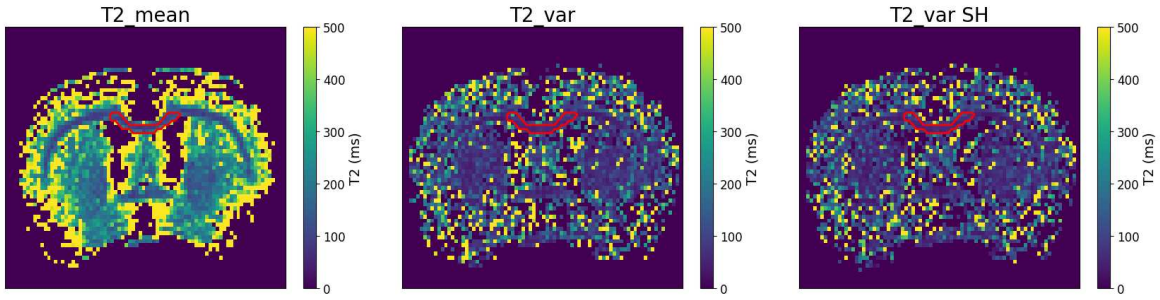

(a) Axonal T_2 map estimated with the spherical mean technique.

(b) Axonal T_2 map estimated with the spherical variance technique, using the raw signal.

(c) Axonal T_2 map estimated with the spherical variance technique, using the spherical harmonics expansion.

Figure 5.31: Axonal T_2 maps obtained with spherical mean (left) and spherical variance (right and middle) techniques. The red line marks the ROI where the mean T_2 was calculated for comparison.

6 | Discussion

This chapter discusses the findings presented in Chapter 5, divided in topics.

6.1. PGSE implemented as a gradient waveform

The results indicate that the waveform-based software implementation can produce signal quality comparable to that of the standard PGSE acquisition when all relevant parameters are carefully matched and the hardware limitations are taken into account. The process of aligning the two sequences was useful in understanding the role of individual parameters and how they interact with each other, particularly in terms of bandwidth, echo time, and readout lines. This achieved equivalence is significant, as it enables the use of more advanced diffusion encoding strategies—such as tensor-valued encoding—to probe tissue microstructure beyond conventional single-directional approaches.

6.2. Choice of the voxel size

Figures 5.3 and 5.4 prove that SNR increases with voxel volume, but also show that larger voxels are more susceptible to partial volume effects, as the edges of anatomical structures are more blurred.
The observed rise in SNR between the 0.2 mm and 0.75 mm slices was smaller than expected, given that the signal scales linearly with voxel volume and with the square root of the number of voxels [55]. Considering the same in-plane resolution and the same number of voxels, increasing the slice thickness from 0.2 mm to 0.75 mm results in a 3.75-fold larger voxel volume and a 3.75-fold expected increase in SNR. However, the SNR improved only by a factor of 1.73, and this discrepancy can be attributed to partial volume effects. While larger voxels accumulate more signal—due to the inclusion of more protons—they also average across different tissue types, potentially reducing contrast and contributing to a different SNR scaling.
These findings highlight the trade-off between spatial resolution and SNR. Although high-resolution images inherently have lower SNR, they may offer better anatomical contrast and reduced partial volume effects. In this case, SNR was prioritized over spatial resolution because the main acquisition sequence—TDE—used very high b-values and a long echo time, both of which require a high initial SNR to compensate for the substantial diffusion-related signal attenuation. An average SNR of 55 in the b_0 image was found to be sufficient to ensure reliable signal detection in the diffusion-weighted volume. Figures 5.7 and 5.8 demonstrate the need for increased

slice thickness to achieve adequate SNR in the TDE images.

6.3. TDE

This section presents the results obtained using tensor-valued diffusion encoding, beginning with a general overview based on the full maps shown in Section 5.5.1, followed by a focused statistical analysis comparing the two subject groups and methods.

6.3.1. Full maps

The developed TDE approach yielded diffusivity parameter maps that preserve distinct anatomical contrast, particularly for the perpendicular diffusivity. Conversely, the estimates of parallel diffusivity appear noisier. This can be attributed to the high parallel b-value employed in the acquisition. As shown in the Appendix and in [31] analytically, the variance of $D_{\parallel}$ increases with higher $b_{\parallel}$ and $b_{\perp}$. However, in the current implementation, a high $b_{\parallel}$ is needed to suppress extracellular signal. Despite this limitation, both parallel and perpendicular diffusivity estimates fall within expected physiological ranges: approximately 10^{-10} to $10^{-9}\,\mathrm{m}^2/\mathrm{s}$ for $D_{\parallel}$, and 10^{-11} to $10^{-10}\,\mathrm{m}^2/\mathrm{s}$ for $D_{\perp}$ [77].
The axonal signal fraction estimates obtained in this study are also consistent with previous reports in the literature. Higher values were observed in white matter compared to gray matter, as expected, with further reductions near the cortical boundary. The quantitative values—around 70–80% in white matter and 60% in gray matter—align with estimates that the extracellular space comprises approximately 15–30% of brain tissue volume [39, 71].
Microscopic fractional anisotropy (μFA) findings indicate high levels of directional diffusion, particularly in white matter regions. Values approached 1 in white matter and were approximately 0.6 in gray matter, consistent with expectations based on the underlying microstructural organization of these tissues and previous studies [37]. The μFA metric, being orientation-dispersion independent, offers a more specific characterization of microscopic anisotropy, compared to conventional DTI-derived FA, which is not rotationally invariant. This makes μFA more sensitive to pathological changes, such as those observed in Alzheimer's disease, by enabling the disentanglement of true microstructural alterations from fiber orientation dispersion [2].
These results support the use of tensor-valued diffusion encoding as a valuable acquisition strategy in preclinical diffusion MRI.

6.3.2. General considerations on statistical tests

In general, the data obtained from tensor-valued diffusion encoding did not follow a normal distribution. This outcome was expected due to the higher noise content of TDE signals. In contrast, some of the ROIs derived from diffusion tensor imaging displayed distributions more closely resembling normality.

When interpreting group differences or regional variations, it is essential to consider multiple layers of statistical information. While the Mann–Whitney U test is a robust nonparametric method for detecting differences between groups, it evaluates variation in the overall distributions of the data—not necessarily discrepancies in medians or means. Importantly, a significant result from the Mann–Whitney U test does not guarantee a difference in central tendency. This can occur, for example, if one group has greater variability or a skewed distribution, even when the means or medians are equal. This situation arose in the analysis of axonal signal fraction. Although the Mann–Whitney U test reports a statistically significant difference between groups, the bootstrap-derived confidence intervals for the mean overlap substantially, and both groups are assigned nearly identical mean values. As illustrated in Figure 5.27b, which shows the voxel-wise distribution of ASF in the gray matter motor area, the skewness of the distributions is in opposite directions for the two groups. This difference in skewness contributes to variations in overall distribution shapes without meaningful shifts in central tendency. Thus, while the Mann–Whitney U test detects a distributional difference, it may not reflect a biologically meaningful change in average voxel values. Therefore, relying solely on p-values without contextualizing the data can be misleading. To obtain a more comprehensive understanding of group differences, it is crucial to supplement hypothesis testing with descriptive statistics such as means, medians, and confidence intervals obtained through bootstrap resampling.
This multi-faceted approach is particularly important in studies with limited sample sizes and substantial biological variability, such as those commonly encountered in preclinical diffusion MRI.

Significant differences were found between the parameter estimates obtained with TDE and those from conventional DTI. These findings support the theoretical advantages of TDE, which, by introducing correlations between diffusion directions, helps resolve degeneracies in multi-compartment models and provides greater sensitivity to parallel diffusivity. While partial volume effects still influence the estimates, only TDE was able to reliably detect these changes. Unlike DTI, which conflates intra- and extra-axonal signals and is confounded by fiber orientation dispersion, TDE enables a more specific characterization of microstructural features [26, 58]. Notably, parallel and perpendicular diffusivities, as well as axonal signal fraction, can be extracted directly from the TDE signal at high b-values. In contrast, DTI requires fitting a tensor model to the data, imposing assumptions that yield composite metrics rather than compartment-specific parameters. Moreover, since DTI does not distinguish between tissue compartments, it cannot provide estimates of ASF. Other models, such as the one introduced by Kaden et al. [35] and described in Section 3.2.2, could be used to derive compartment-specific properties, including ASF. However, as anticipated, these approaches rely on stronger modeling assumptions—such as the tortuosity constraint—and involve more complex and computationally intensive fitting procedures compared to tensor-valued encoding.

In this context, TDE emerges as a sensitive and powerful tool, allowing for more direct and computationally efficient estimation of microstructural parameters, while reducing reliance on complex model fitting and strong prior assumptions.

6.3.3. Parallel diffusivity

The comparison between DTI and TDE estimates shows that TDE provides a broader sensitivity range for $D_{\parallel}$. Specifically, TDE yields higher estimates in white matter and lower estimates in gray matter compared to DTI, suggesting that it captures more effectively the compartment-specific properties of these tissues. In the Alzheimer's group, $D_{\parallel}$ is reduced compared to controls, as evidenced by both the group-wise means and the bootstrap confidence intervals. This decrease may reflect axonal degeneration processes characteristic of AD, such as axonal swelling (see Sec. 3.5) [6]. Swellings can cause deviations from the ideal cylindrical geometry of axons, possibly resulting in reduced directional diffusivity along their length. The reduction in $D_{\parallel}$ is more pronounced in white matter than in gray matter. Within gray matter, the motor region shows the largest effect. Both motor and somatosensory cortices send commissural fibers through the midbody of the corpus callosum [48]. The stronger involvement of motor regions may reflect a higher proportion of motor-related fibers crossing through the analyzed segment of the corpus callosum, making them more susceptible to early microstructural alterations in Alzheimer's disease.

6.3.4. Perpendicular Diffusivity

Perpendicular diffusivity estimated with TDE is reduced compared to that obtained with DTI, and, as expected, it is smaller in white matter than in gray matter due to fiber alignment restricting diffusion in the perpendicular direction. Notably, TDE values are approximately an order of magnitude lower than those from DTI and align more closely with literature values [77].
In the Alzheimer's group, radial diffusivity is higher than in controls, particularly in white matter. Consistently with $D_{\parallel}$, motor cortex experiences bigger variation than somatosensory cortex. This increase aligns with the presence of axonal swellings previously discussed, which may disrupt fiber coherence and allow greater diffusion perpendicular to the axonal axis. The increased TDE estimates further confirm this interpretation, reflecting the method's greater sensitivity to microstructural alterations.

6.3.5. Fractional anisotropy

Fractional anisotropy estimated with TDE was higher than that obtained with DTI, supporting TDE's ability to factor out fiber orientation effects and provide more precise microstructural information. TDE was able to detect significant FA differences across all three tissue types, showing lower FA values in the pathological group, while DTI demonstrated limited sensitivity. The observed FA reduction likely reflects a loss of fiber coherence, consistent with axonal degeneration processes in Alzheimer's disease. Interestingly, the largest FA changes were observed in gray matter (particularly in the motor cortex), contrasting with the diffusivity metrics, where white matter differences were more evident.

6.3.6. Axonal Signal Fraction

TDE revealed minimal differences between healthy and pathological subjects in gray matter, and no detectable changes in white matter. However, the subtle gray matter alterations were not reflected in indices of central tendency, as discussed in Section 6.3.2. This apparent lack of sensitivity may be attributed to axonal degeneration that has not yet progressed to substantial axonal loss in these early disease stages, thereby resulting in little to no change in overall axonal signal fraction. Assuming no variations in T_2, the ratio between axonal volume and total tissue volume remains constant.

6.3.7. Parameters summary

In light of these results, diffusivity measures emerged as the most sensitive parameters for detecting early-stage Alzheimer's disease, particularly due to notable alterations observed in the corpus callosum.
Studying diffusivity in the cortex and corpus callosum represents a promising early biomarker for Alzheimer's disease. Pathologically, amyloid-β plaques are known to accumulate initially in medial temporal lobe structures such as the hippocampus and cingulate cortex, while tau aggregates first appear in the locus coeruleus before spreading to the entorhinal cortex and hippocampus [50]. Because of the localization of this pathology and its associated neurodegeneration, AD has traditionally been viewed as a disease of the brain's gray matter. However, in recent years, neuroimaging studies have increasingly implicated both micro- and macrostructural white matter abnormalities in the risk and progression of AD. These findings support the hypothesis that, beyond the hallmark neuronal loss, white matter degeneration and demyelination are also key features of the disease process [49].

Given this, triple diffusion encoding has emerged as a promising tool to study white matter alterations, with significant differences observed between control and TgF344-AD rats. Measuring diffusivity using diffusion MRI could therefore offer a groundbreaking, non-invasive method for early detection of AD-related microstructural changes.
However, while TDE has shown sufficient sensitivity to detect these differences, current protocols are too time-intensive for in vivo applications. Thus, optimizing the acquisition protocol to reduce the duration of the scan is essential to enable its use in preclinical or even clinical in vivo studies.

6.4. Diffusion time and compartmental exchange

An important consideration when interpreting diffusion-weighted signals is the degree of water exchange between microstructural compartments during the diffusion encoding period. Specifically, the permeability of the axonal myelin sheath may become relevant due to the relatively long echo times (TE $\geq$ 50 ms) employed in the TDE acquisition used in this study. Studies [4, 31] have shown that in vivo exchange times can extend up to 1 s or even longer in ex vivo conditions. Given

that the TE applied in this study is 50 ms and the effective diffusion time is even shorter, the intra-axonal space can be considered effectively isolated throughout the diffusion encoding period.

While diffusion times along each encoding direction in the TDE protocol can be calculated individually, defining a general effective diffusion time is less straightforward due to the multiple gradient waveforms. A rigorous determination would require analyzing the power spectrum of the encoding gradients, as proposed in [32], which is beyond the scope of this work.

In contrast, exchange between glial cells and the extracellular space occurs on shorter timescales (∼25–50 ms) and may be non-negligible at some diffusion times. However, the use of high b-values substantially attenuates signal from the extracellular compartment. Therefore, exchange dynamics involving these compartments have minimal impact on the observed diffusion contrast.

Taken together, these considerations demonstrate that despite the relatively long echo time used in TDE acquisitions, exchange between axons and the extracellular space remains negligible, thereby simplifying the diffusion model.

6.5. Older Alzheimer's rat

The TDE-derived parameters estimated for the 17-month-old Alzheimer's rat do not follow the expected progression of AD. Given the degenerative nature of the disease, it would be reasonable to expect a continuation or amplification of the trends observed in the 4-month-old Alzheimer cohort. This, however, is not the case. Parallel diffusivity, FA, and ASF derived from TDE are increased in both GM and WM compared to the younger rats, which is opposite to the expected pattern of degeneration. (ASF only slightly). Rather than reflecting a decline in microstructural integrity, these elevated values suggest either a non-pathological state or an anomalous measurement inconsistent with typical AD progression. DTI also failed to show a clear difference in AD compared to the younger cohort. For some parameters, such as those in GM, DTI reflected the expected trend, but in WM it struggled to distinguish between groups. The absence of contrast in the TDE maps may be due to significant neuronal loss that alters the microstructural properties of the tissue. Partial volume effects might also contribute; however, this is considered unlikely, as no such impact was observed in the younger rats.
Nonetheless, the structural scan confirmed the presence of the corpus callosum, indicating that major anatomical features remain intact.
Since neither method shows a consistent or interpretable trend, the results cannot be considered conclusive. More rats at the same age must be scanned to determine whether these findings are representative or anomalous.

6.6. T_2

The reference values for in vivo rat brain T_2, as reported in [40], is approximately 50 ms for white matter. This value was derived using conventional T_2-weighted

imaging and therefore reflect signal contributions from all tissue compartments, including extracellular space. Additionally, a reduction in T_2 is typically observed after fixation in ex vivo tissue, as described in [64]. Despite this expected decrease - and considering that the signal was acquired at high b-value to suppress extracellular signal contributions — the estimates obtained in this work are substantially higher: approximately 70 ms using the spherical variance method and up to 125 ms using the spherical mean technique. This discrepancy may suggest an insufficient signal-to-noise ratio, as even the use of spherical harmonics expansion failed to improve the estimates, indicating that the current protocol requires further refinement. The presence of T_2 values exceeding 500 ms outside the region of interest, observed with both techniques, supports this interpretation.
Furthermore, some voxels within the brain mask appear as zero in the spherical mean map due to visualization thresholds. In reality, these values are negative, which is physiologically implausible. This results from a higher spherical mean signal at the longer echo time, which contradicts the expected T_2 decay and may be attributed to noise or residual artifacts.
It is also possible that the relatively small volume of white matter in the rat brain limits the accuracy of compartment-specific T_2 estimation, and that the method may be better suited for human data where white matter is more abundant.
Nonetheless, the divergence between the two estimation approaches underscores the importance of accounting for all diffusion-restricted compartments. Neglecting the cellular component may introduce bias into the results.

As this investigation was exploratory, further development is left for future work. In particular, it would be valuable to improve the sequence design to assess whether T_2 differs between healthy and pathological tissue in disease models and how much the isotropic component impacts the axonal signal fraction.

6.7. Limitations and future work

The TDE protocol demonstrated sufficient sensitivity to detect diffusivity changes in ex vivo samples. However, its application to in vivo studies remains limited due to prohibitive scan durations—each acquisition currently lasts approximately 20 hours, rendering it unfeasible for use in living animals. Therefore, optimizing the acquisition protocol to reduce scan time is a crucial step toward enabling its use in preclinical studies and, potentially, in clinical settings. One possible optimization involves slightly reducing the $b_{\parallel}$ value, which was conservatively chosen in the current implementation. This could help improve the SNR and reduce the variance in the $D_{\parallel}$ estimates. However, this alone is unlikely to be sufficient, and further adjustments to the protocol will be necessary. A further limitation lies in the poor availability of suitable scanners capable of supporting advanced free gradient waveform sequences.

Thicker slices were used to improve the SNR; however, this introduces partial volume effects that must be taken into account during analysis.

As a validation strategy, parallel and perpendicular diffusivities could be estimated by fitting zonal ratios derived from the spherical harmonics expansion of the signal, and compared with the current results to assess consistency [58].

To further investigate changes in microstructural shape, time-dependent diffusion experiments would offer a powerful tool. By acquiring data at different diffusion times, it is possible to probe structures at multiple length scales. This may reveal spatially varying diffusivities along axons in the presence of morphological features such as beading or axonal swellings.

Parameter estimation in this study was performed using a simple nonlinear least squares optimization applied to the non-approximated signal equations. Signal ratios could not be directly used due to violations of the assumption of Gaussian-distributed residuals. To address this limitation, a promising direction for future work is the development of machine learning models capable of estimating microstructural parameters directly from signal ratios. For instance, models such as Random Forest regressors can learn complex, nonlinear mappings from the data without requiring strong assumptions about the underlying noise distribution. However, such models need access to reliable ground truth parameter values for supervised training. This ground truth can be obtained from simulations or approximated using estimates from established methods such as DTI, but care must be taken to ensure that the training data adequately captures the characteristics and variability of real acquisitions. When properly trained, these models could improve the robustness and generalizability of parameter estimation, particularly under challenging conditions with high noise levels, as is typical in TDE acquisitions.

In addition, a larger sample size with the same TE is needed to improve the robustness of the findings. In particular, increasing the number of subjects in the older cohort will be essential to determine whether the one individual currently scanned is an outlier or representative of a broader group.

7 | Conclusion

This MSc thesis investigated the application of free waveform diffusion encoding, specifically Triple Diffusion Encoding, in the context of early-stage Alzheimer's disease. The study employed the TgF344-AD rat model, which manifests the full pathological spectrum of human Alzheimer's disease, including amyloidosis, tauopathy, and neurodegeneration. The novel approach demonstrated promising sensitivity to subtle microstructural changes in the brains of 4-month-old rats, suggesting its potential for early detection of pathological alterations.
Among the extracted microstructural metrics, diffusivity parameters proved particularly sensitive to early pathological changes, capturing alterations in both white and gray matter—despite some noise in the parallel diffusivity maps. In white matter, these changes may reflect processes such as axonal swelling that remain undetected by conventional screening methods. However, axonal signal fraction showed no significant differences, and reductions in fractional anisotropy were observed primarily in gray matter.
Overall, the use of multiple diffusion encoding schemes enabled a more nuanced characterization of tissue microstructure, surpassing the descriptive capabilities of standard approaches like Diffusion Tensor Imaging, with the added advantage of directly obtaining these parameters from the data.
Nevertheless, caution must be exercised when interpreting these findings. The study would benefit from larger datasets to improve statistical power and generalizability. Future work should focus on optimizing echo time and enhancing signal-to-noise ratio, which are essential for translating this technique to in vivo imaging, where shorter scan durations present additional constraints. Another limitation to the in vivo application is the high gradient power needed, not always available in clinical settings.

In summary, this work highlights the potential of advanced diffusion encoding strategies such as TDE to uncover early microstructural abnormalities in neurodegenerative diseases. This contributes to the growing need for earlier and more sensitive diagnostic tools for Alzheimer's disease—an urgent public health challenge affecting a rapidly increasing number of individuals worldwide.

Bibliography

[1] [3] effects of heteroscedasticity and skewness on prediction in regression: Modeling growth of the human heart. In *Part B: Numerical Computer Methods*, volume 240 of *Methods in Enzymology*, pages 37–51. Academic Press, 1994. doi: https://doi.org/10.1016/S0076-6879(94)40042-3.

[2] K. W. Andersen, S. Lasič, H. Lundell, M. Nilsson, D. Topgaard, F. Sellebjerg, F. Szczepankiewicz, H. R. Siebner, M. Blinkenberg, and T. B. Dyrby. Disentangling white-matter damage from physiological fibre orientation dispersion in multiple sclerosis. *Brain communications*, 2(2):fcaa077, 2020.

[3] M. Andersson, M. Pizzolato, H. M. Kjer, K. F. Skodborg, H. Lundell, and T. B. Dyrby. Does powder averaging remove dispersion bias in diffusion mri diameter estimates within real 3d axonal architectures? *Neuroimage*, 248:118718, 2022.

[4] Y. Assaf and P. J. Basser. Composite hindered and restricted model of diffusion (charmed) mr imaging of the human brain. *Neuroimage*, 27(1):48–58, 2005.

[5] D. Barazany, P. J. Basser, and Y. Assaf. In vivo measurement of axon diameter distribution in the corpus callosum of rat brain. *Brain*, 132(5):1210–1220, 2009.

[6] G. Bartzokis. Alzheimer's disease as homeostatic responses to age-related myelin breakdown. *Neurobiology of aging*, 32(8):1341–1371, 2011.

[7] G. S. Bloom. Amyloid-β and tau: the trigger and bullet in alzheimer disease pathogenesis. *JAMA neurology*, 71(4):505–508, 2014.

[8] Bruker Corporation. Biospec 70/20 and 94/20 preclinical mri systems. `https://www.bruker.com/en/products-and-solutions/preclinical-imaging/mri/biospec/biospec-70-20-and-94-20.html`, 2025. Accessed: 2025-06-08.

[9] M. Budde.

[10] E. Caruyer, C. Lenglet, G. Sapiro, and R. Deriche. Design of multishell sampling schemes with uniform coverage in diffusion mri. *Magnetic resonance in medicine*, 69(6):1534–1540, 2013.

[11] R. M. Cohen, K. Rezai-Zadeh, T. M. Weitz, A. Rentsendorj, D. Gate, I. Spivak, Y. Bholat, V. Vasilevko, C. G. Glabe, J. J. Breunig, P. Rakic, H. Davtyan, M. G. Agadjanyan, V. Kepe, J. R. Barrio, S. Bannykh, C. A. Szekely, R. N. Pechnick, and T. Town. A transgenic alzheimer rat with plaques, tau pathology, behavioral impairment, oligomeric a, and frank neuronal loss. *Journal of Neuro-*

science, 33(15):6245–6256, 2013. ISSN 0270-6474. doi: 10.1523/JNEUROSCI.3672-12.2013. URL https://www.jneurosci.org/content/33/15/6245.

[12] G. M. Cooper and K. Adams. *The cell: a molecular approach*. Oxford University Press, 2022.

[13] L. Cordero-Grande, D. Christiaens, J. Hutter, A. N. Price, and J. V. Hajnal. Complex diffusion-weighted image estimation via matrix recovery under general noise models. *Neuroimage*, 200:391–404, 2019.

[14] L. Dan and Z. Zhang. Alzheimer's disease: an axonal injury disease? *Frontiers in Aging Neuroscience*, 15:1264448, 2023.

[15] Danish Research Centre for Magnetic Resonance (DRCMR). Danish research centre for magnetic resonance (drcmr). URL https://www.drcmr.dk/. Hvidovre Hospital, Denmark.

[16] S. Demir. Comparison of normality tests in terms of sample sizes under different skewness and kurtosis coefficients. *International Journal of Assessment Tools in Education*, 9(2):397–409, 2022.

[17] A. Einstein. *Investigations on the Theory of the Brownian Movement*. Courier Corporation, 1956.

[18] S. Eriksson, S. Lasič, M. Nilsson, C.-F. Westin, and D. Topgaard. NMR diffusion-encoding with axial symmetry and variable anisotropy: Distinguishing between prolate and oblate microscopic diffusion tensors with unknown orientation distribution. *The Journal of chemical physics*, 142(10):104201, 2015.

[19] A. Foi. Noise estimation and removal in mr imaging: The variance-stabilization approach. In *2011 IEEE International symposium on biomedical imaging: from nano to macro*, pages 1809–1814. IEEE, 2011.

[20] M. Gavish and D. L. Donoho. Optimal shrinkage of singular values. *IEEE Transactions on Information Theory*, 63(4):2137–2152, 2017.

[21] M. Giannelli, S. Diciotti, C. Tessa, and M. Mascalchi. Effect of echo spacing and readout bandwidth on basic performances of epi-fmri acquisition sequences implemented on two 1.5 t mr scanner systems. *Medical physics*, 37(1):303–310, 2010.

[22] M. Goedert. Alzheimer's and parkinson's diseases: The prion concept in relation to assembled aβ, tau, and α-synuclein. *Science*, 349(6248):1255555, 2015.

[23] J. Graessner. Bandwidth in mri. *Magnetom Flash*, 2:3–8, 2013.

[24] H. Gudbjartsson and S. Patz. The rician distribution of noisy mri data. *Magnetic resonance in medicine*, 34(6):910–914, 1995.

[25] J. S. Hansen. Detecting early microstructural changes in alzheimer's disease using a combination of advanced magnetic resonance imaging techniques and histochemical analysis. PhD project proposal, Department of Neurobiology, University of Southern Denmark, 2025, 2025.

[26] R. N. Henriques, M. Palombo, S. N. Jespersen, N. Shemesh, H. Lundell, and A. Ianuş. Double diffusion encoding and applications for biomedical imaging. *Journal of Neuroscience Methods*, 348:108989, 2021.

[27] L. B. Hinkley, E. J. Marco, A. M. Findlay, S. Honma, R. J. Jeremy, Z. Strominger, P. Bukshpun, M. Wakahiro, W. S. Brown, L. K. Paul, et al. The role of corpus callosum development in functional connectivity and cognitive processing. 2012.

[28] N. Honnorat, M. Mojtabai, J. Li, M. Smith, S. Seshadri, K. Bieniek, and M. Habes. A new halogenated solvent for ex vivo magnetic resonance imaging. *bioRxiv*, pages 2024–06, 2024.

[29] I. O. Jelescu, J. Veraart, E. Fieremans, and D. S. Novikov. Degeneracy in model parameter estimation for multi-compartmental diffusion in neuronal tissue. *NMR in Biomedicine*, 29(1):33–47, 2016.

[30] I. O. Jelescu, F. Grussu, A. Ianus, B. Hansen, R. L. Barrett, M. Aggarwal, S. Michielse, F. Nasrallah, W. Syeda, N. Wang, et al. Considerations and recommendations from the ismrm diffusion study group for preclinical diffusion mri: part 1: in vivo small-animal imaging. *Magnetic resonance in medicine*, 93 (6):2507–2534, 2025.

[31] J. H. Jensen and J. A. Helpern. Characterizing intra-axonal water diffusion with direction-averaged triple diffusion encoding MRI. *NMR in Biomedicine*, 31(7):e3930, 2018.

[32] H. Jiang, L. Svenningsson, and D. Topgaard. Multidimensional encoding of restricted and anisotropic diffusion by double rotation of the q-vector. *Magnetic Resonance Discussions*, 2022:1–12, 2022.

[33] D. K. Jones. Gaussian modeling of the diffusion signal. In *diffusion MRI*, pages 87–104. Elsevier, 2014.

[34] D. K. Jones, M. A. Horsfield, and A. Simmons. Optimal strategies for measuring diffusion in anisotropic systems by magnetic resonance imaging. *Magnetic Resonance in Medicine: An Official Journal of the International Society for Magnetic Resonance in Medicine*, 42(3):515–525, 1999.

[35] E. Kaden, N. D. Kelm, R. P. Carson, M. D. Does, and D. C. Alexander. Multi-compartment microscopic diffusion imaging. *NeuroImage*, 139:346, 2016.

[36] E. Kaden, F. Kruggel, and D. C. Alexander. Quantitative mapping of the per-axon diffusion coefficients in brain white matter. *Magnetic resonance in medicine*, 75(4):1752–1763, 2016.

[37] L. Kerkelä, R. N. Henriques, M. G. Hall, C. A. Clark, and N. Shemesh. Validation and noise robustness assessment of microscopic anisotropy estimation with clinically feasible double diffusion encoding mri. *Magnetic Resonance in Medicine*, 83(5):1698–1710, 2020.

[38] H. Kleven, I. E. Bjerke, F. Clascá, H. J. Groenewegen, J. G. Bjaalie, and T. B.

Leergaard. Waxholm space atlas of the rat brain: A 3d atlas supporting data analysis and integration. *Nature methods*, 20(11):1822–1829, 2023.

[39] A. Lehmenkühler, E. Syková, J. Svoboda, K. Zilles, and C. Nicholson. Extracellular space parameters in the rat neocortex and subcortical white matter during postnatal development determined by diffusion analysis. *Neuroscience*, 55(2):339–351, 1993.

[40] S. Liachenko and J. Ramu. Quantification and reproducibility assessment of the regional brain t2 relaxation in naive rats at 7t. *Journal of Magnetic Resonance Imaging*, 45(3):700–709, 2017.

[41] X. Ma, K. Uğurbil, and X. Wu. Denoise magnitude diffusion magnetic resonance images via variance-stabilizing transformation and optimal singular-value manipulation. *Neuroimage*, 215:116852, 2020.

[42] E. T. McKinnon and J. H. Jensen. Measuring intra-axonal t2 in white matter with direction-averaged diffusion mri. *Magnetic resonance in medicine*, 81(5): 2985–2994, 2019.

[43] P. E. McKnight and J. Najab. Mann-whitney u test. *The Corsini encyclopedia of psychology*, pages 1–1, 2010.

[44] H. Mirzaalian, L. Ning, P. Savadjiev, O. Pasternak, S. Bouix, O. Michailovich, G. Grant, C. E. Marx, R. A. Morey, L. A. Flashman, et al. Inter-site and inter-scanner diffusion mri data harmonization. *NeuroImage*, 135:311–323, 2016.

[45] P. Mishra, C. M. Pandey, U. Singh, A. Gupta, C. Sahu, and A. Keshri. Descriptive statistics and normality tests for statistical data. *Annals of cardiac anaesthesia*, 22(1):67–72, 2019.

[46] P. P. Mitra and B. I. Halperin. Effects of finite gradient-pulse widths in pulsed-field-gradient diffusion measurements. *Journal of Magnetic Resonance, Series A*, 113(1):94–101, 1995.

[47] P. Mukherjee, J. Berman, S. W. Chung, C. Hess, and R. Henry. Diffusion tensor mr imaging and fiber tractography: theoretic underpinnings. *American journal of neuroradiology*, 29(4):632–641, 2008.

[48] F. E. Musiek. Neuroanatomy, neurophysiology, and central auditory assessment. part iii: Corpus callosum and efferent pathways. *Ear and hearing*, 7(6):349–358, 1986.

[49] S. E. Nasrabady, B. Rizvi, J. E. Goldman, and A. M. Brickman. White matter changes in alzheimer's disease: a focus on myelin and oligodendrocytes. *Acta neuropathologica communications*, 6:1–10, 2018.

[50] A. Nataraj, K. Blahna, and K. Jezek. Insights from tgf344-ad, a double transgenic rat model in alzheimer's disease research. *Physiological Research*, 74(1): 1, 2025.

[51] D. S. Novikov, V. G. Kiselev, and S. N. Jespersen. On modeling. *Magnetic resonance in medicine*, 79(6):3172–3193, 2018.

[52] R. J. O'brien and P. C. Wong. Amyloid precursor protein processing and alzheimer's disease. *Annual review of neuroscience*, 34(1):185–204, 2011.

[53] L. J. O'Donnell and C.-F. Westin. An introduction to diffusion tensor image analysis. *Neurosurgery Clinics of North America*, 22(2):185, 2011.

[54] E. Papuć and K. Rejdak. The role of myelin damage in alzheimer's disease pathology. *Archives of Medical Science*, 16(2):345–341, 2018.

[55] D. L. Parker and G. T. Gullberg. Signal-to-noise efficiency in magnetic resonance imaging. *Medical Physics*, 17(2):250–257, 1990.

[56] M. Pizzolato, D. Wassermann, T. Duval, J. S. Campbell, T. Boutelier, J. Cohen-Adad, and R. Deriche. A temperature phantom to probe the ensemble average propagator asymmetry: an in-silico study. In *Computational Diffusion MRI: MICCAI Workshop, Munich, Germany, October 9th, 2015*, pages 183–194. Springer, 2016.

[57] M. Pizzolato, M. Andersson, E. J. Canales-Rodríguez, J.-P. Thiran, and T. B. Dyrby. Axonal t2 estimation using the spherical variance of the strongly diffusion-weighted mri signal. *Magnetic Resonance Imaging*, 86:118–134, 2022. ISSN 0730-725X. doi: https://doi.org/10.1016/j.mri.2021.11.012. URL `https://www.sciencedirect.com/science/article/pii/S0730725X21002356`.

[58] M. Pizzolato, E. J. Canales-Rodríguez, M. Andersson, and T. B. Dyrby. Axial and radial axonal diffusivities and radii from single encoding strongly diffusion-weighted mri. *Medical Image Analysis*, 86:102767, 2023.

[59] M. Questions. Gibbs artifact. `https://mriquestions.com/gibbs-artifact.html`. Accessed: 2025-06-09.

[60] K. M. Ramachandran and C. P. Tsokos. Chapter 13 - empirical methods. In K. M. Ramachandran and C. P. Tsokos, editors, *Mathematical Statistics with Applications in R (Second Edition)*, pages 639–686. Academic Press, Boston, second edition edition, 2015. ISBN 978-0-12-417113-8. doi: https://doi.org/10.1016/B978-0-12-417113-8.00013-8. URL `https://www.sciencedirect.com/science/article/pii/B9780124171138000138`.

[61] S. Ramanna, H. G. Moss, E. T. McKinnon, E. Yacoub, J. A. Helpern, and J. H. Jensen. Triple diffusion encoding MRI predicts intra-axonal and extra-axonal diffusion tensors in white matter. *Magnetic resonance in medicine*, 83 (6):2209–2220, 2020.

[62] A. Rubinski, N. Franzmeier, A. Dewenter, Y. Luan, R. Smith, O. Strandberg, R. Ossenkoppele, M. Dichgans, O. Hansson, M. Ewers, et al. Higher levels of myelin are associated with higher resistance against tau pathology in alzheimer's disease. *Alzheimer's research & therapy*, 14(1):139, 2022.

[63] P. Scheltens, B. De Strooper, M. Kivipelto, H. Holstege, G. Chételat, C. E. Teunissen, J. Cummings, and W. M. van der Flier. Alzheimer's disease. *The Lancet*, 397(10284):1577–1590, 2021.

[64] K. G. Schilling, F. Grussu, A. Ianus, B. Hansen, A. F. Howard, R. L. Barrett,

M. Aggarwal, S. Michielse, F. Nasrallah, W. Syeda, et al. Considerations and recommendations from the ismrm diffusion study group for preclinical diffusion mri: Part 2—ex vivo imaging: Added value and acquisition. *Magnetic resonance in medicine*, 2025.

[65] M. science group. Map-science diffusion pipeline. `https://github.com/MaP-science`, 2023. Accessed: 2025-06-09.

[66] A. S. Shatil, K. M. Matsuda, and C. R. Figley. A method for whole brain ex vivo magnetic resonance imaging with minimal susceptibility artifacts. *Frontiers in neurology*, 7:208, 2016.

[67] K. Singh and M. Xie. Bootstrap: a statistical method. *Unpublished manuscript, Rutgers University, USA. Retrieved from http://www. stat. rutgers. edu/home/mxie/RCPapers/bootstrap. pdf*, pages 1–14, 2008.

[68] J. Sjölund, F. Szczepankiewicz, M. Nilsson, D. Topgaard, C.-F. Westin, and H. Knutsson. Constrained optimization of gradient waveforms for generalized diffusion encoding. *Journal of magnetic resonance*, 261:157–168, 2015.

[69] E. O. Stejskal and J. E. Tanner. Spin diffusion measurements: spin echoes in the presence of a time-dependent field gradient. *The journal of chemical physics*, 42(1):288–292, 1965.

[70] R. Storn and K. Price. Differential evolution–a simple and efficient heuristic for global optimization over continuous spaces. *Journal of global optimization*, 11(4):341–359, 1997. doi: 10.1023/A:1008202821328.

[71] E. Syková and C. Nicholson. Diffusion in brain extracellular space. *Physiological reviews*, 88(4):1277–1340, 2008.

[72] F. Szczepankiewicz, C.-F. Westin, and M. Nilsson. Gradient waveform design for tensor-valued encoding in diffusion mri. *Journal of Neuroscience Methods*, 348:109007, 2021.

[73] J. Taylor. *Introduction to error analysis, the study of uncertainties in physical measurements*. 1997.

[74] J.-D. Tournier, R. Smith, D. Raffelt, R. Tabbara, T. Dhollander, M. Pietsch, D. Christiaens, B. Jeurissen, C.-H. Yeh, and A. Connelly. Mrtrix3: A fast, flexible and open software framework for medical image processing and visualisation. *NeuroImage*, 202:116137, 2019. ISSN 1053-8119. doi: https://doi.org/10.1016/j.neuroimage.2019.116137. URL `https://www.sciencedirect.com/science/article/pii/S1053811919307281`.

[75] J. Veraart, D. Nunes, and N. Shemesh. Detecting temperature-driven microstructural modulations in tissue using diffusion mri.

[76] S. B. Vos, D. K. Jones, B. Jeurissen, M. A. Viergever, and A. Leemans. The influence of complex white matter architecture on the mean diffusivity in diffusion tensor mri of the human brain. *Neuroimage*, 59(3):2208–2216, 2012.

[77] C. Wang, L. Song, R. Zhang, and F. Gao. Impact of fixation, coil, and number

of excitations on diffusion tensor imaging of rat brains at 7.0 t. *European radiology experimental*, 2:1–10, 2018.

[78] C.-F. Westin, H. Knutsson, O. Pasternak, F. Szczepankiewicz, E. Özarslan, D. van Westen, C. Mattisson, M. Bogren, L. J. O'donnell, M. Kubicki, et al. Q-space trajectory imaging for multidimensional diffusion mri of the human brain. *Neuroimage*, 135:345–362, 2016.

[79] H. Zhang, T. Schneider, C. A. Wheeler-Kingshott, and D. C. Alexander. Noddi: practical in vivo neurite orientation dispersion and density imaging of the human brain. *Neuroimage*, 61(4):1000–1016, 2012.

[80] M. Zucchelli, S. Deslauriers-Gauthier, and R. Deriche. A computational framework for generating rotation invariant features and its application in diffusion mri. *Medical image analysis*, 60:101597, 2020.

A | Appendix

A.1. Statistical comparison between cortical areas in control rats

Parameter	Method	p-value (motor vs. somatosensory)
AxD	DTI	5.19×10^{-163}
	TDE	6.68×10^{-28}
RD	DTI	3.91×10^{-31}
	TDE	9.48×10^{-4}
FA	DTI	2.82×10^{-186}
	TDE	7.90×10^{-12}
ASF	TDE	1.73×10^{-15}

Table A.1: P-values from the comparison of axial diffusivity (AxD), radial diffusivity (RD), fractional anisotropy (FA), and axonal signal fraction (ASF) between motor and somatosensory regions in control rats.

A.2. Statistical comparison between control and Alzheimer's rats

Label	Method	p-value AxD	p-value RD	p-value FA	p-value ASF
WM	DTI	1.46×10^{-11}	1.83×10^{-1}	8.58×10^{-2}	–
WM	TDE	5.23×10^{-25}	2.25×10^{-6}	2.80×10^{-17}	4.12×10^{-1}
GM (motor)	DTI	2.37×10^{-19}	1.31×10^{-4}	5.71×10^{-1}	–
GM (motor)	TDE	8.09×10^{-80}	6.37×10^{-101}	3.90×10^{-105}	3.70×10^{-101}
GM (ss)	DTI	9.41×10^{-12}	1.26×10^{-1}	2.50×10^{-9}	–
GM (ss)	TDE	6.97×10^{-26}	2.81×10^{-39}	2.52×10^{-41}	7.46×10^{-34}

Table A.2: P-values for the comparison between Alzheimer and control rats across ROIs and methods for AxD, RD, FA, and ASF.

A.3. Variance of $D_{\parallel}$ via Error Propagation

This section presents the calculation of the variance of $D_{\parallel}$ using the standard error propagation method.

Consider the signal model defined in Equation 3.73:

$$\bar{S}(b_{\parallel}, b_{\perp}) \approx K \cdot A \cdot B$$

where:

$$\begin{aligned} K &= C\frac{1}{\sqrt{b_{\parallel} - b_{\perp}}} \text{ is a constant independent of } D_{\parallel}, \\ A &= \exp\left(-b_{\parallel}D_{\perp} - b_{\perp}(D_{\parallel} + D_{\perp})\right), \\ B &= \sqrt{\frac{\pi}{4(D_{\parallel} - D_{\perp})}}. \end{aligned}$$

From the standard formula for error propagation [73], the standard deviation of $D_{\parallel}$, denoted $\sigma D_{\parallel}^2$, is related to the signal standard deviation $\sigma \bar{s}^2$ via:

$$\sigma_{D_{\parallel}} = \left|\frac{\partial D_{\parallel}}{\partial \bar{S}}\right| \cdot \sigma_{\bar{S}}. \tag{A.1}$$

Since the derivative $\frac{dD_{\parallel}}{d\bar{S}}$ is generally not available in closed form, the inverse of the forward model derivative is used:

$$\sigma_{D_{\parallel}} = \frac{\sigma_{\bar{S}}}{\left|\frac{\partial \bar{S}}{\partial D_{\parallel}}\right|}. \tag{A.2}$$

The expressions A.1 and A.2 are mathematically equivalent, as long as the function $\bar{S}(D_{\parallel})$ is locally invertible and differentiable. The second form is typically preferred because the signal $\bar{S}$ is the measured quantity, and its dependence on the model parameter $D_{\parallel}$ is explicitly known through the forward model.

Therefore, the following variance can be calculated:

$$\sigma D_{\parallel}^2 = \left(\frac{\partial \bar{S}}{\partial D_{\parallel}}\right)^{-2} \cdot \sigma \bar{S}^2. \tag{A.3}$$

This expression describes how noise in the measured signal propagates into uncertainty in the estimated parameter $D_{\parallel}$.

Solving for the signal espression, the derivative of $\bar{S}$ with respect to $D_{\parallel}$ is obtained

using the product rule:

$$\frac{\partial \bar{S}}{\partial D_{\parallel}} = K \cdot \left(\frac{\partial A}{\partial D_{\parallel}} \cdot B + A \cdot \frac{\partial B}{\partial D_{\parallel}} \right). \tag{A.4}$$

Computing the derivative of the exponential term in A with respect to $D_{\parallel}$ yields:

$$\frac{\partial A}{\partial D_{\parallel}} = -b_{\perp} \cdot A. \tag{A.5}$$

The derivative of B is computed with the chain rule as:

$$\frac{\partial B}{\partial D_{\parallel}} = \left(\frac{\pi}{4}\right)^{1/2} \cdot \left(-\frac{1}{2}\right) \cdot \left(D_{\parallel} - D_{\perp}\right)^{-\frac{3}{2}}. \tag{A.6}$$

Simplifying the expression and expressing it with respect to B:

$$\frac{\partial B}{\partial D_{\parallel}} = -\frac{1}{2}\sqrt{\frac{\pi}{4(D_{\parallel} - D_{\perp})}} \cdot \frac{1}{D_{\parallel} - D_{\perp}} = -\frac{1}{2} \cdot \frac{B}{(D_{\parallel} - D_{\perp})}. \tag{A.7}$$

Substituting both expressions A.5 and A.7 into Eq. A.4 gives:

$$\frac{\partial \bar{S}}{\partial D_{\parallel}} = K \left[(-b_{\perp} A)B + A \cdot \left(-\frac{1}{2} \cdot \frac{B}{D_{\parallel} - D_{\perp}} \right) \right] = -KAB \left(b_{\perp} + \frac{1}{2(D_{\parallel} - D_{\perp})} \right). \tag{A.8}$$

According to Eq. A.2, the variance of $D_{\parallel}$ is therefore:

$$\sigma^2_{D_{\parallel}} = \left(\frac{\sigma_{\bar{S}}}{KAB\left(-b_{\perp} - \frac{1}{2(D_{\parallel} - D_{\perp})}\right)} \right)^2 = \frac{\sigma^2_{\bar{S}}}{K^2 A^2 B^2 \left(b_{\perp} + \frac{1}{2(D_{\parallel} - D_{\perp})}\right)^2}. \tag{A.9}$$

A.3.1. Variance of $D_{\parallel}$ with respect to $b_{\perp}$

Rewriting the expressions for A, B, K considering what is not dependent on $b_{\perp}$ as a constant, one obtains:

$$A = \exp(-b_{\parallel} D_{\perp}) \cdot \exp(-b_{\perp}(D_{\parallel} + D_{\perp})) = C_1 \cdot \exp(-b_{\perp} J), \tag{A.10}$$

where $C_1 = \exp(-b_{\parallel} D_{\perp})$ and $J = D_{\parallel} + D_{\perp}$ are constant with respect to $b_{\perp}$.

B is independent of $b_{\perp}$ hence can be regarded as a constant:

$$B = \sqrt{\frac{\pi}{4(D_{\parallel} - D_{\perp})}} = C_2. \tag{A.11}$$

Eventually, K stays unchanged:

$$K = C\frac{1}{\sqrt{b_\parallel - b_\perp}}. \tag{A.12}$$

Substituting these into the variance expression:

$$\sigma_{D_\parallel}^2 = \frac{\sigma_{\bar{S}}^2}{\left(\frac{C}{\sqrt{b_\parallel - b_\perp}} \cdot C_1 \cdot \exp(-b_\perp J) \cdot C_2\right)^2 \left(b_\perp + \frac{1}{2(D_\parallel - D_\perp)}\right)^2}. \tag{A.13}$$

Grouping constants into a single term $C_{\text{total}} = C \cdot C_1 \cdot C_2$, one obtains:

$$\sigma_{D_\parallel}^2 = \frac{\sigma_{\bar{S}}^2 \cdot (b_\parallel - b_\perp)}{C_{\text{total}}^2 \cdot \exp(-2b_\perp J) \cdot \left(b_\perp + \frac{1}{2(D_\parallel - D_\perp)}\right)^2}. \tag{A.14}$$

meaning

$$\sigma_{D_\parallel} \propto \sqrt{b_\parallel - b_\perp} \cdot \exp(b_\perp J) \cdot \left(b_\perp + \frac{1}{2(D_\parallel - D_\perp)}\right)^{-1}. \tag{A.15}$$

This highlights the nontrivial dependency of the variance on $b_\perp$, with exponential, polynomial, and square-root terms all contributing. By the asymptotic comparison theorem from real analysis, a positive exponential function will eventually dominate any polynomial function as the argument tends to infinity. Therefore, in practice, reducing $b_\perp$ is essential for suppressing uncertainty in $D_\parallel$.

A.3.2. Variance of $D_\parallel$ with respect to $b_\parallel$

Again, rewriting $\bar{S} = KAB$, isolating terms dependent on $b_\parallel$:

$$\bar{S} = C_3 \cdot \frac{1}{\sqrt{b_\parallel - b_\perp}} \cdot \exp(-b_\parallel D_\perp), \tag{A.16}$$

where $C_3 = C \cdot \exp(-b_\perp(D_\parallel + D_\perp)) \cdot \sqrt{\frac{\pi}{4(D_\parallel - D_\perp)}}$ is constant with respect to $b_\parallel$.

Substituting Equation (A.16) into the expression for variance:

$$\sigma_{D_\parallel}^2 = \frac{\sigma_{\bar{S}}^2}{C_3^2 \cdot \frac{1}{b_\parallel - b_\perp} \cdot \exp(-2b_\parallel D_\perp) \cdot \left(b_\perp + \frac{1}{2(D_\parallel - D_\perp)}\right)^2}. \tag{A.17}$$

Equivalently,

$$\sigma_{D_\parallel}^2 = \sigma_{\bar{S}}^2 \cdot (b_\parallel - b_\perp) \cdot \exp(2b_\parallel D_\perp) \cdot \frac{1}{C_3^2 \left(b_\perp + \frac{1}{2(D_\parallel - D_\perp)}\right)^2}. \tag{A.18}$$

Hence, the proportional dependence becomes:

$$\sigma_{D_\parallel} \propto \sqrt{b_\parallel - b_\perp} \cdot \exp(b_\parallel D_\perp). \tag{A.19}$$

This illustrates the complex dependence of the variance on $b_\parallel$, involving exponential, polynomial, and square-root terms. According to the asymptotic comparison theorem from real analysis, the positive exponential component dominates both polynomial and root terms as $b_\parallel$ increases. Consequently, reducing $b_\parallel$ is an effective strategy to minimize the uncertainty in estimating $D_\parallel$.

List of Abbreviations

Table A.3: List of abbreviations

Abbreviation	Definition
AD	Alzheimer's Disease
Aβ	Amyloid Beta
APOE	Apolipoprotein E
APP	Amyloid Precursor Protein
ASF	Axonal Signal Fraction
AWGN	Additive White Gaussian Noise
AxD	Axial Diffusivity
BIDS	Brain Imaging Data Structure
BW	Bandwidth
CSF	Cerebrospinal Fluid
DTI	Diffusion Tensor Imaging
DWI	Diffusion Weighted Imaging
dMRI	Diffusion Magnetic Resonance Imaging
EPI	Echo Planar Imaging
ER	Endoplasmic Reticulum
EUIVST	Exact Unbiased Inverse Variance Stabilizing Transformation
FAD	Familial Alzheimer's Disease

Continued on next page

Table A.3 continued from previous page

Abbreviation	Definition
FA	Fractional Anisotropy
FAT	Fast Axonal Transport
FDA	Food and Drug Administration
FOV	Field of View
GM	Gray Matter
hAPP	Human Amyloid Precursor Protein
hPSEN1	Human Presenilin-1
KS	Kolmogorov-Smirnov
LOAD	Late Onset Alzheimer's Disease
LTP	Long-Term Potentiation
MAPT	Microtubule Associated Protein Tau
MCI	Mild Cognitive Impairment
MDE	Multiple Diffusion Encoding
MP	Marchenko Pastur
MP-PPCA	Marchenko-Pastur Principal Component Analysis
MRI	Magnetic Resonance Imaging
MSE	Mean Squared Error
NODDI	Neurite Orientation Dispersion and Density Imaging
NFT	NeuroFibrillary Tangle
NLLS	Non-Linear Least Squares
ODF	Orientation Distribution Function
PE	Phase Encoding

Continued on next page

Table A.3 continued from previous page

Abbreviation	Definition
PET	Positron Emission Tomography
PFPE	Perfluoropolyether
PFA	Paraformaldehyde
PGSE	Pulsed Gradient Spin Echo
PMI	Post Mortem Interval
PSEN1	Presenilin-1
PSEN2	Presenilin-2
RARE	Rapid Acquisition with Relaxation Enhancement
RD	Radial Diffusivity
RF	Radio Frequency
RO	Readout
RMS	Root Mean Square
RMSD	Root Mean Square Displacement
SE	Spin Echo
SDE	Single Diffusion Encoding
SMT	Spherical Mean Technique
SøPB	Sodium Phosphate Buffer
SS	Somatosensory
SNR	Signal-to-Noise Ratio
TE	Echo Time
Tg	Transgenic
TDE	Triple Diffusion Encoding

Continued on next page

Table A.3 continued from previous page

Abbreviation	Definition
TR	Repetition Time
TREM2	Triggering Receptor Expressed on Myeloid cells 2
VST	Variance Stabilization Transformation
WHS	Waxholm Space
WM	White Matter
WT	Wild Type

List of Figures

List of Tables

Acknowledgements

Anche questo viaggio lungo e bellissimo sta per finire. Grazie a tutti quelli che ci sono stati, che mi hanno fatta ridere e risposto alle mie domande.

Il primo pensiero va ai miei coniquilini, che hanno accettato la mia postazione con sedia da ufficio in salotto, anche se rovina il danish design. Grazie perchè mi volete bene anche se cambio sempre idea e avete sopportato 5 mesi di discorsi sui topi. Poi ringrazio tutti i nuovi amici che ho conosciuto al nord. Dalla famiglia di Hempel, che mi ha accolta nel primo inverno, a tutti quelli che hanno trovato un po' di spazio per me in questi due anni. Menzione speciale a Juan Ma per avermi preparato la zuppa quando stavo male. La prossima volta chiamo Vasco quando vedo le scosse di elettricità.

Grazie ai miei supervisors danesi, che non si sono spaventati a gennaio quando mi sono seduta per terra per trovare la soluzione ad un integrale triplo. E grazie al prof. Caiani per avere facilitato il processo di doppia laurea.

Un bacione agli amici pazzi di Lugo che mi fanno sentire leggera e speciale ogni volta che ci sentiamo o vediamo. Vi voglio bene. Grazie agli amici sparsi in giro per l'Italia, conosciuti a Thiene, Padova, Milano o chissà dove, che hanno il tempo di ascoltare i miei audio con le avventure danesi e di raccontarmi come vanno le loro vite. Un abbraccio a Sara, Rebecca ed Eleonora, le mie compagne di studio di triennale e magistrale, che hanno alleggerito le sessioni e risposto ai miei dubbi.

Grazie alla mia famiglia che mi ascolta quando mi lamento, ma è sempre pronta a sostenermi. Grazie mamma perchè mi hai insegnato che la matematica non fa paura. Risolvere i problemi sui triangoli è il primo passo per affrontare i problemi della vita.

Cheers al futuro!

Vittoria